

7 Active Galactic Nuclei

Eric S. Perlman

Department of Physics and Space Sciences, Florida Institute of Technology, Melbourne, FL, USA

1	A Little History	306
2	Fundamental Properties of AGN	308
2.1	Overall Continuum Shape	308
2.2	Emission and Absorption Lines in the Optical – UV	310
2.3	Radio Emission and the Radio-Loud/Radio-Quiet Divide	312
2.3.1	Radio-Loud Versus Radio-Quiet: A True Bimodality?	314
2.3.2	Radio Morphology	314
2.4	Infrared Emission	318
2.5	X-Ray and Higher-Energy Emission	320
2.6	Variability	322
3	The Overall Structure: Unified Models	325
3.1	The Basic Scheme	326
3.2	Evidence for Type 1/Type 2 Unification	329
3.3	Blazars, Jets, and Unified Schemes for Radio-Loud AGN	330
4	Nuclear Black Holes and Accretion	335
4.1	Bondi Accretion	339
4.2	Disk Accretion	340
4.3	Disk Coronae and the 6.4 keV Iron Line	342
5	Emission Line Regions	347
5.1	Reverberation Mapping	348
5.2	Physical Conditions in the BLR	350
5.3	Physical Conditions in the Narrow-Line Region	352
5.4	Photoionization	353
6	Nuclear Obscuration: Tori, Broad, and Narrow Absorption Lines	356
6.1	The Torus	356
6.2	Line Absorption	358
7	Jets and Lobes in Radio Loud AGN	366
7.1	Acceleration of Jets	366
7.2	Propagation and Dynamics of Jets at Larger Scales	370
7.3	Emission Mechanisms in Jets	373
8	Final Remarks	379
References		381

Abstract: Active galactic nuclei (AGN) represent an extreme stage in the life cycle of a galaxy. For a relatively short period of time ($\sim 10^8$ years or less), a region less than a parsec across at the center of a galaxy produces tremendous amounts of energy, often outshining the rest of the galaxy by orders of magnitude. The most luminous of these objects are the most powerful, continuously emitting sources in the universe. The observational characteristics of AGN are reviewed, as well as how these properties are used to sort them into different classes. The evidence that supports the current paradigm, under which the central source powering AGN is a supermassive black hole, is discussed. While these are found in virtually all bright galaxies, in AGN the black holes are actively accreting matter, most likely as a result of an increased matter density in their immediate environs. A variety of accretion models are considered, particularly disk and Bondi accretion, along with the mechanisms by which material is carried inward and angular momentum is dissipated. Photoionization models for the broad and narrow emission line regions are reviewed in detail, including the physical conditions that prevail in each and their location relative to the central black hole. The evidence for unified models is presented. Under unified models, different types of AGN are related by means of viewing angle. A key aspect of these models is the presence of large-scale obscuring regions within the active nucleus. The phenomenology of nuclear absorption is discussed, both within the torus as well as in lines, along with present models for these obscuring regions. Also discussed are generation mechanisms for and the physics of relativistic jets, which are present in 10–20% of AGN. Finally, the entire picture is brought together by discussing the evolution of AGN.

Keywords: Accretion, Active galactic nuclei (AGN), BAL quasars, Blazars, Bremsstrahlung, Continuum emission, Coronal processes, Emission line regions, Galaxy evolution, Gamma-ray emission, General relativistic effects, Infrared emission, Inverse-Compton radiation, Jets, LINERs, Nuclear absorption, Nuclear structure, Outflows, Photoionization, Polarization, Quasars, Radio emission, Radio lobes, Reverberation mapping, Seyfert galaxies, Special relativistic effects, Superluminal motion, Supermassive black holes, Synchrotron radiation, Torus, Unified AGN models (Unified Schemes), Variability, Winds, X-ray emission

1 A Little History

It has been more than 100 years since the first evidence of nuclear activity in galaxies was first discovered. Interestingly, this history proceeded parallel to – rather than after – the discovery of the spiral nebulae themselves, and as with so many in astronomy, was at least partly the result of serendipity. As pointed out by Osterbrock (1999) and Shields (1999), the first documented observation of what today is called an active galactic nucleus was made by E. A. Fath in 1907 using the Lick 36-inch reflector telescope (Fath 1909). Fath was using a prism spectrograph that he had built; as part of his thesis project, he obtained low-resolution spectra of seven spiral nebulae, including M31. These observations required a titanic effort – his spectrum of M31 required 18 h of exposure. Most of his spectra were dominated by the same absorption lines seen in stars. However, one spectrum stood out: that of NGC 1068, which showed emission lines, more typical of planetary nebulae – what one would recognize today as H β ; [O III] $\lambda\lambda$ 4363, 4959, 5007; [OII] λ 3727; and [Ne III] λ 3869. During the next two decades, several different observers – notably Pease (1915), Moore (1915), Slipher (1917), and Hubble (1926) – also noticed emission lines in spectra of NGC 1068, NGC 4151 (see, e.g., Fig. 7-1), and NGC 4051. Another nine such objects were known by the time that Carl K. Seyfert, then a National Research

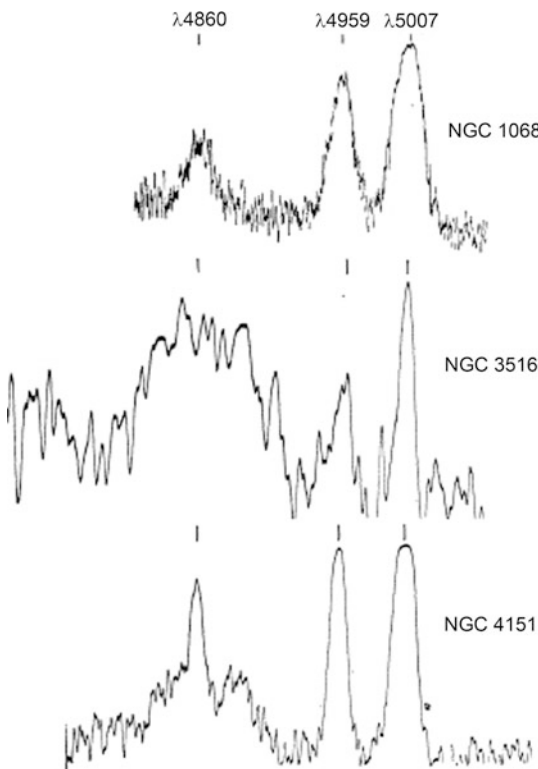


Fig. 7-1

A section of three of the early spectra of active galaxies, obtained using the Mt. Wilson 1.5 and 2.5 m telescopes by Carl Seyfert (1943, his Fig. 1). Note the bright H β and [O III] emission lines seen in all three spectra

Council Postdoctoral Fellow, systematized the properties of what are now called Seyfert galaxies (Seyfert 1943). As Seyfert wrote, the “most consistent characteristic” of the class was “an exceedingly luminous stellar or semistarrier nucleus which contains a relatively large percentage of the total light of the system.” He also pointed out that many of the anomalous emission lines were amazingly wide – up to $10,000 \text{ km s}^{-1}$. Figure 7-1 shows Seyfert’s spectra for three of the earliest known AGN in the region around H β and [O III] $\lambda\lambda 4959, 5007$. All three of these lines are visible in each spectrum, although their strength and width vary significantly – a factor discussed later in this chapter.

It was Seyfert’s work that first put forth the hypothesis that there was a distinct class of galaxies whose properties were dominated by nuclear emissions. At nearly the same time as Slipher, Pease, and Moore were undertaking their spectroscopic studies, Heber Curtis pointed out in 1918 that the galaxy M87 exhibited a “curious straight ray...apparently connected with the nucleus by a thin line of matter.” At the time, Curtis’s discovery was not connected to the spectroscopic evidence mentioned above – it took a large number of other discoveries for this to happen. The key development in this regard was the development of radio astronomy as a discipline. As is well known, the first receiver sensitive enough to receive cosmic radio emissions was built by Karl Jansky in the 1920s. Jansky, who at the time was working at Bell

Laboratories, was conducting a study of the sources of static in trans-Atlantic communications (Jansky 1932). His records showed two types of interference: thunderstorms and a persistent hiss that moved around in azimuth every 24 h and precessed through the sky seasonally. After further study, (Jansky 1933, 1935) concluded that the radiation came from the center and disk of the Milky Way galaxy. During the next decade, the first radio maps and surveys of the sky were done (Reber 1940a, b; Ryle and Smith 1948). By 1950, three radio sources had been identified with external galaxies (Bolton et al. 1949), namely, Virgo A (M87), Cygnus A, and Centaurus A (NGC 5128). Each of these objects was later identified optically as an active galaxy. This pointed out another facet of the AGN phenomenon – namely, that a substantial fraction have well-collimated outflows that extend out for many kiloparsecs from the nuclear regions.

Radio astronomy continued to play a role in defining our knowledge of active galaxies during the next two decades, as two bright radio sources, namely, 3C 273 and 3C 48, were the first two objects found to have systemic redshifts greater than 0.1 (Hazard et al. 1963; Schmidt 1963; Oke 1963; Greenstein and Matthews 1963). While initially there was some controversy about the nature of these redshifts (respectively 0.16 and 0.37), with some suggesting bizarre configurations such as galactic stars with a high density and hence a large gravitational redshift, the least objectional interpretation was that the redshifts were cosmological; however, this would require extreme optical luminosities for these objects, 10–30 times that of the brightest elliptical galaxy, and total emitted energies as high as 10^{60} ergs (Greenstein and Schmidt 1963).

2 Fundamental Properties of AGN

As can be seen by the previous discussion, the class of objects which today are called active galactic nuclei (or AGN) displays a rather complex phenomenology. These properties include not only bright emission lines but also strong continua (both thermal and nonthermal), X-ray, and radio emission. In this section, the observational properties of AGN are discussed, along with the taxonomy that has been developed through the years to describe subclasses.

2.1 Overall Continuum Shape

One of the distinguishing characteristics of AGN is a strong continuum that stretches from at least the infrared through hard X-rays, and in some cases up to gamma-ray energies. In Fig. 7-2, two examples of the broadband spectral energy distributions (SEDs) of AGN are shown. The SEDs of AGN are very different from those of typical galaxies: instead of displaying two main peaks (in the optical and far-IR, respectively, from starlight and cool dust emission) a much broader distribution is seen, with nearly equal power per decade from millimeter wavelengths through X-rays. For this reason, it is typical to characterize the spectra of AGN over a broad range of frequencies as a power law of the form $F_\nu \propto \nu^{-\alpha}$, where α is the spectral index. $\alpha = 0$ corresponds to a flat spectrum in F_ν , whereas $\alpha = 1$ describes a spectrum in which the luminosity is constant in every decade of frequency, similar to the situation seen in Fig. 7-2 over the infrared to soft X-rays.

Two other features seen in Fig. 7-2 are immediately obvious: the local maxima in the ultraviolet and mid-infrared, displayed in both SEDs. The first of these, often referred to as the “big blue bump,” has a remarkably similar shape in most AGN, with a peak in the far-UV and

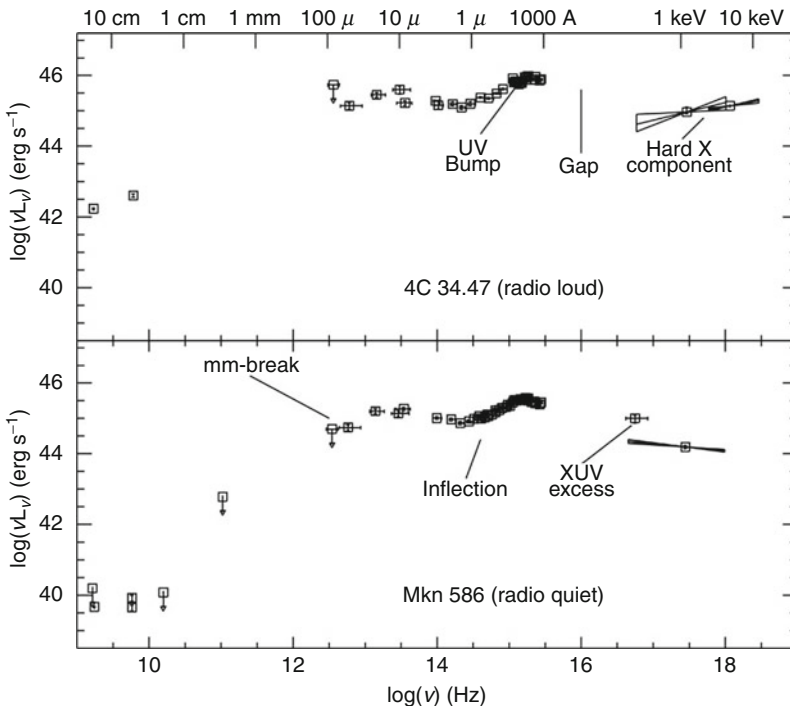


Fig. 7-2

Broadband spectral energy distributions of two typical active galaxies, one radio-loud and one radio-quiet. The two are essentially identical except in the radio, where the radio-loud object, 4C 34.47, is brighter by 3 orders of magnitude (Figure taken from Impey and Neugebauer (1988, their Fig. 1))

a typical UV spectral index of $\alpha = 0.3$ (Zheng et al. 1998; Scott et al. 2004). This translates to a U-B color of <-0.3 , far bluer than that seen in “passive” galaxies and also bluer than all stellar populations except hot white dwarfs. This same characteristic also gives AGN spectra between the UV and X-rays a very characteristic shape, with spectral indices α_{OX} clustered tightly between 1.2 and 1.8 (Tang et al. 2007). As discussed later on in this chapter, the UV bump is often interpreted in terms of emission from an accretion disk surrounding a central black hole (e.g., Shang et al. 2005 and references therein). The second “hump,” believed to be due to thermal emission from warm dust at greater distances from the central engine, has a much more diverse morphology, with dust temperatures seen from tens to thousands of Kelvin, and often includes multiple components.

Emission is also seen in other bands, including a strong high-energy continuum in X-rays as well as radio emission. The strong X-ray emission is a property shared by both SEDs which, as shown later on in this chapter, is a characteristic common to all AGN, although strong obscuration in some objects can impair our ability to see this component. The radio luminosity of the two SEDs shown in Fig. 7-2 differ radically, however, by more than 3 orders of magnitude relative to the emission seen in other bands. This points out what is known as the radio-loud/radio-quiet dichotomy, a subject that will be explored in depth later on in this chapter.

2.2 Emission and Absorption Lines in the Optical – UV

As already discussed, one of the original, distinguishing characteristics of AGN was their bright emission lines. These lines are the dominant feature of AGN spectra in the optical-UV, as shown in [Fig. 7-3](#), which was generated from the Sloan Digital Sky Survey's quasar sample (Van den Berk et al. 2001). As can be seen, many bright lines are present, including the Hydrogen Lyman and Balmer series as well as lines of various ionized metal species, such as MgII, CIII, CIV, OIII, etc. Near-IR observations reveal similar lines.

The lines come in two categories: broad ($\text{FWHM} > 1,000 \text{ km s}^{-1}$) and narrow ($\text{FWHM} < 1,000 \text{ km s}^{-1}$). Generally speaking, it is the permitted lines (e.g., Ly α , C IV $\lambda 1549$, C III $\lambda 1909$, Mg II $\lambda 2798$, H α , H β) which are observed to be broad, while forbidden lines (e.g., [O III] $\lambda\lambda 4959, 5007$; [OII] $\lambda 3727$) are observed to be narrow – although many or most permitted lines are also observed to have a narrow core. The widths of these emission lines are generally interpreted as Doppler shifts, and thus indicative of gas motions in the producing regions. These emission lines are very different from what is normally found in external galaxies, as seen in [Fig. 7-4](#), which shows the spectrum of Seyfert 1 and 2 galaxies, as well as a LINER (low-ionization emission region) galaxy, a BL Lacertae object (see [Sect. 3](#)), broad- and narrow-line radio galaxies (BLRG and NLRG, respectively), as well as a normal galaxy.

The differences between the main AGN spectral types is reasonably obvious – no broad lines are found in Seyfert 2s or NLRG, while LINERS have predominantly narrow lines, but only in low-ionization states (their lines are generally less broad as well), and the BL Lac objects

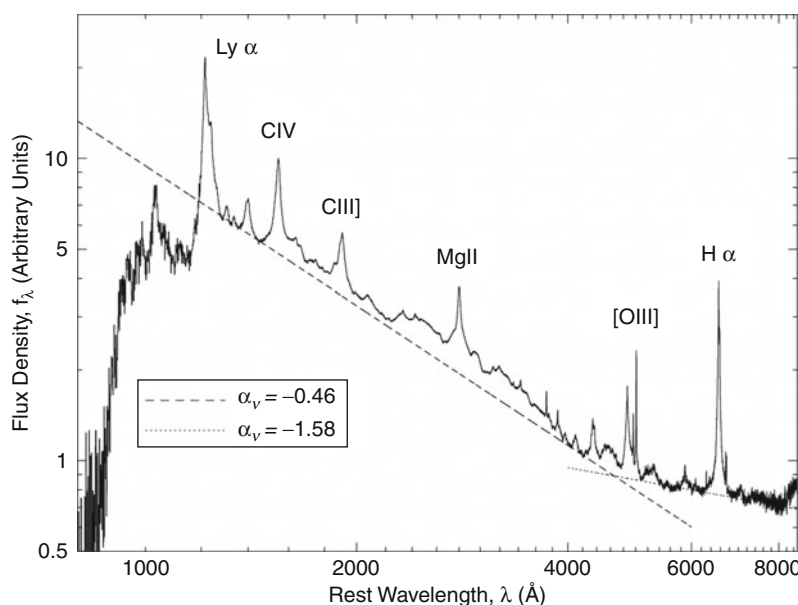


[Fig. 7-3](#)

Composite quasar spectrum, constructed from over 2,200 quasars in the SDSS DR 1. The dotted line indicates power law fits to the estimated continuum spectrum (From Van den Berk et al. (2001, their Fig. 3))

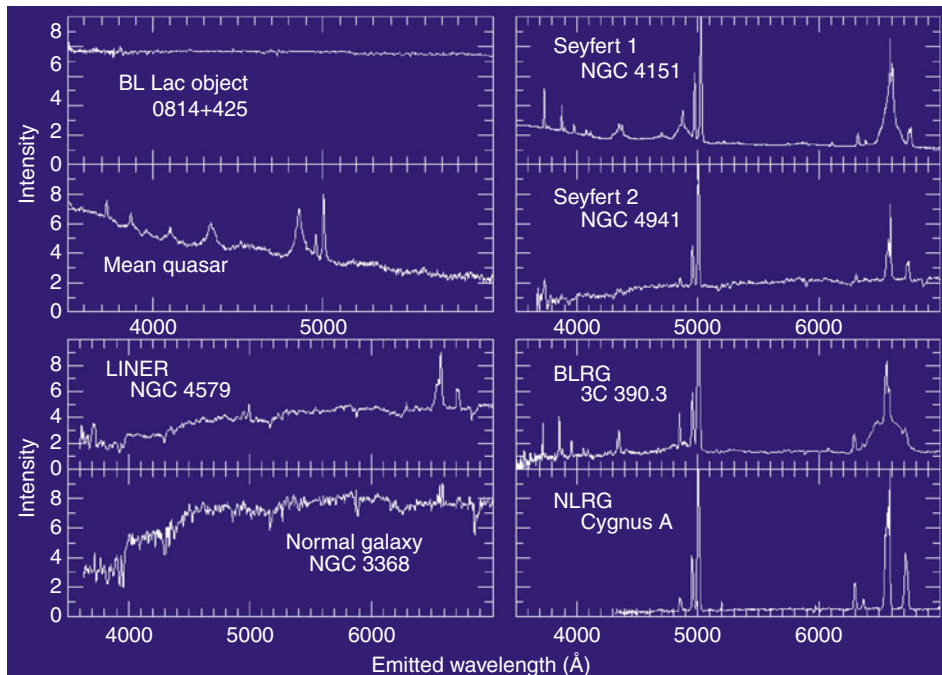


Fig. 7-4

Optical spectrum of several different types of active galaxies as compared to a normal elliptical. Note the strong emission lines present in all types except the BL Lacs and LINERs, where they are either weaker or absent. Note also that narrow-line objects completely lack the broad lines found in Seyfert 1 or BLRG-type objects (Figure taken from Keel, <http://astronomy.ua.edu/keel/agn>)

show a nearly complete lack of emission lines. What is not shown in Fig. 7-4, however, is that the same narrow lines are seen also in starburst galaxies, where they originate in HII regions surrounding hot stars. Therefore, in identifying AGN, one does need to be careful. Veilleux and Osterbrock (1987) proposed to use the line strengths of five commonly found features to distinguish between Seyferts, LINERS, and HII (Starburst) galaxies. This procedure, illustrated in Fig. 7-5, is quite efficient at sorting objects into AGN and nonactive objects, although there is some overlap. These “transition objects” indicate a possible link between the two phenomena.

The fact that there exists a significant population of AGN without broad emission lines was for many years a source of significant controversy in the field. Various attempts were made to explain these objects as being less luminous, but these were unsuccessful, as the bolometric luminosity of Seyfert 1 and 2 galaxies are similar. As discussed later, however, comparing the broadband spectra of Seyfert 1 and 2 objects, one sees the evidence of significant obscuration, as not only are the broad lines missing in Seyfert 2s but their optical spectra are redder, and they are also brighter in the mid-infrared (where any AGN light would be reradiated). This divide became the genesis of *unified schemes*, which will be discussed in Sect. 3.

The emission lines of AGN not only indicate the presence of a powerful ionizing and exciting source in the center, they also indicate the presence of high-velocity gas surrounding the central source. There is a strong dependency on the equivalent width of many lines on luminosity

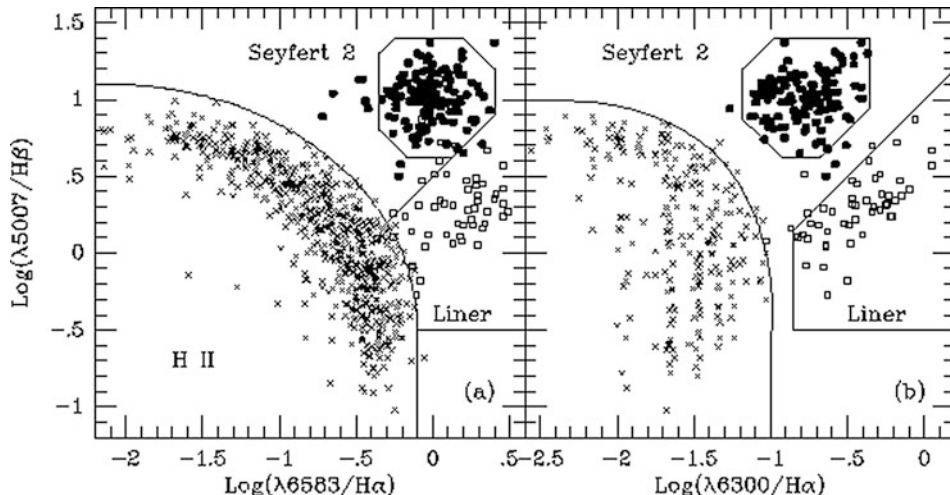


Fig. 7-5

Diagnostic diagrams for all nuclear emission line galaxies with published line ratios, excluding objects with a composite spectrum. Note that Seyfert 1, Seyfert 2, and LINER galaxies separate relatively neatly into the drawn regions, which are determined empirically. A few Seyfert 2s with weak [N II] lines appear outside the region assigned to Seyfert 2s. A few other objects falling in “intermediate” regions deserve a more detailed study (Figure taken from Veron-Cetty and Veron (2000, their Fig. 3))

(Yip et al. 2004), in the sense that more luminous objects tend to have relatively weaker lines. They can also be used to diagnose the physical state of the material in the regions producing the lines – as will be investigated in more detail later in this chapter. **Figure 7-6**, also taken from the SDSS, shows an expanded view, revealing the enormous variety of lines seen in AGN spectra. Many of the lines are blended, so to get quality diagnostics, often high resolution and signal to noise are needed. In addition to the bright emission lines, one also sees other interesting features. In particular, one sees in some of the broad emission lines a “P Cygni” type of profile – that is, the emission line is redshifted, and the blue wing exhibits strong absorption, often with a complex profile. This spectral morphology, seen in about 10% of quasars (known as “broad absorption line” or BAL quasars, discussed in **Sect. 6.2**), is similar to those seen in Be type stars such as their namesake, P Cygni, and in those objects they are interpreted as being due to an outflow, with the emission lines originating in the outermost shell, which is seen relatively unabsorbed, while the absorption lines originating in the portion of the wind that is approaching us. The same interpretation is invoked for AGN as well.

2.3 Radio Emission and the Radio-Loud/Radio-Quiet Divide

The SEDs of AGN come in both radio-loud and radio-quiet varieties, as shown in **Fig. 7-2**. Typical radio-loud AGN have radio continuum emission that is about 1,000 times brighter, relative to the IR-UV continuum, than a typical radio-quiet AGN. However, radio-quiet objects are significantly more numerous, amounting to 80–90% of all AGN.

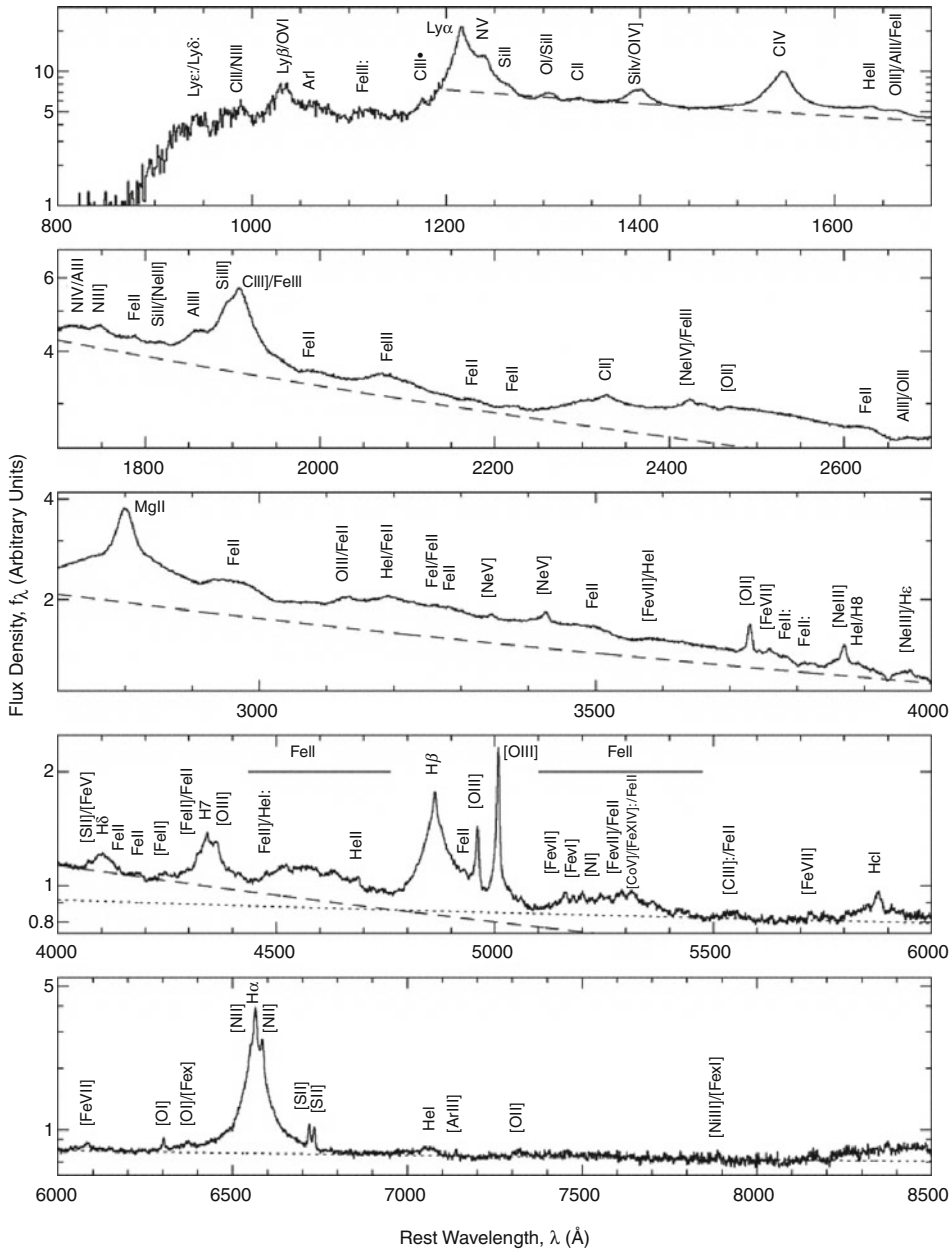


Fig. 7-6

A more detailed look at the composite quasar spectrum shown in Fig. 7-3. Note the wide variety of both broad- and narrow-line features (Figure taken from Van den Berk et al. (2001, their Fig. 6))

In contrast to the continuum at higher energies (far-infrared up to far-UV), which is believed to be dominated by thermal emission from various components of the AGN structure, the radio emission must have a nonthermal origin (☞ Sect. 7). The radio emission from both radio-quiet and radio-loud AGN are roughly power law in shape and display remarkably similar spectral slopes, with $\alpha \sim 0.7$ being typical of the extended structure, while $\alpha \sim 0$ is more typical of the compact, core components. The radio emission is often linearly polarized (both in the extended and core components), with degrees of polarization that can reach into the tens of percent.

2.3.1 Radio-Loud Versus Radio-Quiet: A True Bimodality?

Traditionally, the radio-loud/radio-quiet break has been drawn in terms of the ratio between the emission at 5 GHz and that in the blue (rest frame), with the dividing line being at a ratio $R \equiv F_{\text{5 GHz}}/F_{\text{2,500 \AA}} > 10$ (Kellermann et al. 1989; Stocke et al. 1992). The main reason why this ratio was chosen was observational – AGN were historically found by surveys in the UV or X-ray band, with radio loudness being established by correlating with a radio survey. Up until the last 10 years, the best data showed a bimodality in R , with very few objects having $R \sim 1\text{--}10$. However, more recent data are divided on this issue, and it is not certain whether this division represents a true bimodality or is a product of observational biases in the surveys (see Cirasuolo et al. 2003; Ivezić et al. 2002, 2004 for both sides of this debate, as well as ☞ Fig. 7-7). What is clear is that the fraction of radio-loud objects appears to depend strongly on both the optical luminosity and redshift, with the RLF at $z = 0.5$ declining from $\sim 24.3\%$ to 5.6% (from a sample of 4472 SDSS/FIRST quasars) as luminosity decreases from $M_{\text{2,500}} = -26$ to -22 and the RLF at $M_{\text{2,500}} = -26$ declining from 24.3% to 4.1% as redshift increases from 0.5 to 3 (Jiang et al. 2007).

It is also somewhat unclear what produces this dichotomy, real or not. Sikora et al. (2007) pointed out that there appear to be distinct radio-loud and radio-quiet sequences in the Eddington ratio versus radio-loudness plane, with both sequences showing a similar dependence of R on Eddington ratio. This led them to suggest that the main difference between the two was the spin of the central black hole, a view more recently backed up by general relativity simulations of jet formation in high and low spin environments (Tchekhovskoy et al. 2010; see also ☞ Sect. 7). An alternate view (Körding et al. 2006, 2008) is that the radio-loud and radio-quiet populations represent two different accretion states in a continuum of AGN. The idea behind this latter scenario is the behavior of X-ray binaries, which are known to switch between several states, with the same objects sometimes exhibiting radio jets and sometimes not, depending on their positions in an (X-ray) hardness/intensity diagram. Radio jets are only ejected from X-ray binaries when they are in the high-intensity and hard X-ray spectrum part of the diagram. As the timescales for phenomena around black holes should scale with the mass, one would not expect to be able to observe objects to switch from radio-loud to radio-quiet behavior. Importantly, however, the two scenarios given here may not be mutually exclusive, as pointed out by Sikora et al. (2007); it may be that the black hole spin governs the efficiency of the jet production process, but that a second factor may determine whether a jet is produced.

2.3.2 Radio Morphology

The radio morphology of active galaxies is quite varied, but several characteristics appear common to a variety of classes. Typically, one sees highly collimated outflows on one or both

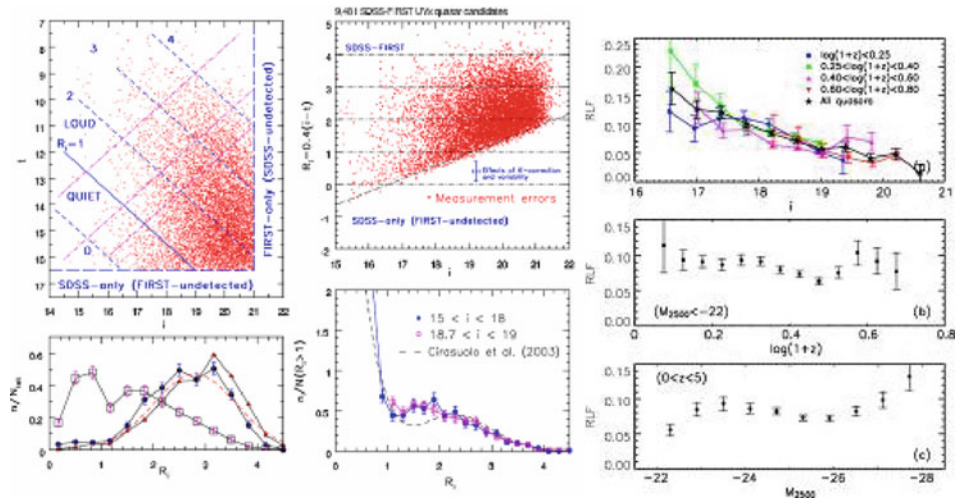


Fig. 7-7

At left, two analyses of the quasar radio dichotomy as carried out with a sample of 10,000 objects from the SDSS and FIRST. In the top left panel, which shows the source distribution in the t (radio AB magnitude) versus i (optical magnitude) plane, the diagonal dot-dashed lines define regions that were used to determine the $R_i = 0.4$ ($i - t$) distribution. The R_i histograms for these regions, marked by filled circles and triangles in the bottom left panel, were interpreted as evidence for a quasar radio dichotomy. The histogram marked by open squares shows the R_i distribution for sources with $i < 18$ and is shown as an example of a biased estimate of the R_i distribution. The upper right panel shows the R_i versus i distribution for the same SDSS-FIRST dataset as in the two left panels (note that this diagram is a sheared, and not simply a rotated, version of the diagram in the top left panel). The large dot in the top right panel illustrates the typical measurement uncertainty. The two histograms in the bottom right panel (symbols with error bars) show $p(R_i|i)$ for two ranges of i , as marked. The dashed line in the bottom right panel shows a best-fit result for $p(R_i|i)$ by Cirasuolo et al. (2003), displayed here for illustration (it is shifted left by 0.4 mag to account for different optical bands, i vs. B). Figure taken from Ivezić et al. (2002, their Fig. 1). At far right, the radio-loud/radio-quiet fraction is shown, both as a function of magnitude and as a function of redshift (Figure taken from Jiang et al. (2007, their Fig. 5))

sides of the nucleus, terminating in diffuse lobes. These lobes are often far larger than the galaxy in which the active nucleus resides and can extend for many hundreds of kiloparsecs. Several classic examples are shown in [Fig. 7-8](#). 3C 341 and Cygnus A are examples of Fanaroff-Riley type II (FR II) sources: highly luminous (the classical definition is $P_{178 \text{ MHz}} > 10^{25} \text{ W Hz}^{-1}$, as laid out by Fanaroff and Riley (1974)), with lobes that have an edge-brightened morphology, terminate in hotspots, and have fairly straight large-scale morphology. Less powerful sources ($P_{178 \text{ MHz}} < 10^{25} \text{ W Hz}^{-1}$) do not have as extreme a morphology. Two examples of these Fanaroff-Riley type I (FR I) sources are shown in [Fig. 7-8](#), namely, M87 and 3C 31. The morphological differences between FR I and FR IIs are obvious: while both classes show jets that extend for many kiloparsecs, in FR Is, one sees obvious bends and a much more edge-dimmed morphology than seen in FR IIs, usually with one or both lobes lacking obvious hotspots.

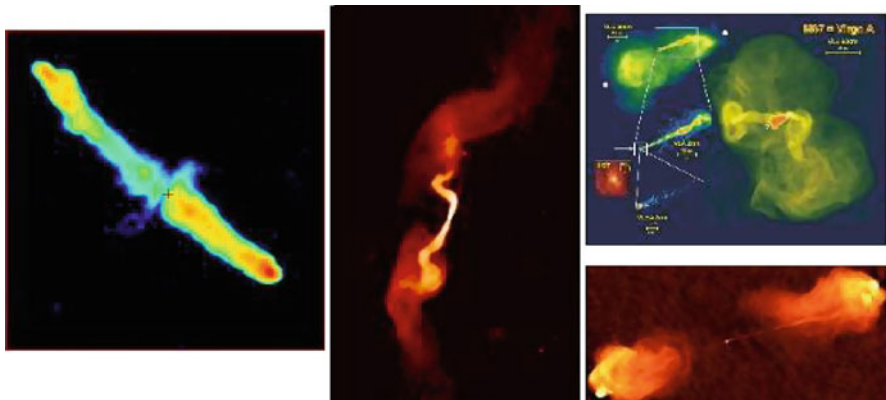


Fig. 7-8

Four radio galaxies illustrating the variety of radio morphologies seen in these objects. At left, we show 3C 341, an FR II radio galaxy. In the middle panel, we show 3C 31, an FR I radio galaxy. Note its edge-dimmed morphology and bent jets. At top right, we show several views of M87, an FR I; this includes images at several resolutions from the VLA as well as an HST image. In the pseudocolor images, red colors indicate the highest intensity, while blue indicates the lowest intensity. At bottom right, we show the FR II galaxy Cygnus A (The three images at right are courtesy of NRAO/AUI, while the image at left is taken from Leahy and Perley (1991))

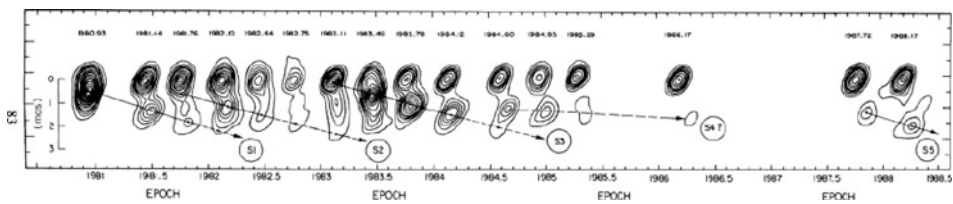


Fig. 7-9

Images of the nuclear regions of BL Lacertae over several years. Motions for several components are pointed out. Note that at the distance of BL Lacertae, 1 mas = 1.381 pc, so that an angular speed of 1 mas year^{-1} works out to an apparent speed of $4c$ (Figure from Mutel et al. (1990, their Fig. 1))

The jets of both FR I and FR II radio sources are collimated on small scales (within 1 pc of the central engine; see [Sect. 7](#)) and carry a major fraction of the kinetic flux and angular momentum ([Sect. 4](#)) generated by the central source with them. They affect the host galaxies of the AGN quite significantly as well, often triggering star formation in their path as well as other shocks, as witnessed by optical emission line shocks near the path of the jets in nearby radio galaxies, as well as the high-redshift “alignment effect” (see [Chap. 11](#)).

An important property of relativistic jets is that they display *apparent superluminal motion* on parsec scales. An example is shown in [Fig. 7-9](#) for the prototype BL Lac object, BL Lacertae. As can be seen, several components are tracked over more than 10 years; each is apparently moving at several times the speed of light.



Fig. 7-10

Geometry illustrating relativistic effects in jets

This is actually a relativistic effect. The geometry is shown in Fig. 7-10, with an object moving at speed v at a small angle θ to the line of sight. The time of origin is chosen arbitrarily as $t = 0$. At time $t = t_e$, the component has moved a distance vt_e . As shown, the observed separation will be the transverse component of the distance,

$$\Delta r = vt_e \sin \theta \quad (7.1)$$

However at time t_e , the component has moved both in the transverse direction as well as along our line of sight and is closer to Earth than at $t = 0$. Photons emitted at times $t = 0$ and $t = t_e$ will reach us at times separated by

$$\Delta t = t_e - \frac{vt_e \sin \theta}{c} = t_e (1 - \beta \cos \theta) \quad (7.2)$$

where $\beta = v/c$ is the velocity in units of the speed of light. Thus if (7.1) and (7.2) are divided, the apparent velocity is obtained:

$$v_{\text{app}} = \frac{\Delta r}{\Delta t} = \frac{v \sin \theta}{1 - \beta \cos \theta} \quad (7.3)$$

This result was first pointed out by Sir Martin Rees in 1966 (Rees 1966) – a full decade before it was first observed. There are two results here: first of all, the observed velocity is a function both of the true velocity as well as the direction of the motion relative to our line of sight, and second, that (through a trick of geometry) it is possible to observe speeds that seem to be faster than that of light without an object ever actually traveling faster than light. Further exploration of equation (7.3) shows that a maximum velocity is found at a value $\sin \theta_{\max} = 1/\Gamma$, where γ is the Lorentz factor $\Gamma = (1 - v^2/c^2)^{-1/2}$. (It should be noted that very often in the literature one sees the capital letters as referring to bulk motion within the jet, whereas particle velocities are expressed by small letters. This convention is adopted herein). When the viewing angle $\theta = \theta_{\max}$, the apparent velocity is then $v_{\text{app}} = \Gamma v$. Thus it is quite possible for us to observe speeds much larger than c , as in M87. In fact, speeds as high as $40c$ have been observed in high-frequency VLBI observations of BL Lac objects (e.g., Jorstad et al. 2001, 2005).

2.4 Infrared Emission

The infrared emissions of active galaxies have been studied with a number of tools. However, the increased sensitivity of Spitzer, combined with the angular resolution possible with 10-m class ground-based telescopes, has spawned a revolution over the last decade. In the infrared, one finds much of the power emitted by AGN – typically upwards of 25%, as shown by [Fig. 7-2](#). This fraction varies from 10% at a minimum to more than 50% in some objects, depending on the amount of obscuration within the AGN as well as the amount of star formation in the surrounding galaxy. Here the latter topic, which is studied in detail in the [Chap. 11](#), is not discussed; however, it does bear mentioning in the global sense. Infrared light in AGN typically originates in warm dust, which is believed to be heated by the central AGN and also obscuring some fraction of its emission, as discussed further in [Sect. 3](#).

The continuum emission of AGN in the infrared is characterized by three main features. These include (i) a minimum at $\sim 1\text{--}2 \mu\text{m}$, corresponding to the sublimation temperature of the most refractory dust (1,000–2,000 K, depending on the composition of the dust grains); (ii) an “IR bump,” somewhere between a few up to $100 \mu\text{m}$. This bump can have a variety of morphologies, from a narrow, nearly single-temperature blackbody shape in some objects to a flat morphology that requires multiple emitting components. This component is due to the thermal emission of dust, with temperatures usually between 50 and 1,000 K, and in radio-quiet objects, (iii) a steep decline ($\alpha > 3$) at large wavelengths, typical of the low energy spectrum of a gray emitter (Chini et al. 1989). This latter feature is not present in radio-loud objects, wherein the far-infrared and submillimeter nonthermal emission (discussed in [Sects. 2.3](#) and [7](#)) takes over.

Underlying the seemingly simple picture described above is a considerable amount of complexity. There are a broad range of spectral features in the infrared, and moreover, the mid-IR is also the site of a great deal of spatial complexity within the central regions of both the host galaxy as well as the AGN. In [Fig. 7-11](#), average mid-IR spectra of Seyferts and starburst galaxies are shown, as well as six example spectra. Several things are seen in this figure. Both the Seyfert and starburst spectra possess an overarching thermal continuum, as already discussed above; however, the typical starburst possesses a considerable amount of additional cold gas, likely due to the massive amounts of star formation going on within it. Also seen in the Seyfert spectra are forbidden lines from high-ionization species, notably [Ne V] and [O IV]. This is a strong sign of a powerful exciting source in the nucleus. Also present in all of the spectra are molecular emission features, notably those due to PAH molecules. These indicate that the dusty regions that emit in the mid-IR are rich in molecular gas and also that it is not easy to completely separate the AGN from the surrounding host galaxy in this band, either physically or phenomenologically. The final set of features that are notable in all of the spectra shown in [Fig. 7-11](#) are a pair of features due to dusty silicates, the first located at $10 \mu\text{m}$ and the second at $18 \mu\text{m}$. These are seen in absorption in some objects, notably Sey 2s, while in Sey 1s, they are typically seen in emission.

The stable, low-noise nature of the space environment gives space-based telescopes an enormous advantage when it comes to sensitivity. Ground-based telescopes are limited by thermal emission from the Earth’s atmosphere as well as molecular features from atmospheric material, neither of which are a factor in space, where the background is orders of magnitude lower. Unfortunately, however, *Spitzer* was only a 0.85-m telescope, and as a result it does not have the angular resolution to separate the inner regions of the AGN from the nearby regions of the surrounding galaxy. To accomplish this task, one must currently resort to imaging and spectroscopy with ground-based telescopes, which are essentially diffraction limited

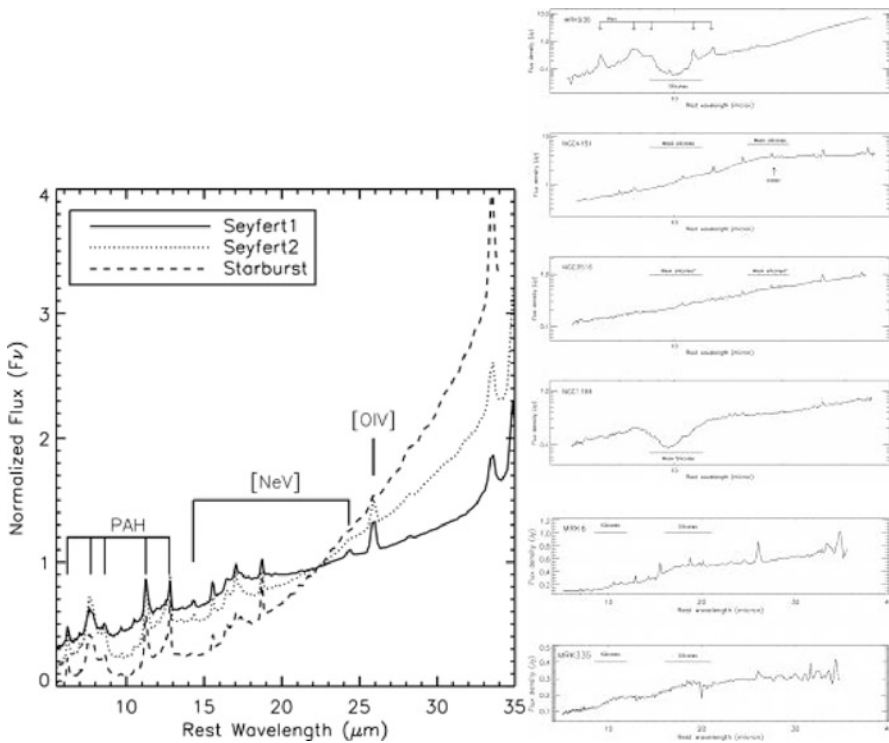


Fig. 7-11

At left, average 5–35-mm spectra of Seyferts and Starburst galaxies obtained with Spitzer. Figure from Wu et al. (2009, their Fig. 4). At right, example spectra for Seyferts in six classes, obtained with Spitzer. Figure from Buchanan et al. (2006, their Fig. 8). Spectral features are pointed out in each case

in the 10- and 20- μm windows. With ground-based 8–10-m class telescopes, angular resolutions $\sim 0.3''$ at 10 μm can be reached, a factor of 10 better than what *Spitzer* is capable of. In the mid-IR, JWST will be capable of similar resolution once launched, but much greater sensitivity; however, it will lack polarimetric capability.

An example of this work is shown in [Fig. 7-12](#) for the prototype Sey 2 NGC 1068 (Mason et al. 2006). The spectra cover the nucleus and central $6.0'' \times 0.4''$ of the ionization cones. The spectra extracted in $0.4''$ (~ 30 pc) steps along the slit reveal striking variations in continuum slope, silicate feature profile and depth, and fine structure line fluxes, illustrating the complexity of the circumnuclear regions of this galaxy at MIR wavelengths. A comparison of photometry in various apertures reveals two distinct components: a compact (radius < 15 pc), bright source within the central $0.4'' \times 0.4''$ and extended, lower brightness emission. The compact source is identified as the torus (see [Sect. 6](#) for discussion) and the diffuse component as warm or hot, AGN-heated dust located mostly in the ionization cones ([Sect. 4](#)). While the torus emission dominates the flux observed in the NIR, the MIR flux measured with apertures larger than about $1''$ is dominated instead by the dust emission from the ionization cones; in spite of its higher brightness, the torus contributes $< 30\%$ of the $11.6\text{-}\mu\text{m}$ flux contained in the central $1.2''$. Thus if one attempts to determine the torus SED using space-based data alone, one is significantly compromised by contamination from the extended emission. Mid-IR interferometry

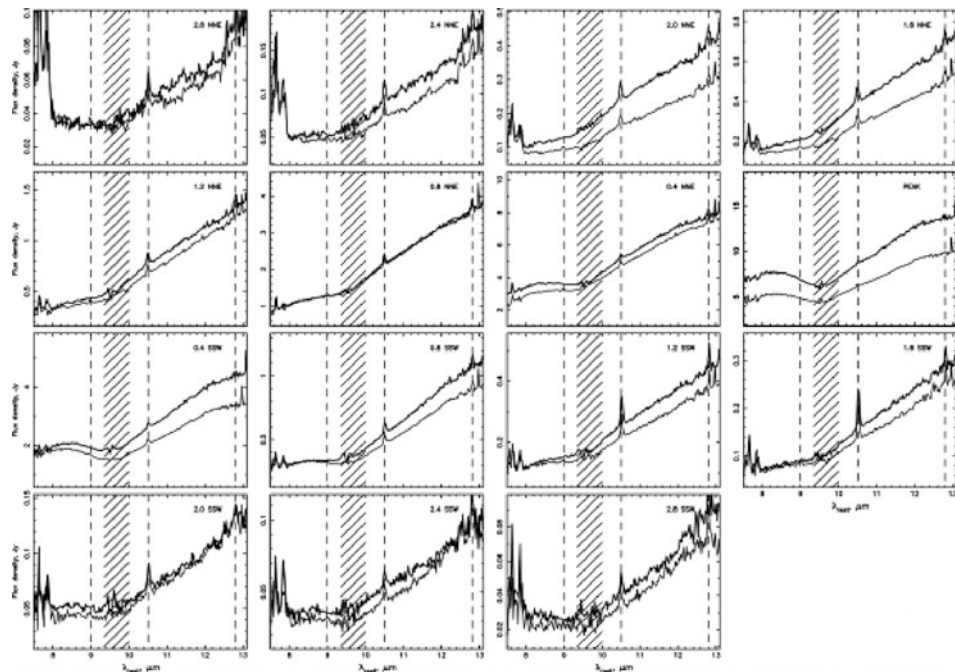


Fig. 7.12

Spatially resolved spectroscopy of the Sey 2 galaxy NGC 1068 obtained with Gemini-North + Michelle. The data are shown in $0.4''$ segments along a slit that extended along the main mid-IR emission axis (PA 20°). All positions are relative to the mid-IR peak. *Black* and *gray* lines refer to two different epochs. Note how the shape of the spectrum changes within the $7.5\text{--}13\text{-}\mu\text{m}$ window – both the depth of the silicate feature (shaded region) as well as the luminosity of emission lines (e.g., [S IV] $10.5\text{ }\mu\text{m}$ and [Ar III] $8.99\text{ }\mu\text{m}$) vary. This emphasizes how critical it is to attain high angular resolution when studying the AGN in mid-IR (Figure taken from Mason et al. (2006, their Fig. 2))

(Poncelet et al. 2006; Jaffe et al. 2004) also supports a very small central obscuring source for NGC 1068, placing a severe limit of only ~ 3 pc on its size. Work on a variety of other sources is showing similar results: the nuclear obscuration in AGN is concentrated in the innermost few parsecs (e.g., Radomski et al. 2003, 2008; Packham et al. 2005; Roche et al. 2006, 2007; Meisenheimer et al. 2007; Tristram et al. 2007, 2009; Poncelet et al. 2007, 2008), although in a few sources, more extended nuclear dust is seen (e.g., IC 5063, Young et al. 2007). This places severe constraints on unification models, as discussed in **Sect. 6**, and also directly links the regions of heaviest mid-IR obscuration to the observations of water masers by Greenhill et al. (1996) (discussed below).

2.5 X-Ray and Higher-Energy Emission

The X-ray and gamma-ray properties of active galactic nuclei are complex. Emission is seen from the galactic absorption cutoff at ~ 0.1 keV up to a few hundred keV. This emission contains

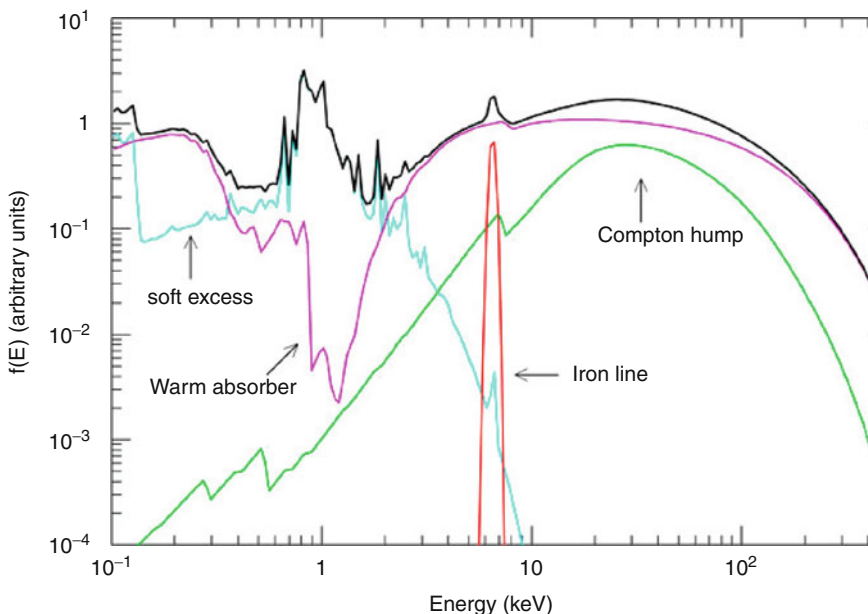


Fig. 7-13

Average total spectrum (thick black line) and main components (thin grey lines) in the X-ray spectrum of a type I AGN. The main primary continuum component is a power law with an high energy cutoff at $E \sim 100\text{--}300\text{ keV}$, absorbed at soft energies by warm gas with $N_H \sim 10^{21}\text{--}10^{23}\text{ cm}^{-2}$. A cold reflection component is also shown. The most relevant narrow feature is the iron K α emission line at 6.4 keV. Finally, a “soft excess” is shown due to thermal emission of a Compton thin plasma with temperature $kT \sim 0.1\text{--}1\text{ keV}$ (Figure taken from Risaliti and Elvis (2004))

the signature of a number of processes, discussed in this section. Figure 7-13 summarizes the various emission and absorption components that tend to be present in AGN X-ray spectra.

At zeroth order, the intrinsic continuum shape is a power law that extends from about 1 keV to over 100 keV. The typical spectral index of this power law is between $\alpha = 0.8$ and $\alpha = 1$, both for lower luminosity Seyfert galaxies as well as quasars. A somewhat flatter spectral shape is seen for radio-loud AGN, typically between $\alpha = 0.5$ and $\alpha = 0.7$. These spectral indices are remarkably constant with redshift, according to work done on the SDSS AGN (Green et al. 2009). The difference between radio-loud and radio-quiet X-ray spectral slopes is believed to be due to the additional inverse-Compton scattering taking place within the jet’s inner regions. BeppoSAX spectra reveal that this power law cuts off exponentially at energies between 80 and 300 keV for most AGN, with the exception of some radio-loud objects (in particular blazars, which will be discussed later).

Further examination reveals that considerable complexity underlies this power law. At the soft end of the spectrum, one often observes a quasi-thermal component (the so-called soft excess), with characteristic temperature $kT \sim 0.2\text{--}1\text{ keV}$. A second feature is seen between 10 and 50 keV, namely, a “hump” believed to be due to Compton reflection in the accretion disk’s corona (see Sect. 4.3). Tied to this reflection “hump” is a warm absorber component seen in about $\sim 50\%$ of Seyfert 1 galaxies. This feature is quite complex, featuring a variety of line

features, most notably “edges” due to hydrogen and helium-like oxygen, but also a wide variety of other highly ionized species, visible in deep, higher-resolution spectra. A variety of emission lines are also present in these objects. Most prominent among the emission lines is the Fe K α line at a rest energy of 6.4 keV; however, a number of other emission lines are also seen in deep, higher-resolution spectra, including K- and L-shell features of iron, oxygen, silicon, magnesium and other elements. An example of a high-resolution spectrum is shown in [Fig. 7-14](#).

These generalities apply to many objects; however, in a large number of AGN, one sees absorption much heavier than galactic. Obscuration in the X-rays can be due to photoelectric absorption (which dominates below a few keV) and Compton scattering (dominant above 7 keV). The observed spectral properties will depend on the amount of absorbing material present along our line of sight: column densities below $\sim 1.5 \times 10^{24}$ cm $^{-2}$ produce a cutoff at energies between 1 and 10 keV, with higher-energy cutoffs observed in more obscured objects. In this case, the source is called “Compton thin.” However, at higher column densities, the source is optically thick (and hence faint) up to several tens of keV. In this case the source is called “Compton thick,” and the main spectral features seen are a prominent Fe K α line with equivalent width $\sim 1\text{--}3$ keV and a reflected and/or scattered continuum. For less obscured sources, the Fe K α line typically has a much lower equivalent width. These properties are summarized in [Fig. 7-15](#).

2.6 Variability

Another important property of AGN is their variability, a property first discovered in the late 1960s (Cannon et al. 1968; Kinman 1968; Pacholczyk and Wyemann 1968; Barnes 1968; Selove 1969; Zaitseva and Lyutyi 1969; Babadzhanyants and Hagen-Thorn 1969) in the optical, and a couple years later in the radio (Stull 1970; Ross 1970). This variability has since been found to extend to all wavebands (see Ulrich et al. 1997 for a review), in both continuum and line emission. Variability in AGN is seen on all timescales (see [Fig. 7-16](#) for examples), ranging from years down to days, with a variety of amplitudes as well. In some objects (BL Lacs and blazars), violent variability is a defining characteristic, with flux varying by factors of several in short time periods.

Variability on such short timescales puts tight constraints on the size of the emitting region – since nothing can move faster than the speed of light, an object that varies within a few days must be no larger than a few light-days in diameter. This topic will be discussed in depth below, along with the nature of the central object and the need for a black hole. However, it is worthwhile to mention at this time that the variability of AGN is one of the strongest reasons behind the fact that an alternate model, advocated by Terlevich et al. (1992), is not well regarded in the literature. Under the Terlevich et al. model, AGN are viewed as giant young stellar clusters, and variability must be explained as the result of nova and supernova explosions generating rapidly evolving remnants due to the interaction between their ejecta and a high density circumstellar environment. This model is supported by the overall similarity of the optical spectra and compact supernova remnants (e.g., Filippenko 1989). What this model has difficulty explaining is not the overall character of the variations (Aretxaga and Terlevich 1994; Cristiani et al. 1996), which can be explained by a combination of complicated processes that could arise either in the structure discussed in this chapter or in separate, interstellar processes such as novae or supernovae, but rather the combination of small variability timescale and massive luminosity. For quasars, the variability properties seen require that more than 10¹² solar luminosities, spanning

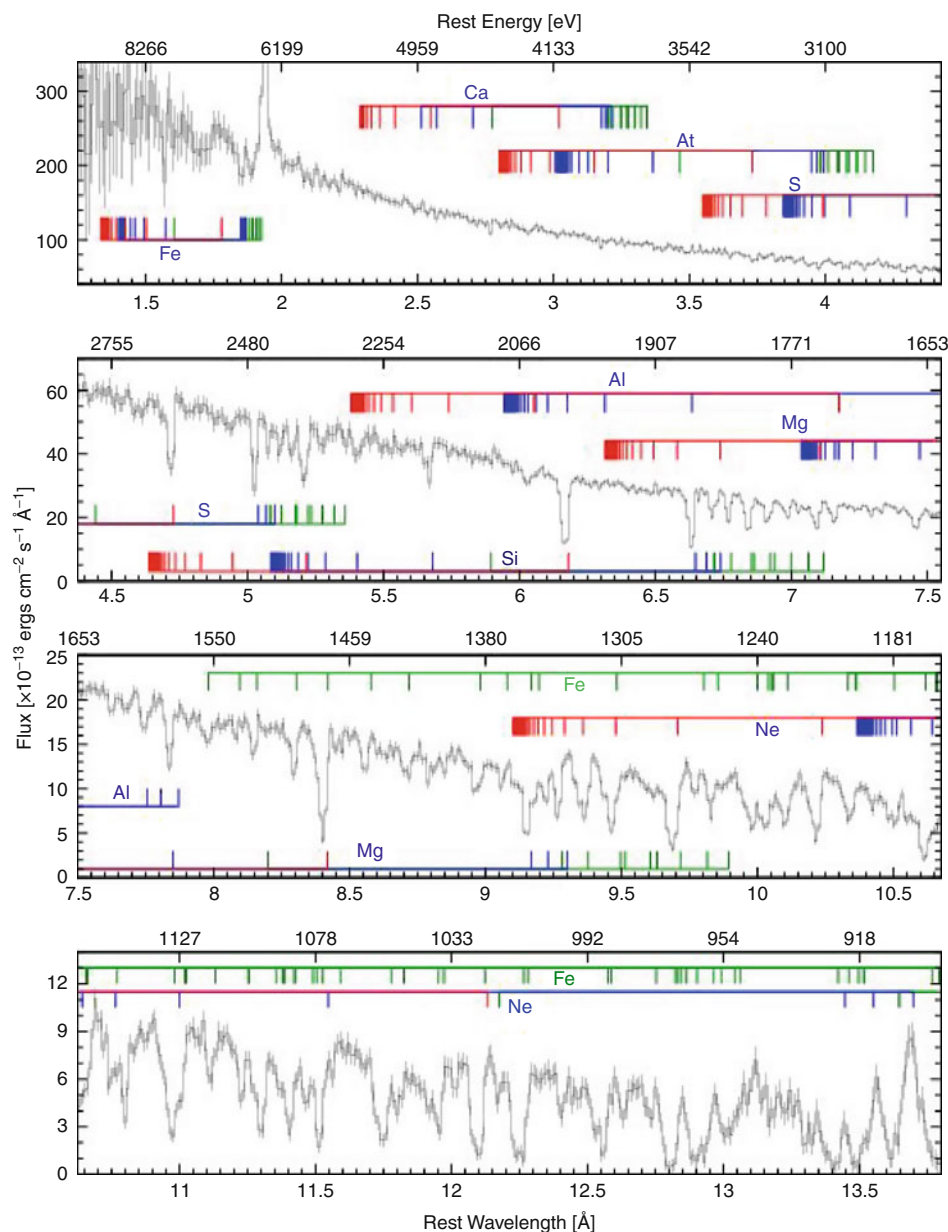


Fig. 7-14

A high-resolution X-ray spectrum of the Seyfert 2 galaxy, NGC 3783. This spectrum was obtained with the high-energy transmission grating spectrometer (HETGS) aboard the Chandra X-ray Observatory (Kaspi et al. 2002). Note the wide variety of line features

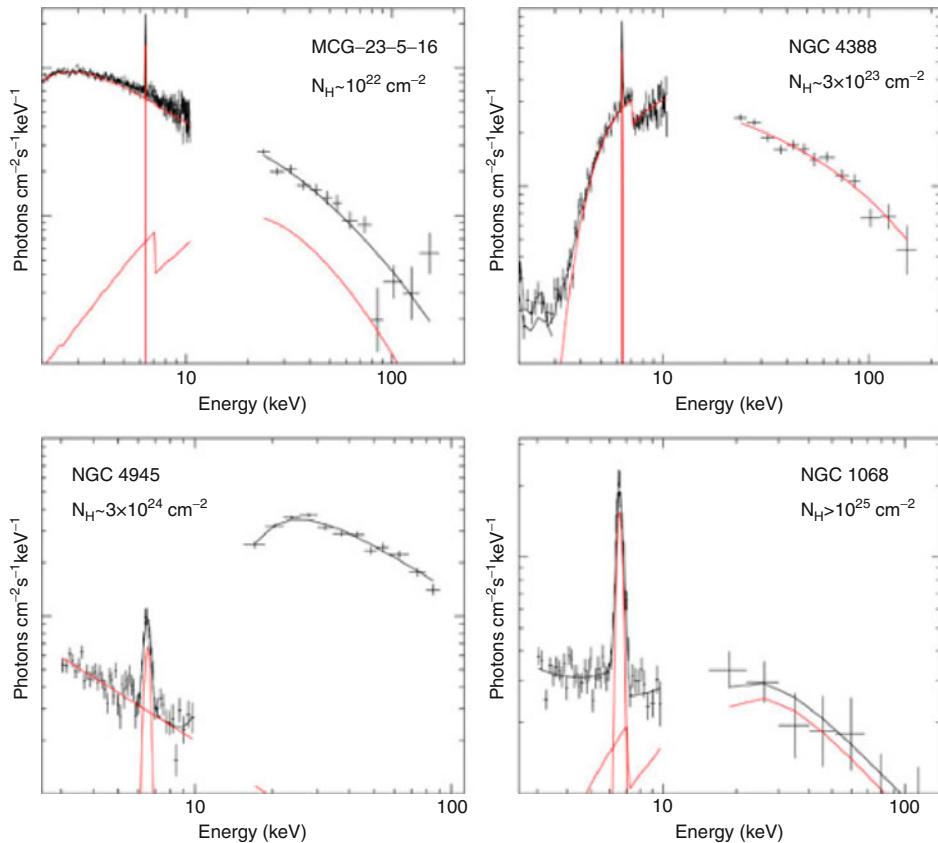


Fig. 7-15

Four 2–100-keV BeppoSAX best-fit X-ray spectra of Seyfert 2 galaxies. Main components of the best-fit models are also shown. MCG-5-23-16 and NGC 4388 (Risaliti 2002) are “Compton thin,” that is, they are dominated by the primary emission down to a few keV. In MCG-5-23-16, a cold reflection component also gives a measurable contribution. The continuum in the Compton-thick source NGC 4945 (Guainazzi et al. 2000) is due to a warm reflection component in the 2–10-keV range, while at higher energies the intrinsic component emerges. Note the high ratio between the 10–100-keV and the 2–10-keV emission as compared with the Compton-thin sources. NGC 1068, also Compton-thick (Matt et al. 1997), shows a cold reflection and a warm reflection component. Equivalent widths of the iron K α line are ~ 100 eV in MCG-5-23-16, ~ 500 eV in NGC 4388, and 1–2 keV in NGC 4945 and NGC 1068

several decades in frequency, be radiated in a region no larger than a few light days. Explaining such large variations by a series of supernova-related explosions requires an extreme stellar density, large enough that the cluster would be unstable to gravitational collapse over short timescales.

Importantly, AGN variability is often correlated across wavebands (e.g., Fig. 7-17). This indicates that the processes responsible for the emission in these different bands must be connected somehow. Interestingly, however, the variability seen in different bands,

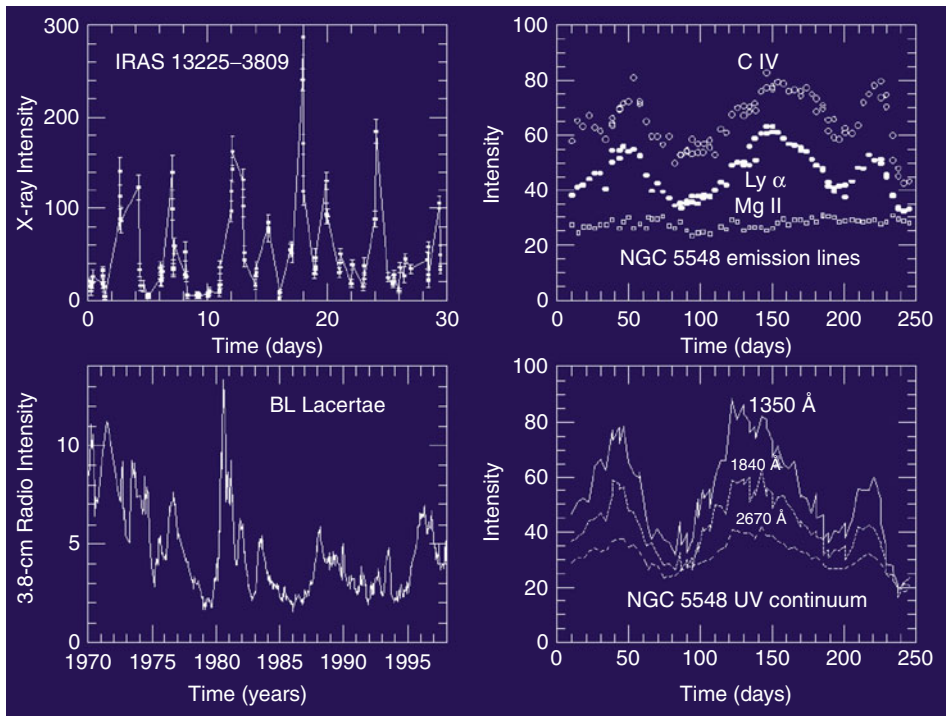


Fig. 7-16

Examples of variability in different active galaxies. The examples include two Seyferts and one BL Lacertae object (Figure taken from W. Keel <http://astronomy.ua.edu/keel/agn>)

while correlated, is offset somewhat in time – that is, very often it is found that shorter wavelengths lead the emission seen in softer bands.

3 The Overall Structure: Unified Models

With the large zoo of AGN properties outlined in the previous section, there is a strong motivation to explain them all through a single, unified structure that has a minimum of different features. It was out of this desire that unified schemes were born. From the outset it was clear that any unified scheme had to be able to generate the massive luminosity observed within a small region – light-days or smaller. The scheme also had to be reasonably stable for millions of years. That last fact rules out any origin in a collection of normal stars (as proposed by Terlevich in 1992), as the generation of up to 10^{12} solar luminosities by thermonuclear fusion would require of order 10^{12} solar masses within that small volume (thus being unstable to gravitational collapse in a very short time) and would have no way to explain the variability without positing the existence of novae or supernovae. The modern view centers around a supermassive black hole and posits a nonaxisymmetric system, where the properties observed depend entirely on the perspective.

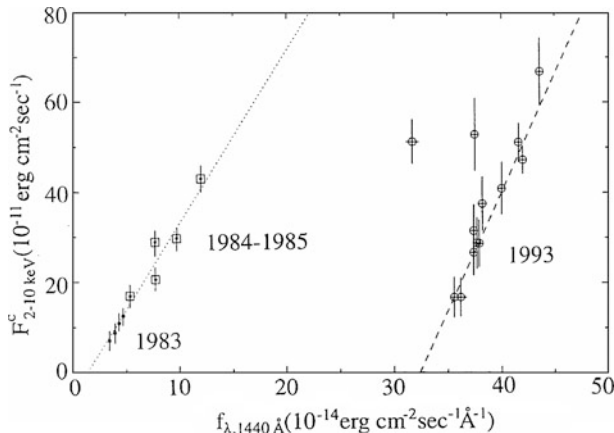


Fig. 7-17

X-ray flux (absorption corrected, 2–10 keV) versus UV flux ($1,440 \text{ \AA}$) for NGC 4151. Right: ASCA observations in November 30–December 13, 1993, with best-fitting linear correlation. Left: EXOSAT observations in December 16, 1984, to January 28, 1985 (large crosses), and November 7–19, 1983 (small crosses), with best-fitting linear correlation. The good correlation of the UV and X-ray flux on a timescale of weeks and months breaks down at long (years) and short (days) timescales (Ulrich et al. (1997), their Fig. 3)

3.1 The Basic Scheme

The basic structure, illustrated in [Fig. 7-18](#), is seen in both radio-loud and radio-quiet objects and features a supermassive black hole at the center, accreting material, possibly (although not necessarily; see [Sect. 4](#)) through a disk. Accretion is an elegant way to generate enormous luminosities within the small volumes required by the observed variability as it offers the potential of converting up to half of the gravitational potential energy from accreting matter into light and heat in the process. Surrounding the accretion disk are various layers of warm gas, which would explain the broad and narrow emission line features. These two sets of gas clouds need to be located at vastly different distances from the central black hole, because, as indicated in future discussion, detailed modeling indicates that the physical conditions in the two regions are vastly different.

A critical feature of this model is the presence of a large-scale obscuration region. [Figure 7-18](#) illustrates this obscuration as having a uniform, optically and geometrically thick toroidal structure, which is the simplest model. However, this geometry is by no means required, and in fact the most modern data indicate that a patchy geometry may be more likely, as discussed in [Sect. 6](#). This obscuration region would need to be dusty and possibly molecular gas-rich, but whatever its geometry, has gained the name “torus” in the literature. Its key feature is to obscure the view of the broad-line clouds from some points of view. Objects that are viewed through the dusty, obscuring clouds would be seen to have Seyfert 2 type spectra, whether with or without a radio jet, while objects viewed at a more direct angle would have broad-line spectra, more typical of Seyfert 1s. Intermediate objects would be possible depending on how much obscuring material was along our line of sight.

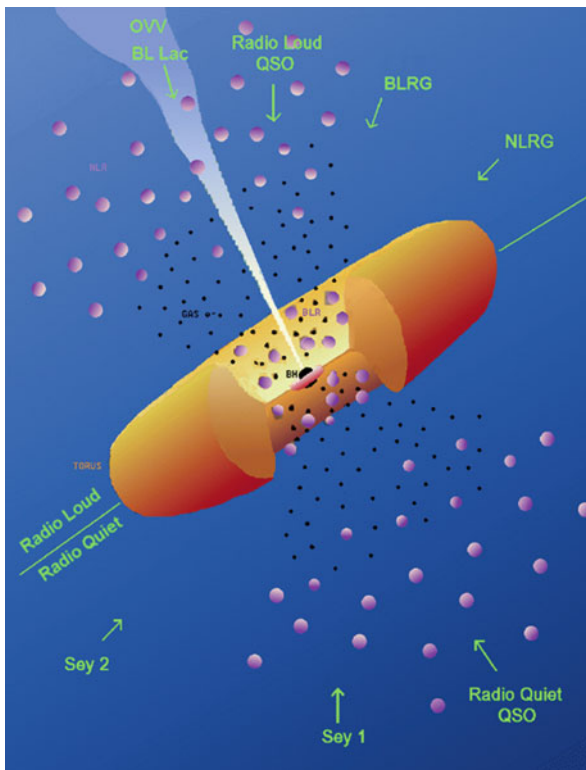


Fig. 7-18

The basic structure for active galaxies as postulated by unified schemes. This figure is not to scale, nor is the geometry for all regions settled, as discussed in the text. Nevertheless, it illustrates the basic geometry and aspect-dependent nature of the scheme (Figure courtesy of P. Padovani)

The final piece of this picture, present only for radio-loud objects, is bipolar jets that emerge from the nuclear regions at relativistic speeds. For objects where the jet was seen close to our line of sight, relativity would increase the apparent luminosity of the source so that the source was dominated by the jet properties. The result in this case would be what is known as a *blazar*, a radio-loud object with weaker or no emission lines, apparent superluminal motion and extreme variability. The most extreme of these observationally are the BL Lacertae objects, which are distinguished by their featureless optical spectra (see example in [Fig. 7-4](#)). Under unified schemes, BL Lacs represent low-luminosity, FR 1 radio galaxies viewed at small angles to the jet axis, while a subclass of quasars, the FSRQ or flat-spectrum radio quasars (also called OVV or optically violent variables), represent the FR 2 radio galaxies viewed at small angles to the jet axis. FSRQ are more luminous than BL Lacs and do not have their featureless optical spectra but share with BL Lacs the properties of superluminal motion and violent multiwaveband variability.

Special relativity has a number of important consequences for high-velocity jets. A little manipulation will show that a number of other interesting effects are observed for a relativistically approaching object (i.e., a jet component). The observed is also distorted

for these sources, as are the frequencies of the radiation observed:

$$\Delta t_{\text{app}} = \delta^{-1} \Delta t \quad (7.4)$$

$$\nu_{\text{app}} = \delta \nu \quad (7.5)$$

where the commonly used *Doppler factor* is $\delta = [\Gamma(1 - \beta \cos \theta)]^{-1}$. However, perhaps most importantly, the luminosity one would infer (if one naively assumes uniform illumination over 4π steradians) differs greatly from that truly emitted:

$$L_{\text{app}} = \delta^p L \quad (7.6)$$

where the exponent p depends on the source's morphology and spectral index α . This last relation, often referred to as *Doppler boosting* or *beaming*, arises because the product of intensity and frequency cubed, $I\nu^3$, can be shown to be a Lorentz invariant. For a spherical source, $p = 3 + \alpha$, whereas for a cylindrical morphology, $p = 2 + \alpha$. Thus for a relatively modest bulk Lorentz factor $\gamma_{\text{bulk}} = 10$, it is possible to infer luminosities up to 10,000 times higher if one is in the beaming cone. In Fig. 7-19, all three of these effects are plotted (along with

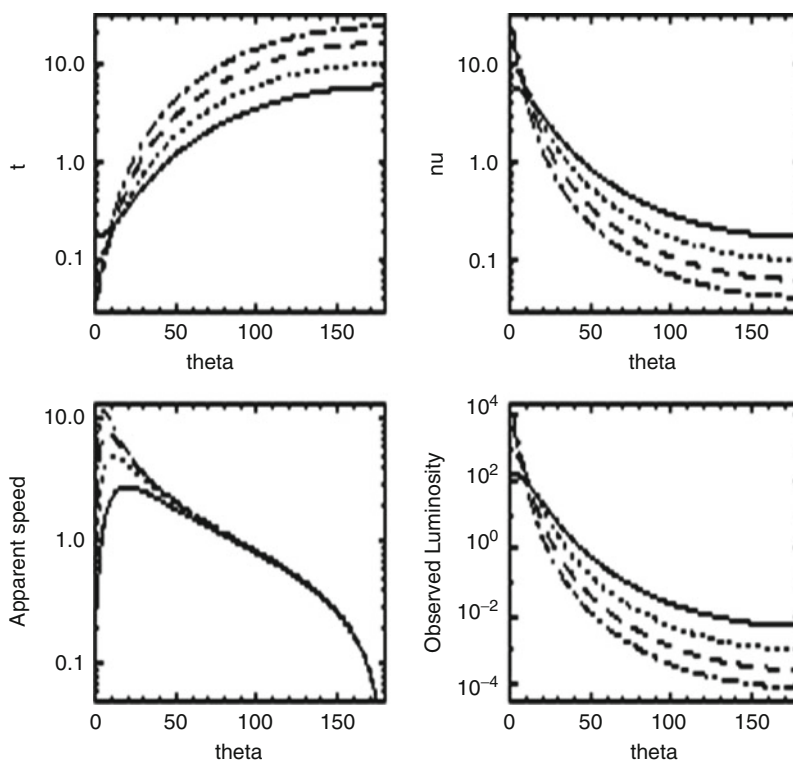


Fig. 7-19

Relativistic effects predicted by unified schemes: time dilation (upper left), frequency shift (upper right), apparent superluminal motion (lower left), and Doppler boosting (lower right) plotted versus the viewing angle in degrees. The tracks shown represent Lorentz factors $\gamma_{\text{bulk}} = 3, 5, 8, 12$

superluminal motion, previously explored in (Sect. 2.3) versus the viewing angle θ for $\gamma_{\text{bulk}} = 3, 5, 8, 12$. As can be seen, significant boosting is obtained for a fairly large range of viewing angles, and even for relatively modest values of γ , one can easily obtain significant Doppler boosting.

3.2 Evidence for Type 1/Type 2 Unification

The evidence supporting this view, known variously as *AGN unification* or the *unified scheme*, is strong and comes from a variety of avenues. In this section and the next, some of the strongest evidence for unified schemes is described.

If indeed the broad-line region of Sey 2 galaxies is hidden from view by dusty obscuration regions, one would expect to be able to directly detect evidence of silicates in the infrared spectra of these objects, as well as emission features from molecular features such as PAH and H₂. Observations of numerous type 2 AGN with *Spitzer* have revealed direct evidence of these features. (Figure 7-20 shows an example of such a spectrum (Armus et al. 2006), specifically for the Seyfert 2 NGC 6240. As can be seen, this spectrum shows strong silicate absorption features around 10 and 18 μm . Equally important, these same features are detected in *emission* in Seyfert 1s, exactly as would be predicted if dust clouds are obscuring our view of the central regions in these objects.

It should be noted, however, that while the *Spitzer* spectra just mentioned indicate the presence of an optically thick obscuring structure, they do not say anything about *what* is being obscured. Thus a second piece of evidence is required. This is provided by spectropolarimetry (Antonucci and Miller 1985; Antonucci 1983; Miller et al. 1991). Spectropolarimetry is a key diagnostic because it takes advantage of the fact that the obscuring region will scatter some fraction of the background region's light, and this scattered light will be polarized. (Figure 7-21 shows the detection of this scattered light for the Seyfert 2 galaxy NGC 1068 (Antonucci and Miller 1985). As can be seen, while the total intensity spectrum of this object shows only very weak H β and other Balmer lines, the broadness of these features is not obvious in total intensity. However, a completely different picture emerges in the polarized light spectrum, where broad Balmer lines typical of type 1 objects are seen, while the narrow [O III] lines are unchanged in strength. This directly indicates that the light intercepted and scattered by the dust in the torus, comes from the broad-line region.

Subsequent observations have revealed polarized broad-line emission in many other type 2 objects, both radio-loud and radio-quiet. In radio-loud objects, there is additional information, allowing us to infer the orientation of this obscuring medium relative to the radio jets. For example, in 3C 234 (Antonucci 1984) and IC 5063, scattered broad-line emission is detected, with the plane of polarization being perpendicular to the axis of the jets. This is expected if a type 1 nucleus is at least partially obscured by optically thick dust clouds whose axis coincides with the radio jet axis. Interestingly, spectroscopy of narrow-line radio galaxies also reveals that the luminosity of the obscured region is quasar-like (e.g., di Serego Alighieri et al. 1994; Goodrich and Cohen 1992; Antonucci et al. 1994, 1996), although not all NLRG have polarized optical broad lines (in particular Cygnus A, Jackson and Tadhunter 1993, although Antonucci et al. 1994 suggested that this may be due to dilution by the local optical continuum at the scattering site).

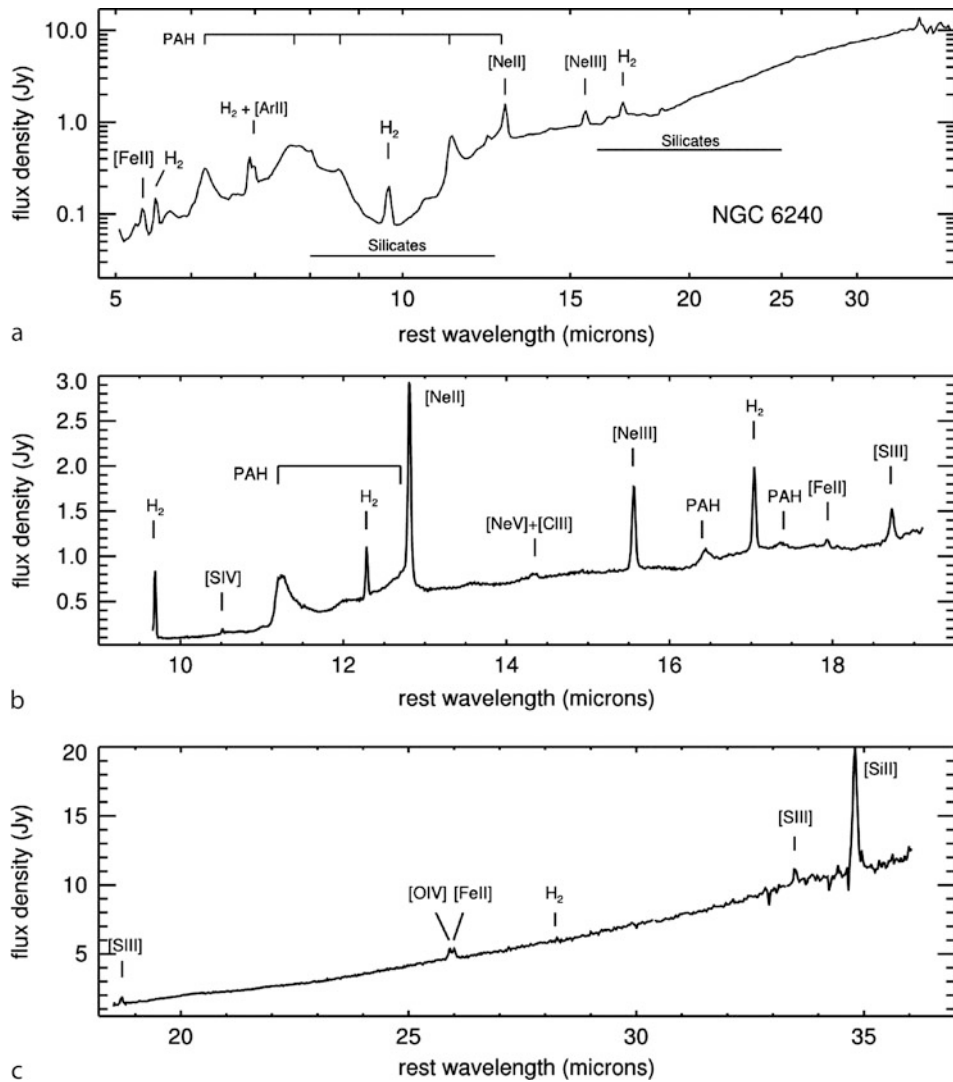


Fig. 7-20
Spitzer spectrum of the Seyfert 2 galaxy NGC 6240, revealing silicate absorption features as well as emission features from molecular gas. At top, the Short-Low spectrum is shown, while the middle and bottom panels show the Short-High and Long-Low spectra, respectively (From Armus et al. (2006, their Fig. 1))

3.3 Blazars, Jets, and Unified Schemes for Radio-Loud AGN

As has been seen, when an emitting plasma is moving at speeds close to that of light, relative to a fixed observer, a number of special relativistic effects are observed. Among these are superluminal motion as well as relativistic beaming. Therefore an important element in the

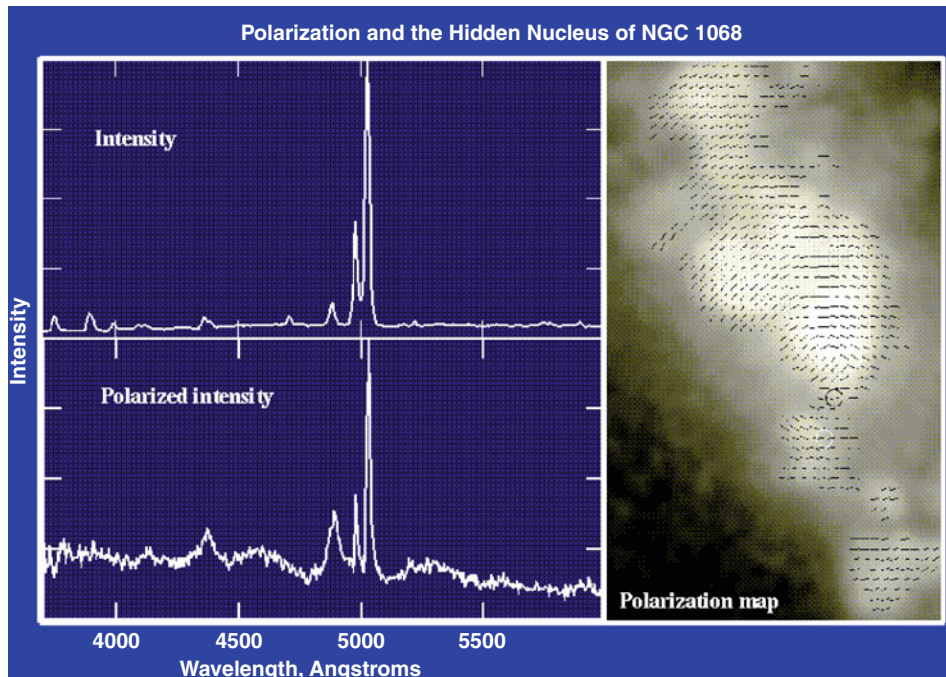


Fig. 7-21

Polarized broad-line and continuum emission from NGC 1068. As shown, broad H β emission is unambiguously seen in the polarized light spectrum but not in total intensity. The right-hand panel shows the polarization map from imaging polarimetry (Figure taken from W. Keel, using data from Antonucci and Miller)

verification of unified schemes is to see whether radio galaxies contain evidence of relativistic phenomena. This can be done in two ways: both by searching directly for those phenomena as well as by looking at the luminosity functions of both radio galaxies (known as the parent population under unified schemes) and blazars to see if the introduction of a simple relativistic beaming term can reproduce the features. In addition, since relativistic beaming is thought to explain the rapid variations and high polarizations observed in blazars and is also required to explain their GeV and TeV emission (Maraschi et al. 1992); these properties must also be present in unbeamed radio galaxies, albeit at lower levels.

Superluminal motion and violent variability have been observed in the radio galaxy M87, an FR 1 which is believed to be a misdirected BL Lacertae object (Tsvetanov et al. 1998; Harris et al. 2003). Figure 7-22 shows two important results from multiyear monitoring of M87 with the *HST*, *Chandra* and *VLA*. Several regions of the M87 jet show apparent superluminal motion, most prominently in HST-1, a knot located 60 pc (projected distance) from the core. As shown in Fig. 7-22 (left-hand panels), in this region four optical knots have been observed with apparent motions at speeds of $\sim 6c$ (Biretta et al. 1999). Somewhat slower speeds have been found in the radio for this region, as high as $4.3c$ (Cheung et al. 2007; Biretta et al. 1995), albeit not over the same 1994–1998 time period. Superluminal speeds have also been found in optical observations of several other regions of the M87 jet, out to about $10''$ (780 pc) from the nucleus,

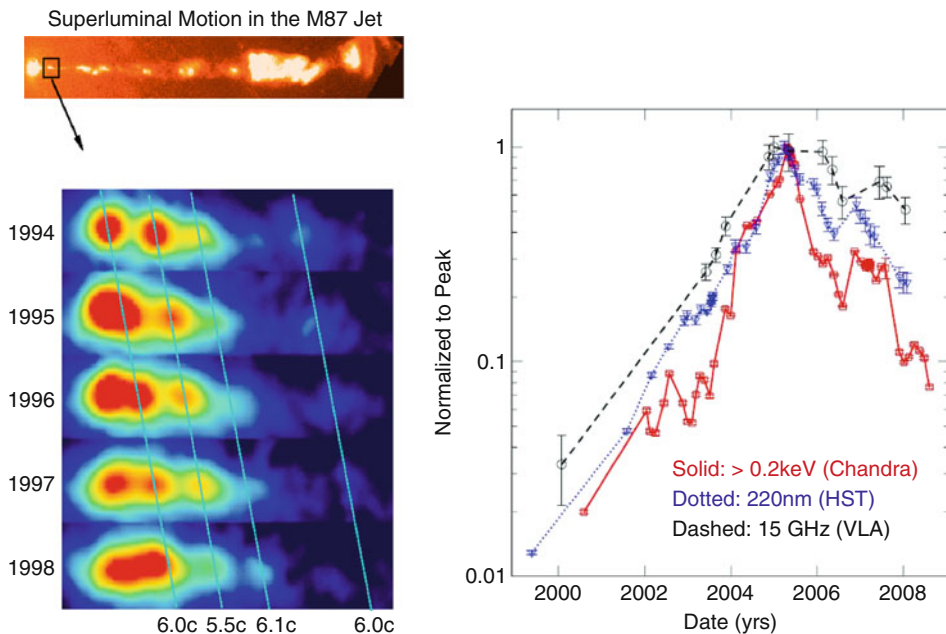


Fig. 7-22

Knot HST-1 in the M87 jet, located at a projected distance of 60 pc from the nucleus (see inset at top left), is the site of violent variability as well as superluminally moving components. The images at left, taken from Biretta et al. (1999, a color version of their Fig. 2), show the HST-1 region at five epochs, roughly once per year between 1994 and 1998. Four components are seen to move at speeds $\sim 6c$. As shown at right (taken from Harris et al. 2009, their Fig. 4), this region is also the site of violent variability; beginning in 2000, the knot began to increase in brightness, culminating in April 2005 when HST-1 had surpassed the core in flux by a factor of 2–6 in the UV and X-rays

with speeds that appear to decrease with distance from the nucleus, suggesting a gradual deceleration process may be at work. As of now no other radio galaxies have had such rapid motions detected, however a few other radio galaxies have been seen with mildly superluminal motions ($1\text{--}2c$), in particular B2 1144+35B (Giovannini et al. 2007, 1999).

Knot HST-1 is also the site of violent variability, another key property of blazars. As can be seen in Fig. 7-22 (right-hand panels), beginning in 2000–2001, HST-1 began a massive increase in its flux, which culminated in March–May 2005 when for 10 weeks the knot was two to six times brighter than the nucleus (depending on the band) in the ultraviolet and X-rays. At maximum, the flux of HST-1 had increased by about 100 over its quiescent level. It is not known whether other regions in the large-scale jet of M87 also vary in brightness; however, the nucleus of M87 is also known to vary rapidly, both in the optical (Tsvetanov et al. 1998; Perlman et al. 2011) as well as in the X-rays (Harris et al. 2009).

Significant core variability has been seen in other radio galaxies, particularly Centaurus A, which is known to vary massively in the hard X-ray and millimeter bands (Jourdain et al. 1993; Beckmann et al. 2007; Abraham et al. 2007; Chitnis et al. 2009), as well as 3C 390.3 and 3C 120, both of which are known to be variable in the optical and X-rays. In those last two objects,

there is, however, some controversy over the nature of the observed variability, as some of the properties are consistent with the less violent variability shown by Seyferts (both are broad-line objects; see Gliozzi et al. 2009 for 3C 390.3 and Marshall et al. 2009 for 3C 120), suggesting an origin outside the inner jet regions. However, both objects are known to exhibit apparent superluminal motion (see Gomez et al. 1998 for 3C 120, and Alef et al. 1988, 1996 for 3C 390.3), and in addition, Arshakian et al. (2010) and Abraham et al. (2007) argue strongly for the origin of the variability in 3C 390.3 in its jet. Radio variability is also seen for these objects as well as others in the radio (Ekers et al. 1983; Valtaoja et al. 1992), albeit in some cases mild enough that beaming may not be required for an explanation.

A well-known property of blazars is their high-energy gamma-ray emission – until recently, they were the only extragalactic objects known to emit at GeV and TeV energies, where in many cases it turns out that blazars emit the majority of their power (Fig. 7-23). Blazar gamma-ray emissions are highly variable, and it turns out that these variations put strong, model-independent constraints on the compactness required, requiring relativistic beaming in their own right. Specifically, in order for gamma-rays to escape the source, the optical depth to pair production, $\tau_{\gamma\gamma}$, must be of order unity or less, which is equivalent to saying the compactness, a convenient dimensionless parameter that represents source luminosity divided by dimension, must be less than about 40 at the threshold for pair-production. That is, $\tau_{\gamma\gamma} = l/40 = 1$, where $l = (L/r)(\sigma_T/m_e c^3)$ is the compactness, with L and r being the source luminosity and dimension. The Thomson cross section, σ_T , is appropriate because most pairs will be produced by interactions with gamma-rays rather than particles (see Sect. 7). For 3C279 and PKS 0528+134, the first two blazars where this variable emission was detected, the inferred values for the compactness are 5,000–15,000, well in excess of the optical depth limit. To allow gamma-rays to be observed from these blazars, the true gamma-ray luminosity must be much smaller than observed and the true size much larger. Relativistic beaming has the effect that $L_{\text{obs}} \sim \delta^{(3+\alpha)} L$, where δ is the Doppler beaming factor (7.7) and α is the spectral index. If r is estimated from the variability timescale, then

$$l = \delta^{-5} \frac{L_{\text{obs}}}{\Delta t_{\text{obs}}} \frac{\sigma_T}{m_e c^4} \quad (7.7)$$

The limit $l \leq 40$ then translates to $\delta \geq 6$ for 3C 279 and $\delta \geq 7$ for PKS 0528+134, where L_{obs} has been evaluated at X-ray energies under reasonable spectral assumptions (Maraschi et al. 1992); similar limits are obtained for other gamma-ray blazars (Dondi and Ghisellini 1995). More recent observations (Abdo et al. 2009a) show much shorter timescale variability now in GeV observations, as small as days, and in TeV observations on timescales of less than an hour (Benbow et al. 2008). As shown in Fig. 7-23, M87 (Abdo et al. 2009b; Aharonian et al. 2006; Beilicke et al. 2005) is now known to emit in both GeV and TeV gamma-rays, with a luminosity much less than that seen in blazars, and is in addition, strongly variable on timescales as small as a day, while Centaurus A and NGC 1275 (Abdo et al. 2009c) are now confirmed as GeV emitters, with luminosity similarly orders of magnitude below that seen in blazars. Thus the detection of very-high-energy gamma-ray emission also argues for relativistic jets in both blazars and radio galaxies, and hence unification.

A final piece of evidence in favor of the unification of radio-loud classes of AGN can be found in their luminosity functions. Specifically, Urry and Padovani (1995) found that they could use a fit to the luminosity function of the 2 Jy radio galaxy sample and apply a simple beaming correction, and derive a reasonable fit to the luminosity function of both quasar-type and BL Lac-type blazars. That work requires Doppler factors for both populations of

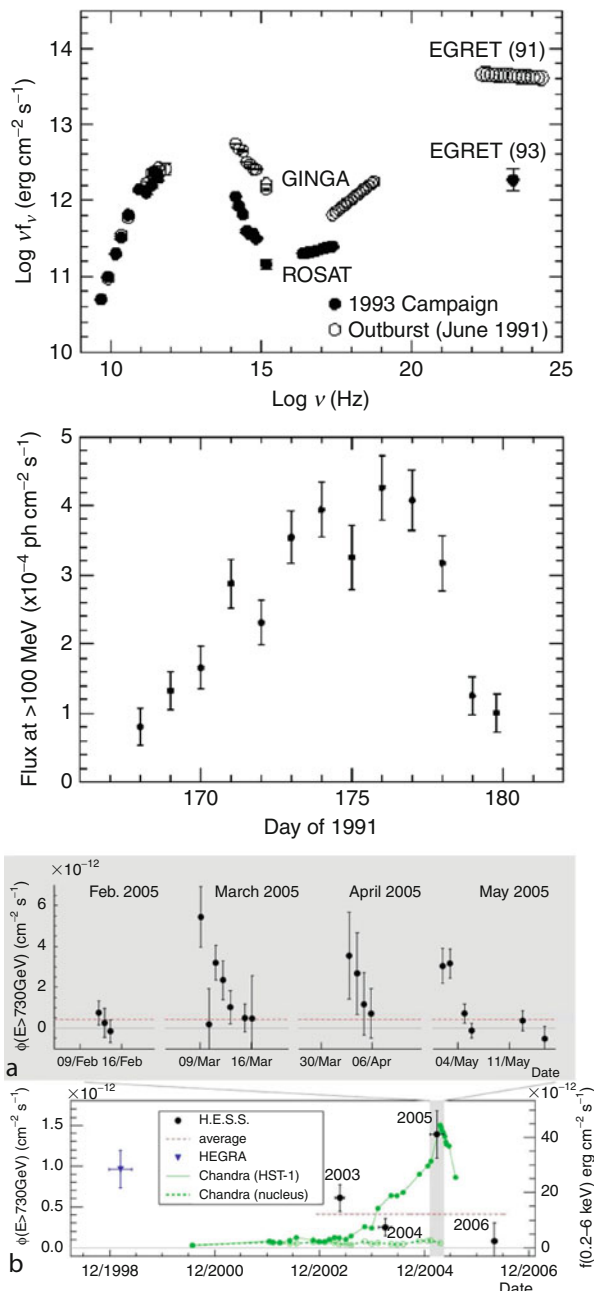


Fig. 7-23

At top, the spectral energy distribution for the blazar 3C 279 during 1991 and 1993, and at middle, the GeV variability seen by EGRET during the 1991 flare. At bottom, the fast variability now seen for M87 in the TeV band. Figures from Maraschi et al. (1994a), Kniffen et al. (1993), and Aharonian et al. (2006). The similarity between these variations is striking and in both cases requires relativistic beaming

between 2 and 40, with a power-law distribution, and critical viewing angles of 10–20°. More recent work (Padovani et al. 2007) has verified and strengthened this connection.

4 Nuclear Black Holes and Accretion

The development of the dominant paradigm for AGN occurred gradually. Of key importance was the realization that a black hole was necessary to drive the enormous luminosities and high-energy phenomena seen in AGN. The generation of large luminosities (as high as 10^{12-14} solar luminosities in quasars) in a region only a few light-days across is quite difficult. A stellar cluster, for example, would have to include many billions of stars in this small volume in order to explain these luminosities, and it is a simple matter to calculate that such a cluster would be unstable to collapse within very short timescales. It is for this reason that Donald Lynden-Bell (1969) first suggested the connection between active galaxies and black holes.

Accretion onto a black hole can be highly efficient in producing energy. If one assumes a small mass δm spiraling into a black hole from infinity, it will have an available (gravitational potential) energy of $\delta E = \frac{GM_{\text{BH}}\delta m}{r}$, such that the upper limit on the luminosity is simply $L_{\text{max}} = \frac{GM_{\text{BH}}\dot{M}}{r}$. Note that this is an upper limit – not all of the gravitational potential energy can be extracted from infalling matter. If, however, one assumes that the matter goes in to $3 R_S$ (the location of the innermost stable orbit for a Schwarzschild black hole), then the efficiency ε is

$$\varepsilon \equiv \frac{L}{\dot{M}c^2} = \frac{GM_{\text{BH}}\dot{M}}{(6GM_{\text{BH}}/c^2)} \times \frac{1}{\dot{M}c^2} \approx 0.17 \quad (7.8)$$

A considerably higher efficiency can be reached if the matter goes all the way to the event horizon before plunging (as it would in a maximally rotating Kerr black hole). However, a countervailing factor is that this calculation is purely Newtonian and does not take into account relativistic effects, nor does it take into account exactly how the energy is extracted or any fluid-dynamical effects within the accretion disk (about which more later). Taking these into account, the best estimate for ε is ~ 0.06 for the Schwarzschild case and 0.42 for the Kerr case. So, for example, if $\varepsilon \sim 0.1$, then a luminosity of $10^{46} \text{ erg s}^{-1}$ requires an accretion rate $\dot{M} = 2M_{\odot} \text{ year}^{-1}$.

Another constraint on the energy that can be extracted from accretion onto a black hole comes from radiation pressure. A basic result from electromagnetism is that radiation exerts a momentum flux of $P_{\text{rad}} = L/(4\pi r^2 c)$, and so there will be a force $F_{\text{rad}} = \frac{L\sigma_T}{4\pi r^2 c}$ on each electron at a distance r , where σ_T is the Thomson cross section. So, if the radiative force equals that from gravity, the luminosity is

$$L_{\text{Edd}} = \frac{4\pi G cm_p}{\sigma_T} M_{\text{BH}} = 1.51 \times 10^{38} \left(\frac{M}{M_{\odot}} \right) \text{ erg s}^{-1}. \quad (7.9)$$

This result, known as the *Eddington limit*, is a result that is also important to X-ray binary systems as well as high mass stars. If the luminosity exceeds this quantity, radiation force must overpower gravity. It represents a fundamental limit to the luminosity of any accretion-powered source, as without matter streaming in, the accretion process cannot function (although, *n.b.*, there are a few objects where asymmetric, super-Eddington flows are suspected (Collin et al. 2006; Collin and Kawaguchi 2004)). This argument can also be inverted – that is, the large luminosities observed from AGN absolutely demand central black holes in the range 10^5 – $10^9 M_{\odot}$, as if the central object were either less massive or not a black hole, the Eddington limit would

be violated. In fact, if a black hole's accretion flow produces light with a fixed efficiency ϵ , its mass also sets a characteristic scale for the mass accretion rate – the Eddington rate:

$$\dot{M}_{\text{Edd}} = \frac{L_E}{c^2 \epsilon} = 3 \left(\frac{M_{\text{BH}}}{10^8 M_\odot} \right) \left(\frac{\epsilon}{0.1} \right)^{-1} M_\odot \text{ year}^{-1}, \quad (7.10)$$

An important – if obvious – point needs to be made here and that is that in order to reach high efficiencies ϵ , the matter cannot just quickly accrete into the black hole. If matter plunges into the black hole quickly and as discrete lumps (e.g., stars or planets), there is little prospect for extracting significant amounts of radiative energy from it. Thus, two critical parts of the equation are the time taken in the accretion process and whether accreted objects are disrupted into smaller bits as they stream in. The latter question is governed by tidal forces, and for a rough indicator of where these forces operate, one can turn to the Roche criterion, which expresses the competition between the smoothed out mass density of the central black hole and the gravitational forces (i.e., internal mean density) of the star or planet. For a self-gravitating object of mass M_* and radius R_* , this will mean that the object will be pulled apart by tidal forces when it approaches closer than the tidal radius,

$$r_t = R_* \left(\frac{M_{\text{BH}}}{M_*} \right)^{1/3} \approx \left[\left(\frac{M_{\text{BH}}}{10^8 M_\odot} \right)^{-2/3} \left(\frac{\rho_*}{\rho_\odot} \right)^{-1/3} \right] R_S, \quad (7.11)$$

where the latter scaling holds for an object at the solar density. For a solar-type star, this radius is *smaller* than the Schwarzschild radius when the black hole's mass is less than $10^8 M_\odot$ – so that it is entirely conceivable that a star could accrete onto the black hole without being disrupted first. Thus, even though this radius varies weakly with the density of the object being accreted, it is important to realize that gravity alone will not serve to extract significant amounts of energy from matter. Therefore it is more profitable to consider the supply of matter at lower densities, that is from the interstellar medium. Furthermore, one also needs to consider the roles played by other processes – such as viscosity and disk structure – in the energy production mechanism. The actual efficiency of the process and hence the luminosity of any accreting black hole system are highly dependent on the type of accretion flow – disk, spherical, or otherwise – as well as whether the cooling within the disk is dominated by radiative or dissipative losses.

The data are decisively in favor of the association of AGN with nuclear black holes. A few AGN were included in the HST Nuker survey of nearby galaxies (Magorrian et al. 1998) for central black holes, in particular M87, where the data require a $3 \times 10^9 M_\odot$ black hole. This link has been strengthened by gas dynamical measurements of black hole masses for a number of other AGN (Wang et al. 2009; Onken and Kollmeier 2008; Zhang et al. 2008; Vestergaard et al. 2008; McGill et al. 2008; Hicks and Malkan 2008; Onken et al. 2007; Greene and Ho 2007; Kelly and Bechtold 2007). Moreover, reverberation mapping (Sect. 5.1) has now been used to estimate the black hole masses for dozens of AGN (Vestergaard and Peterson 2006; Vestergaard and Osmer 2009; Bentz et al. 2009c) and work back to the $M-\sigma$ relation (Ferrarese and Merritt 2000), which is found to be the same for AGN as it is for normal galaxies. Finally, maser molecular line features have been discovered in several Seyfert 2s. The data indicate that the material comes from warped, rotating disks a few thousand R_S from the black hole (e.g., Fig. 7-24). The advantage of this last method is that it is sensitive to only the accretion structure itself, as the resolution of the VLBI technique is a 100 times finer than that available from HST optical data.

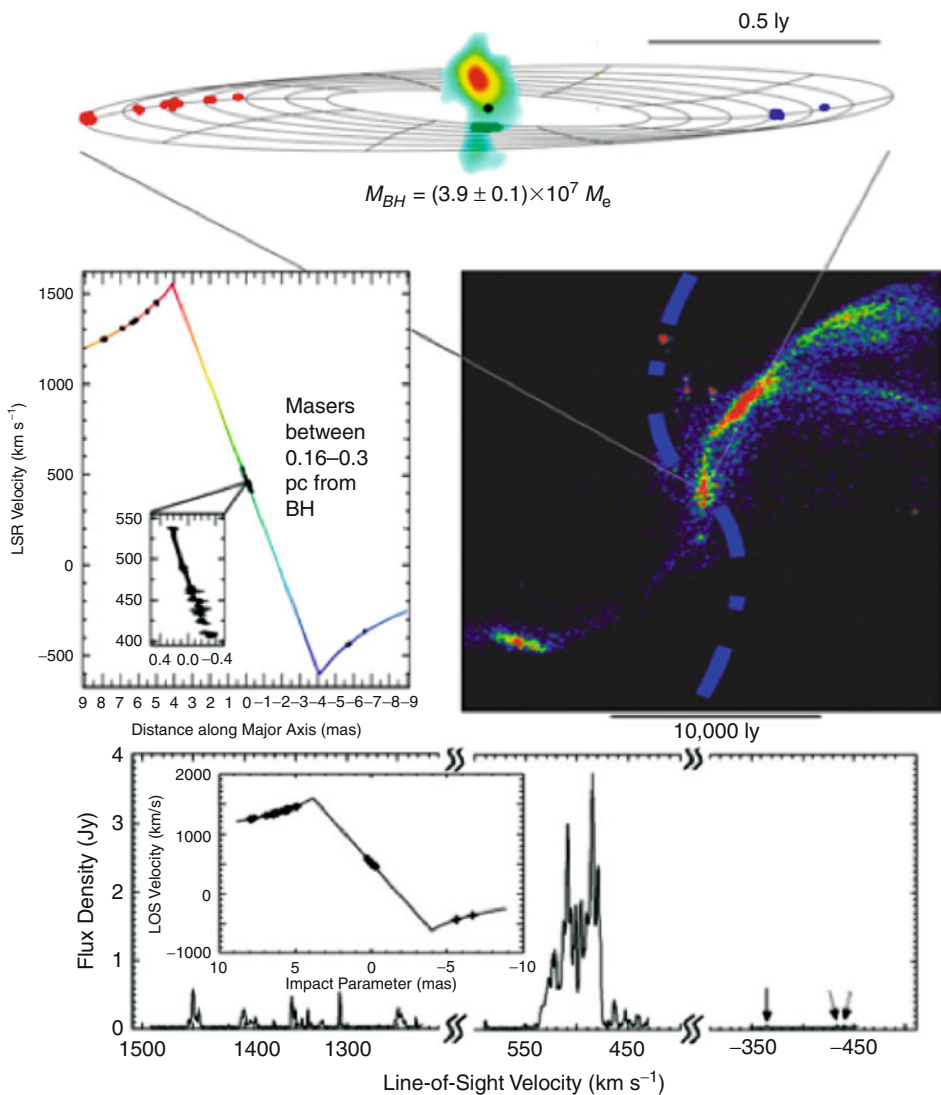


Fig. 7-24

Masing molecular features discovered in the outer accretion structure of NGC 1068. Included is a model fit for a Keplerian disk with a central *black hole* of the indicated mass (Figure taken from Greenhill et al. (1996))

None of these datasets, however, can tell us what kind of a black hole is present. The jury is still out on this; however, the latest data indicate that at least some AGN require near maximally rotating Kerr black holes. The reason for this is twofold. First of all, broadened Fe K α lines have been observed in several AGN (e.g., Fig. 7-25), which not only require both special and general relativistic corrections to explain their profiles, but also require that material be present within $3 R_S$, where the innermost stable orbit would lie for a nonrotating Schwarzschild

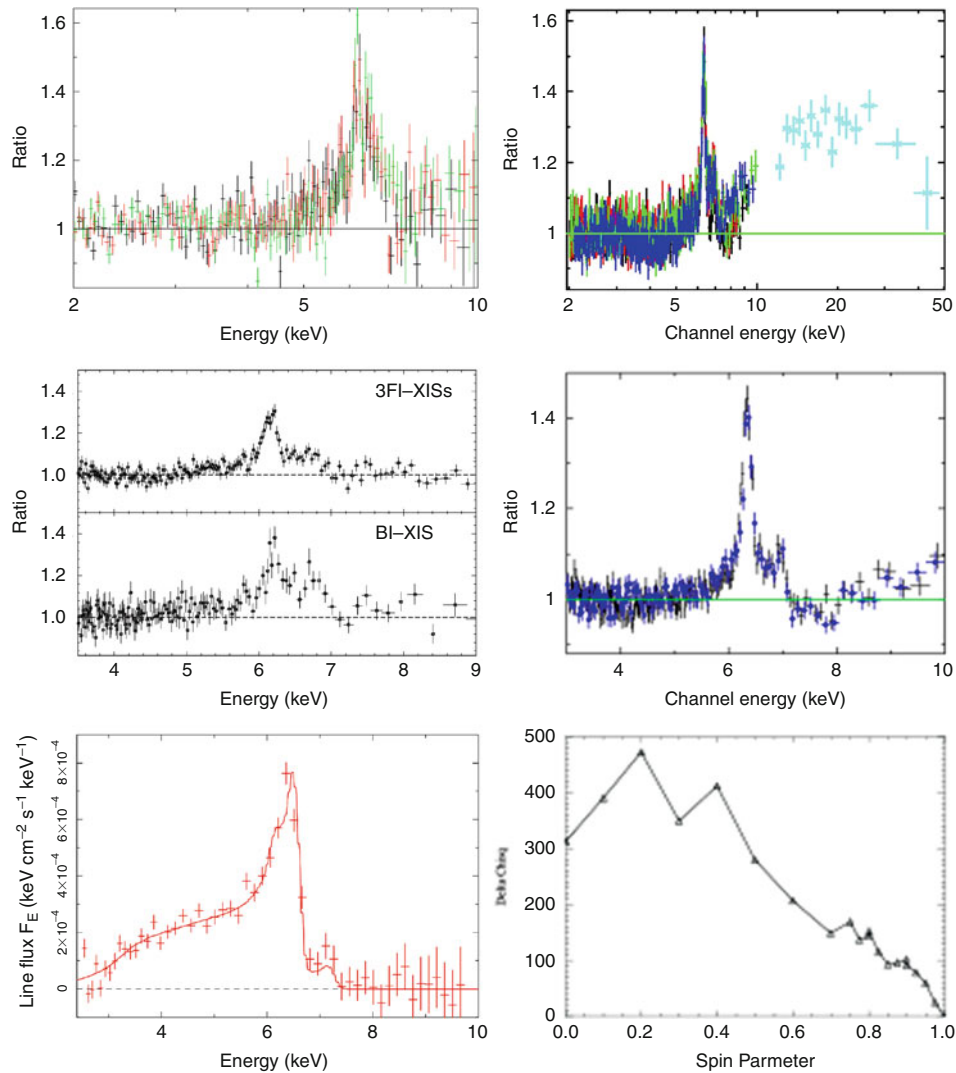


Fig. 7-25

X-ray spectra of four active galaxies showing the Fe K α line profiles seen for objects best fitted by disks that truncate at $40 R_G$ (Mrk 335, top left, Larsson et al. 2007), $20 R_G$ (MCG -5-23-16, top right and middle right, Reeves et al. 2007), $10 R_G$ (3C 120, middle left, Kataoka et al. 2007), and $< 3 R_G$ (MCG -6-30-15, bottom panels, Fabian et al. 2002). This type of line profile can only be produced by the warped spacetime that exists close to the event horizon of a *central black hole*.

black hole. The presence of cold material at smaller radii requires a rotating black hole, where the innermost stable orbit can move closer in to the ergosphere. If the black hole were not rotating, all of the material within $3 R_S$ would be in the “plunging region” where no stable orbit is possible, and in that case it would plunge into the black hole in a very short time with no further release of energy.

The second reason why rotating black holes may be required for many AGN comes from models of jet ejection (e.g., Meier et al. 2001; Tchekhovskoy et al. 2011; see  Sect. 7), which indicate that the acceleration of a highly relativistic jet is much easier in the ergosphere surrounding a maximally spinning black hole. This latter work is not yet backed up by data, although some authors (notably Sikora et al. 2007) have linked the radio-loud/radio-quiet dichotomy to the spin of the central black hole.

4.1 Bondi Accretion

The simplest type of flow one can imagine into the central black hole is purely spherical. This is the classic problem of *Bondi accretion*. Imagine a black hole moving through a uniform medium of density ρ_∞ at some (relatively slow) velocity v . In spherical symmetry, the accretion rate from a radius r will then be simply $\dot{M} = 4\pi r^2 \rho_\infty v$. If the gas is adiabatic, then from a fluid-mechanical analysis of the surrounding medium, one can derive (see, e.g., Krolik 1999) that the overall accretion rate will be

$$\dot{M} = 4\pi\lambda(\gamma) \frac{(GM)^2}{c_s^3} \rho_\infty, \quad (7.12)$$

where c_s is the speed of sound and λ is a dimensionless parameter dependent only on the adiabatic exponent γ :

$$\lambda(\gamma) = \left(\frac{1}{2}\right)^{(\gamma+1)/[2(\gamma+1)]} \left(\frac{5-3\gamma}{4}\right)^{-(5-3\gamma)/[2(\gamma-1)]}. \quad (7.13)$$

This analysis then allows one to estimate the gas density necessary to feed an AGN of a given luminosity and mass:

$$\rho_\infty = 5 \times 10^{27} \left(\frac{L}{10^{45} \text{erg s}^{-1}}\right) \left(\frac{T}{10^4 \text{K}}\right)^{3/2} \left(\frac{\varepsilon}{0.1}\right)^{-1} \left(\frac{M_{\text{BH}}}{10^8 M_\odot}\right) \text{g cm}^{-3}. \quad (7.14)$$

Bondi accretion represents the simplest solution to the problem of accretion in the sense that no assumption is made regarding the density of the material, incoming angular momentum, or the like. Of course more complex solutions, particularly disks (discussed next), are possible if the matter comes in with significant angular momentum.

As matter that is accreting spherically does not spend a large amount of time falling into the black hole, the majority of the regions around the black hole are optically thin, so that any emission is Bremsstrahlung, which has an emissivity proportional to $T^{-1/2} n^2$. An adiabatic accretion flow will then have a luminosity

$$L = \int_{R_s}^{r_{\text{acc}}} 4\pi r^{1/2} \frac{AT_\infty^{1/2}}{\rho_\infty m_p^2} \left(\frac{\dot{M}}{4\pi}\right)^{7/3} \left(\frac{1}{2GM}\right)^{7/6} dr. \quad (7.15)$$

$$= \frac{8\pi A}{m_p} \left(\frac{T_\infty^{3/2}}{\rho_\infty}\right)^{1/3} \left(\frac{\dot{M}}{4\pi}\right)^{7/3} \left(\frac{1}{2GM}\right)^{7/6} \left(\frac{1}{R_s^{1/2}}\right). \quad (7.16)$$

After some manipulation, this simplifies to

$$L = \frac{8Ac}{4^{8/3} \pi m_p^{3/2} G \sqrt{2k}} \left(\frac{\dot{M}^2}{M_{\text{BH}}}\right). \quad (7.17)$$

For typical temperatures and densities, this emission is seen in the X-rays. The efficiency is then

$$\epsilon = \frac{8A}{4^{8/3}\pi m_p^{3/2} G c \sqrt{2k}} \left(\frac{\dot{M}}{M_{\text{BH}}} \right). \quad (7.18)$$

By putting in values typical of galactic nuclei, one sees that this is generally a very inefficient process. For example, Bondi accretion for Sgr A* gives an efficiency $\epsilon = 10^{-7}$, whereas most AGN require much higher efficiencies. As a result, Bondi accretion is probably important only for low-luminosity AGN, particularly LINERs and possibly also FR I radio galaxies (Allen et al. 2006). For more luminous objects, a different solution must be sought.

Thus spherical accretion, while likely common in galactic nuclei, actually has limited utility for fueling activity. In general, it is very inefficient in translating gravitational potential energy into radiative energy due primarily to the fact that the density of incoming material tends to be low and a given parcel will accrete onto the black hole relatively quickly (as opposed to disk accretion, for which see the next section).

4.2 Disk Accretion

One of the problems with spherical accretion is that the matter can fall into the black hole in a relatively short time, thus allowing little opportunity for the extraction of energy into radiative form. Also, it takes no account of the angular momentum of the matter streaming in. This latter consideration is important. If, for example, the central regions of the host galaxy are rotating, or if matter is streaming in to the central regions from a galactic interaction, then it will enter the central regions with considerable angular momentum, which must be dealt with if matter is to accrete onto the central black hole. In a typical galaxy, matter orbiting the nucleus at distances of kiloparsecs has a typical specific angular momentum of $10^{28} - 10^{29} \text{ cm}^2 \text{ s}^{-1}$, while matter orbiting at the last stable orbit of a $10^8 M_\odot$ black hole has a specific angular momentum four orders of magnitude less. Thus if rotation or large-scale streaming motions are important in a galaxy, it will be necessary for any matter that accretes to shed its angular momentum before being accreted onto the central black hole to fuel activity.

It is well known that typical galaxies are rotationally flattened into disk shapes by their angular momenta. It should therefore not be surprising that the same thing happens to accreting matter. Thus when angular momentum is important, one would expect material orbiting the black hole to stream into a disk, where as it loses energy and angular momentum (by heretofore unspecified processes) it will fall into a succession of ever-so-slightly smaller circles until finally it reaches the last stable orbit and plunging region. It should be mentioned that matter in this case will take a considerably longer period of time to make the journey from the nuclear interstellar medium into the black hole. This allows much more time for the extraction of energy, which was one of the problems plaguing Bondi accretion. Thus disk accretion can be much more efficient at extracting energy from accreting matter than Bondi accretion.

It is a good idea to begin our consideration of accretion disks with a discussion of their structure in terms of both temperature and density. If one assumes that the disk is supported against gravity by a pressure gradient in the vertical coordinate z , then from hydrostatic equilibrium,

$$\frac{dP}{dz} \cong -\rho \frac{GM}{R^3} z \quad (z \ll R). \quad (7.19)$$

For an isothermal thin disk, the solution is an exponential

$$\rho = \rho(z=0) \exp\left(-\frac{\Omega^2 z^2}{2c_s^2}\right) = \rho(z=0) \exp(-z^2/h^2). \quad (7.20)$$

where the scale height is

$$h = \frac{\sqrt{2}cs}{\Omega} = \frac{\sqrt{2}csR}{v_\phi},$$

Ω is the angular velocity, and the velocity v_ϕ is just the Keplerian orbital speed for a given radius. This means that the specific angular momentum at any radius R will be $l = \sqrt{GM_{\text{BH}}R}$. To flow inward, the gas must lose angular momentum through some unknown process. This can include redistribution of some kind (i.e., by gas at the smallest radii losing angular momentum) or a generalized wind or outflow. In either case, matter will be transported to small radii while angular momentum is carried out to a very large radius by some tiny fraction of the mass that must therefore leave the black hole's environs at large speeds.

If the gas is flowing inward, it will have a potential energy per unit mass of

$$E = -\frac{GM_{\text{BH}}}{R}. \quad (7.21)$$

So for a small parcel of mass dM flowing inward by dR (see geometry in Fig. 7-26), its potential energy will change by

$$dE = \frac{GM_{\text{BH}}}{R^2} dMdR. \quad (7.22)$$

Half of the energy will go into increasing the kinetic energy of the gas, while the other half is radiated. Therefore the luminosity at each radius will be

$$L = -\frac{GM_{\text{BH}}\dot{M}}{2R^2} dR. \quad (7.23)$$

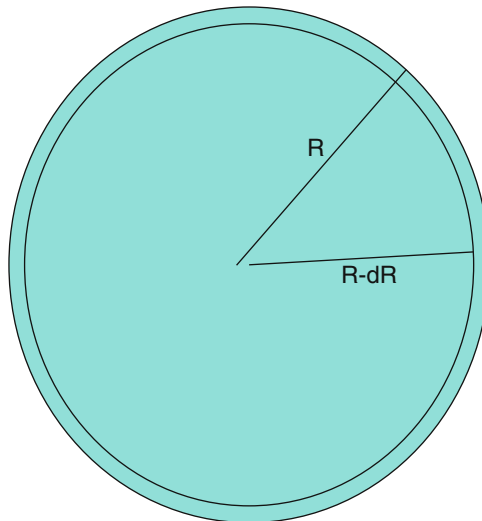


Fig. 7-26
Geometry for disk accretion

By dividing by the radiating area and equating the rate of energy loss assuming blackbody radiation, one can derive a radial temperature distribution for the disk:

$$T = \left(\frac{GM_{\text{BH}}\dot{M}}{8\pi\sigma R^3} \right)^{1/4} = 6.8 \times 10^5 \epsilon^{-1/4} \left(\frac{L}{L_E} \right)^{1/2} \left(\frac{L}{10^{46} \text{erg s}^{-1}} \right)^{-1/4} \left(\frac{R}{R_G} \right)^{-3/4} \text{K.} \quad (7.24)$$

It should be noted that this analysis, due to Shakura and Sunyaev (1973), does not account for the transport of angular momentum or boundary conditions (including general relativistic corrections near the black hole), and of course it assumes local thermodynamic equilibrium. A more correct analysis that includes these factors as well as the disk viscosity (see below) (Melia 2009) obtains

$$T = \left(\frac{3GM_{\text{BH}}\dot{M}}{8\pi\sigma R^3} \left[1 - \sqrt{\frac{R_{\text{in}}}{R}} \right] \right)^{1/4}. \quad (7.25)$$

The overall disk spectrum will then be an integral over the entire range of radii for which the disk exists, weighted by the mass in each annulus. The majority of the disk emission will come from the innermost region of the disk (i.e., the innermost few gravitational radii); however, as the accretion disk is expected to span at least two to three decades in radius, a similar range in temperature and hence frequency is to be expected from the disk spectrum. Theoretical models of disks indicate that the spectrum one should expect (e.g., Koratkar and Blaes 1999) is relatively flat, $\nu^{-1/3}$, over the range of temperatures seen in the disk, with an exponential cutoff at high frequencies. As shown by Fig. 7-27, this is consistent with the broad spectral energy distribution seen from most AGN in the near-IR, optical, and ultraviolet.

The exact mechanism for redistributing angular momentum is not clear. While it is clear this is a viscous process, it cannot simply be the microscopic viscosity, which is far too weak to have a noticeable effect. One way to produce a larger viscosity is via turbulence; however, there is no obvious reason why one might expect a turbulent disk as the Rayleigh stability criterion is satisfied for the Keplerian potential. It is true that since the interesting regions of AGN disks have temperatures $\sim 10^5$ K, He II/He III ionization transitions may occur at some radii, which would then be convectively unstable. However, such a mechanism is unlikely to exist throughout the disk, and, moreover, simulations appear to show that convection tends to carry angular momentum *in* rather than *out* (Stone and Balbus 1996). The conventional view now appears to be that magnetic fields are required to transport angular momentum outward, as required. In the presence of a magnetic field, the instability criterion is satisfied because the magnetic field couples fluid elements together. This mechanism, known as the magnetorotational instability (MRI) (e.g., Balbus 2003), can transport angular momentum outward. If the magnetic field grows as one goes to smaller radii, the MRI becomes stronger, and therefore one can see that this process is also intimately tied up with the mechanism for producing large-scale outflows and jets (about which more later), which also are likely responsible for carrying outward a fair fraction of the angular momentum of disk matter.

4.3 Disk Coronae and the 6.4 keV Iron Line

Accretion disks produce a quasi-thermal spectrum that tends to peak in the ultraviolet to soft X-rays. However, as already indicated, AGN usually exhibit emission that extends to much higher energies, ≥ 100 keV even for radio-quiet AGN. This emission cannot come from the disk

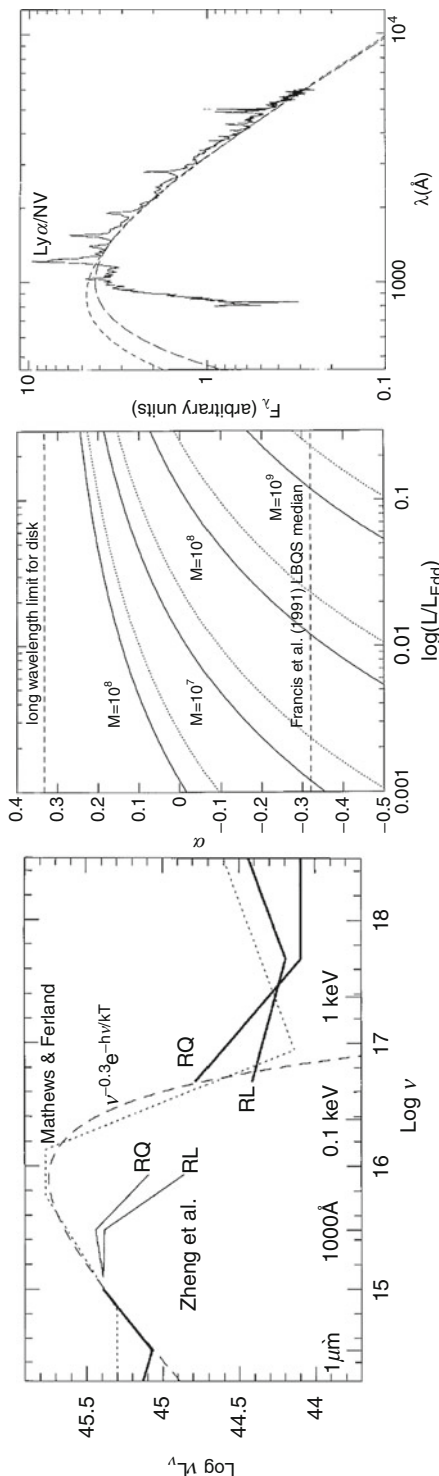


Fig. 7-27

Predictions and performance for accretion disk models. At left, and middle, the optical/UV slopes predicted by simple models of disk accretion around Schwarzschild black holes, as a function of luminosity. The transfer function used is fully relativistic, and the upper and lower curves correspond to inclination angles of 66° and 26° , respectively. At right, a fit of a model accretion disk spectrum to the composite quasar spectrum of Francis (1996). Note the excellent fit, although the roll-off has yet to be replicated by data due to the difficulty of observations (All plots from Koratkar and Blaes (1999, their Figs. 7-3, 7-16 and 7-17)

itself or the broad- or narrow-line regions because the conditions are not right. However, one aspect not yet considered is whether, in a system where disk accretion is going on, the regions surrounding the accretion disk will contribute to the emissions observed. It is logical to assume that, at higher latitudes surrounding the accretion disk, there is an “atmosphere” or (as more often attributed) corona of hot gas. This corona can be much less dense than the accretion disk itself; however, thanks to well-known processes such as Compton scattering, it can account for a major portion of the AGN emission.

In Compton scattering, photons are scattered by electrons. It is important to point out that Compton scattering is a *mandatory* process – that is, if one has a region of space with a considerable population of free electrons, and a bright radiation source nearby, the process is unavoidable. These conditions are easy to satisfy in a lower-density region near the center of an AGN, and therefore it is critical to consider Comptonization and its implications for AGN – both in the corona as well as other regions (see [Sect. 7](#) on jets, below). In this section, the theory of Comptonization and its impact on AGN are discussed. More information on the subject is available from, for example, Rybicki and Lightman (1986).

It is a well-known result from special relativity that when a photon is scattered by an electron, its wavelength changes by

$$\Delta\lambda = \frac{h}{m_e c} (1 - \cos \theta), \quad (7.26)$$

and its final energy is related to its initial energy via

$$\Delta E = \frac{E^2}{m_e c^2} (1 - \cos \theta). \quad (7.27)$$

In the electron’s rest frame, the photon imparts energy to the recoiling electron. However, in the laboratory frame, it is possible for the electron to impart energy to the photon, up to $\Delta E = (\gamma - 1) m_e c^2$ (where γ is the electron’s Lorentz factor) if the angle is right. This process, whereby the photon gains energy through scattering, is called inverse-Compton scattering. For low-energy electrons, this process is not important; it is only for high-energy particles (i.e., hot gas) where it takes on critical importance.

It can be shown that for a nonrelativistic, thermal distribution of electrons with temperature T_e , the average change in energy becomes

$$\langle \Delta E \rangle = (4kT_e - E) \frac{E}{m_e c^2}. \quad (7.28)$$

For a thermal distribution of electrons, a photon will gain energy if its energy $E \ll 4kT_e$, with the change in energy being proportional to γ^2 . One factor of γ in this proportionality comes from the boosting of the photon into the electron’s initial rest frame, while the other comes from the boosting of the scattered photon back into the lab frame. The process of inverse-Compton scattering can occur an arbitrary number of times (so long as the photon remains within the scattering region), as long as $E \ll 4kT_e$, with $\Delta E/E = 4kT_e/m_e c^2$. After N scattering events, the photon’s final energy will be given by

$$E_f = E_i \exp \left(N \frac{4kT_e}{m_e c^2} \right) \quad (7.29)$$

Typically the number of scatters is parameterized in terms of the optical depth τ_{es} ; in this parameterization, the average number of scatters will be $\max(\tau_{es}, \tau_{es}^2)$. Often one speaks in terms of

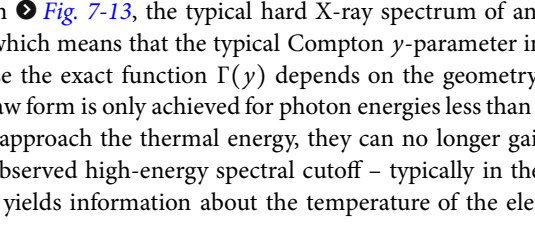
the Compton y -parameter, where y is defined such that

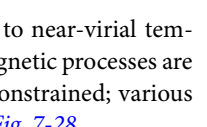
$$y = \max(\tau_{\text{es}}, \tau_{\text{es}}^2) (4kT_e/m_ec^2) \quad (7.30)$$

and $E_f = E_i e^y$. If y is large – a case known as saturated Compton scattering – the average photon will reach the thermal energy of the electrons. This process is less important for accreting black hole systems. More important for AGN coronae is the unsaturated case, which is the suspected mechanism for producing the hard X-ray continuum in the broadband spectrum of AGN. In the context of accreting black hole systems, it is most convenient for the corona to speak of the *virial temperature* that refers to the average accretion energy per particle. Since the gravitational energy released per particle of mass m scales as $GM_{\text{BH}}m/r$, which itself scales as $mc^2/[R/(GM_{\text{BH}}/c^2)]$, the virial temperature is independent of the size of the black hole. Electron virial temperatures of tens to hundreds of keV can be readily achieved in the innermost regions of black hole systems (the proton virial temperature is a factor $\sim 2,000$ higher), and this represents the maximum energy that Comptonized photons can achieve.

The resulting spectrum thus reflects the competition between the number of scatterings and the likelihood of these multiple scatters – although multiple scatterings become exponentially unlikely, they produce exponential energy gain. The two effects balance to some degree, and it can be shown that for a given Compton y -parameter, the resulting spectrum is a power law with photon index $\Gamma(N(y) \propto E^{-\Gamma})$ of approximately 1 (see Reynolds and Nowak 2003).

$$\Gamma = -\frac{1}{2} + \sqrt{\frac{9}{4} + \frac{4}{y}}. \quad (7.31)$$

As can be seen from , the typical hard X-ray spectrum of an AGN has a photon index of around 2, which means that the typical Compton y -parameter in black hole coronae is about 1. Of course the exact function $\Gamma(y)$ depends on the geometry and other assumptions, and a power-law form is only achieved for photon energies less than the electron thermal energy. As photons approach the thermal energy, they can no longer gain energy from scattering, so that the observed high-energy spectral cutoff – typically in the neighborhood of a few hundred keV – yields information about the temperature of the electrons in the AGN's corona.

It should be mentioned that the mechanism for heating the electrons to near-virial temperatures is currently unknown, although the leading hypothesis is that magnetic processes are dominant. Second, the geometry of the corona in AGN is completely unconstrained; various workers have produced models for a variety of geometries, as shown in .

A second set of processes, due to reprocessing in the accretion disk's outer layers of photons scattered within the corona and then “reflected” back toward the disk, are also important for AGN X-ray spectra. These processes may be modeled simplistically by supposing that the accretion disk is a semi-infinite slab of uniform density gas, irradiated from above by a continuum produced in the corona via thermal Comptonization. Hydrogen and helium are assumed to be fully ionized, but heavier elements are neutral. While a crude approximation, this is not far from the truth in a relatively “cold” accretion disk.

An X-ray photon coming from the corona can either be scattered by the free electrons associated with the ionized hydrogen and helium, or the outer electrons of the other elements, or photoelectrically absorbed by one of the neutral atoms. For the latter process to occur, the photon's energy must be above the threshold energy for a given photoelectric transition. The transitions with the largest cross sections are those associated with the ejection of K -shell

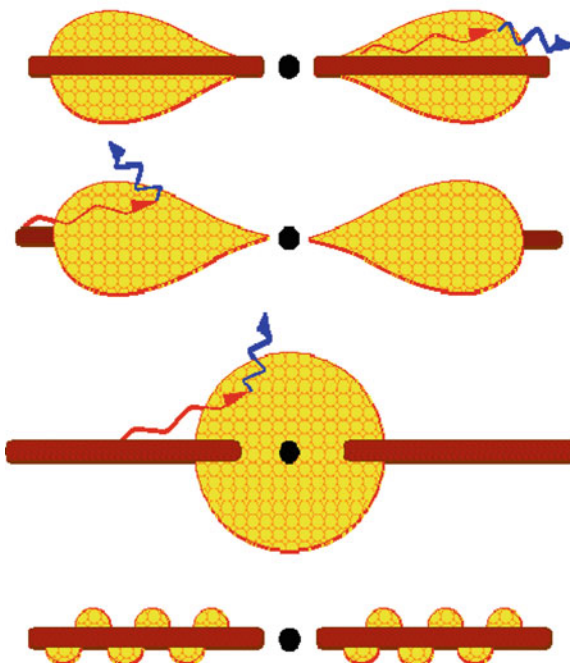


Fig. 7-28

Possible geometries for accretion disk-corona systems. The *top panel* is referred to as a “slab” or “sandwich,” but it predicts spectra softer than observed. The remaining three geometries give a corona that is less effectively cooled by soft disk photons. The *middle two* are referred to as “sphere + disk” geometries, whereas the *bottom geometry* is called a patchy corona. (Figure taken from Reynolds (1996))

(i.e., $n = 1$) electron. Following K -shell photoionization, the resulting ion usually de-excites in one of two ways, both of which start with an L -shell ($n = 2$) electron dropping into the K -shell. This can occur with either the excess energy being radiated as a $K\alpha$ line photon or a second L -shell electron can be ejected (often called autoionization or the Auger effect). Thus the output spectrum must include both of these effects: a “hump” due to the reflection at 30–40 keV and then a variety of $K\alpha$ lines from different elements (see [Fig. 7-29](#)).

These features are indeed observed in most spectra, as shown by the recent Suzaku spectrum of MCG-6-30-15 (Reynolds and Miller 2009), as well as Chandra and XMM observations of several other AGN (Brenneman and Reynolds 2009). Importantly, one expects that the disk, and the associated corona, will truncate at a similar radius, namely, that of the innermost stable orbit (Reynolds and Miller 2009; Reynolds and Fabian 2008). Thus the shape of the observed Fe $K\alpha$ line becomes a link to not only how far inward the disk goes but indeed what type of black hole the object hosts – as it is the spin parameter that determines the location of the innermost stable orbit ([Fig. 7-25](#)). However, in radio-loud objects, these features can be overshadowed by the continuum from the jet (which will be discussed in [Sect. 7](#)). In addition, there appears to be an inverse correlation between the 2–10-keV X-ray luminosity and the equivalent width of the Fe $K\alpha$ line (Iwasawa and Taniguchi 1993; Nandra et al. 1997).

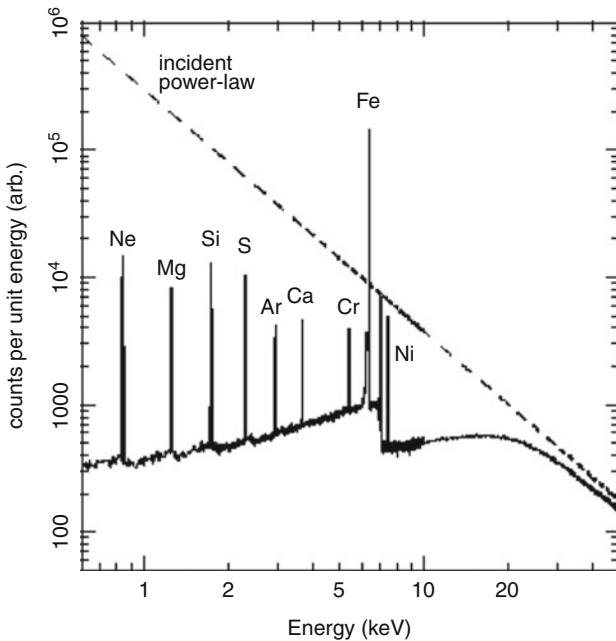


Fig. 7-29

Results of a Monte Carlo simulation demonstration of an incident power-law X-ray spectrum (shown by the *dashed line*) by a cold and semi-infinite slab with cosmic abundance (Figure from Reynolds (1996))

5 Emission Line Regions

As already discussed, one of the original characteristics by which AGN were first identified is their strong line emission in the optical. This is a property displayed by the great majority of all AGN, with the exception of BL Lac objects. The widths of these emission lines are generally interpreted as Doppler velocities, as the alternate interpretation of thermal broadening would require temperatures $\sim 10^{10}$ K in the case of the broad lines. At that temperature, all atoms would be fully ionized so that no emission lines would be produced (in addition, a plasma at that temperature would efficiently produce e^+ / e^- pairs, and the resulting annihilation line at 511 keV is not observed in the Gamma rays).

To get a first idea of the distance scale at which velocities $\sim 10,000$ km s $^{-1}$ might be possible, one might suppose that the velocities are indicative of the local rotation around the central black hole. In this case, since

$$\nu_{\text{rot}} \sim \sqrt{\frac{GM}{R}} = \frac{c}{\sqrt{2}} \left(\frac{R}{R_S} \right)^{-1/2}, \quad (7.32)$$

one would expect a distance $R \sim 500 R_S$ for velocities $\sim c/30$. Hence, to a first approximation, the broad lines can be produced no closer to the black hole than $\sim 1,000 R_S$ (although this estimate was based on the assumption of rotational motion, the infall velocity for free fall is within a factor 2). The region in which these broad emission lines are produced is called the *broad-line*

region or BLR. By a similar argument, then, one would expect the narrow lines to be produced at greater distances from the central black hole, specifically at least 2 orders of magnitude more distance given that their widths are at least a factor 10 smaller.

5.1 Reverberation Mapping

A more direct way to measure the extent of emission regions in AGN and their geometry is provided by *reverberation mapping*. This technique, pioneered by B. M. Peterson (1993), utilizes the fact that heating and ionization of the BLR (for details see the ensuing discussion) are both accomplished by the central continuum source of the AGN, that is, the accretion disk. One would expect that variability in the accretion disk would therefore produce corresponding variations of the physical conditions in the BLR, and hence the broad lines observed. However, things are not quite as simple as that, as light (as with all other information) travels at a finite speed, namely c . If indeed a change in the continuum causes a change in the observed emission lines, then one would expect a delay $\Delta t \sim r/c$ between the change in the continuum and that observed in the emission lines – where r represents the distance between the regions where the two are produced. Thus what is done in reverberation mapping is that one correlates changes in a variety of emission lines to the changes in the UV continuum and thus infers the corresponding values of r , which correspond to the characteristic distances at which each of these lines are produced. One can also monitor different continuum bands to investigate the temperature structure of the accretion disk.

It should be mentioned that carrying out this technique is very demanding – one needs to continuously monitor the fluxes of both the continuum and lines (many of them) over a long period and then cross-correlate them against one another to look for correlated variability. The technique is illustrated in [Fig. 7-29](#) and [Fig. 7-30](#). Looking at the figure, it is important to point out the multiplicity of timescales that one needs to monitor: while the variations in the continuum and lines are on timescales of days to hours, the delays between the continuum and the broad lines occur on much longer timescales – months to a few years. Thus one needs to obtain data from many observatories in order to avoid gaps due either to bad weather or even the normal day-night cycle at single observing sites.

These campaigns (see [Fig. 7-31](#)) show that the BLR is typically at distances of light-months from the central black hole. Furthermore, the BLR extends over a wide range of radii, which consists of a variety of different layers; higher ionization potential lines are produced closer in to the black hole (and therefore have smaller delays observed) while lower potential lines are produced at greater distances from the black hole. For example, for the Seyfert 1 galaxy NGC 5548, for which [Fig. 7-30](#) shows the result of reverberation monitoring data, one obtains $r \sim 12$ light-days for $Ly\alpha$, about 26 light-days for C III], and about 50 light-days for Mg II. It should be noted that the finding that higher ionization potential lines are produced at smaller distances from the black hole is consistent with the observation that the higher ionization potential lines also tend to be broader than lines at lower ionization potential (Bentz et al. 2006, 2007). Interestingly, lines of higher ionization energy also tend to have a mean redshift that is systematically shifted blueward compared to narrower emission lines – thus hinting at a generalized outflow structure in which the BLR participates (see e.g., Risaliti and Elvis 2010). Another interesting finding from reverberation mapping data is that the extent of the BLR also scales with the luminosity of the AGN (Peterson et al. 2005; Kaspi et al. 2007; Bentz et al. 2009b) – larger BLRs are observed in more luminous objects and vice versa.

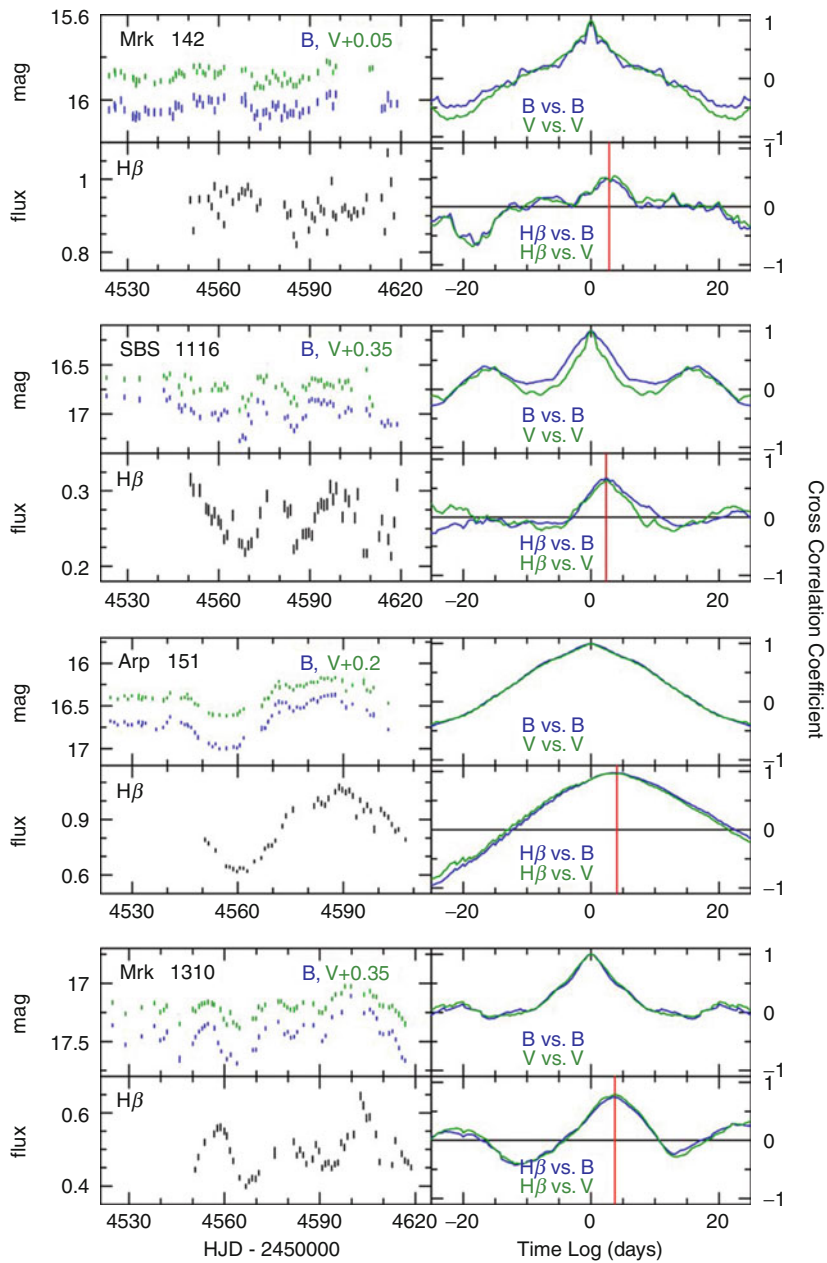


Fig. 7-30

Left panels: Photometric and H β light curves for Mrk 142, SBS 1116+583A, Arp 151, and Mrk 1310. The photometric measurements have units of Vega magnitudes, and the H β emission line fluxes have units of 10–13 erg s $^{-1}$ cm $^{-2}$. **Right panels:** Cross-correlation functions for the light curves. For each object, the top panel shows the auto-correlation functions of the photometric light curves and the bottom panel shows the cross-correlation of H β with the photometric light curves. The red vertical lines mark the location of the measured lag time (Figure taken from Bentz et al. (2009a, their Fig. 1))

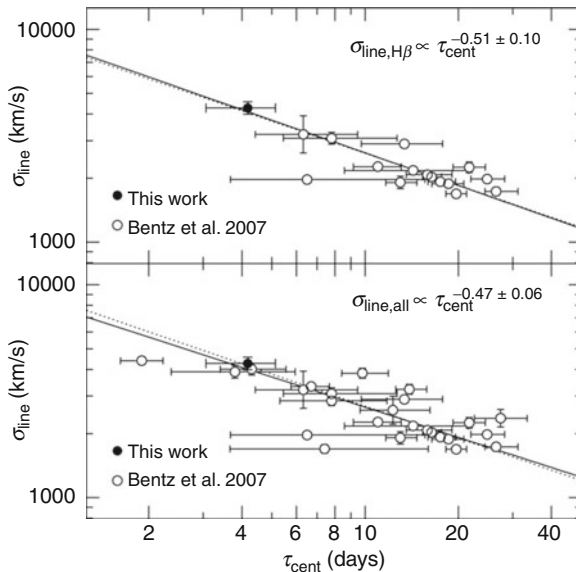


Fig. 7-31

Relationship between lag time and line width for several independent reverberation studies of NGC 5548. The *top panel* shows the relationship for $\text{H}\beta$ reverberation results only, while the *bottom panel* shows the relationship for all broad emission lines with reverberation results. The *dark circle* in each panel is the $\text{H}\beta$ result from this work, while the *open circles* are the compilation of results from Bentz et al. (2007) and references therein. The *solid lines* show the best fits to the relationship, with the slopes noted in each panel. The *dotted lines* show the relationship with the slope fixed at the value expected for a virial relationship, that is, -0.5 .

5.2 Physical Conditions in the BLR

The broad lines observed in AGN are nearly all permitted transitions typical of those seen in the warm interstellar medium. The BLR clouds are photoionized by energetic (i.e., UV and X-ray) continuum radiation from the AGN's accretion disk (See [Sect. 5.4](#)). This photoionization does not, however, represent the only heating source. There is clearly significant hydrodynamic heating as part of the generalized outflow that is taking place in the AGN, which the BLR clouds take part in. The main energy loss mechanism in the BLR clouds is emission of line radiation. Detailed photoionization models (e.g., Korista and Goad 2004, 2000; Korista et al. 1995; and references therein) are very successful at reproducing the line emission and line ratios seen in AGN ([Fig. 7-32](#)).

Those efforts use techniques similar to those used in ISM work (e.g., line ratios and the like) to fill in information regarding the temperature and density of BLR clouds as well as other information. What is found is that the typical densities in BLR clouds range from 10^7 up to 10^{11} cm^{-3} , near the critical density for $\text{CIII] } \lambda 1909$, thus making that line a very important diagnostic with higher values required for higher ionization potential lines, which (as detailed above) also appear to come from regions somewhat closer to the central black hole, while the lower values pertain to lower ionization lines. The typical temperature is around 20,000 K. Interestingly,

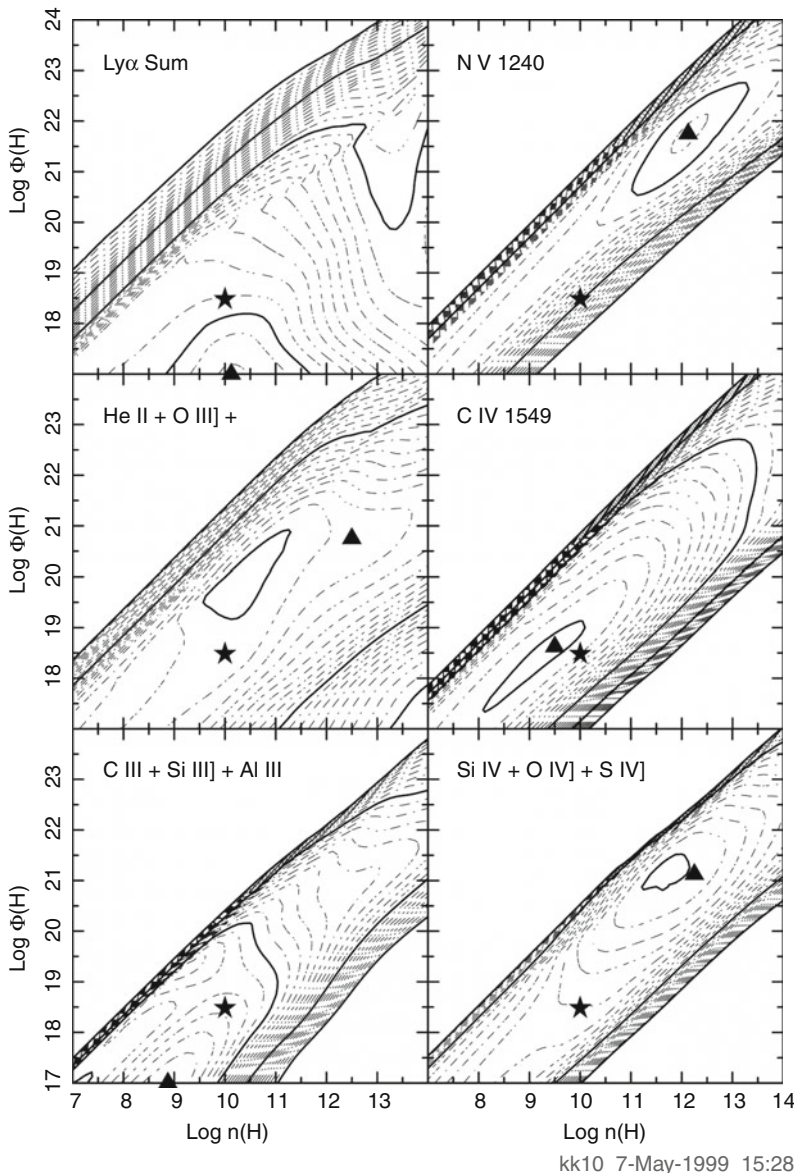


Fig. 7-32

Contours of $\log(\text{EW})$ for six prominent UV emission lines or blends, referenced to the incident continuum at 1215Å for full source coverage, are shown as a function of the hydrogen density and flux of hydrogen-ionizing photons. The total hydrogen column density within each cloud within the photoionization grid (generated using Cloudy; Ferland et al. 1998) is 10^{23} cm^{-2} . The EW is in direct proportion to the continuum reprocessing efficiency for that emission line. The smallest, generally outermost, decade contour corresponds to 1 Å; each solid line is 1 decade, and dotted lines represent 0.1 decade steps. The contours generally decrease monotonically from the peak to the 1 Å contour; the solid triangles mark the location of the peak of the dominant line within the blends (Ly α , He II, [C III], and Si IV). The solid stars are reference points marking the old "standard BLR" parameters. From Korista and Goad (2000)

the abundances seen in AGN broad-line regions do not appear to be typical of the interstellar medium. Arav et al. (2005, 2007) and Costantini et al. (2007), for example, find typically $\sim 2 \times$ solar abundances of C, N, and O in the outflow and broad-line region of Mrk 279, using data from HST, FUSE, and Chandra. The origin of these supersolar abundances is unclear, but it hints at links between the host galaxy (i.e., the number of stellar generations in an AGN nucleus) and the presence of AGN.

There is considerable controversy about the filling factor and number of clouds required for BLR. While HST observations (e.g., Gabel et al. 2005; Scott et al. 2009, among others) suggest a filling factor ~ 0.1 and a complex kinematic structure within the BLR, high-resolution spectroscopy (Arav et al. 1997, 1998) show that an extraordinarily high number of clouds – upwards of 10^7 and possibly upwards of 10^8 – are required to explain the smoothness of the broad-line profiles observed in bright, albeit low-luminosity Seyfert AGN such as NGC 4151 and Mrk 335. These two results are at least outwardly difficult to reconcile with one another; however, it is possible for both to be true in a turbulent region. However, the combination of this large number of clouds and filling factor ~ 0.1 indicates that the discrete clouds that make up the BLR must be relatively small, $\sim 10^{14}$ cm in size at most. This small size has significant implications for the stability (i.e., evaporation time) of BLR clouds, especially under these conditions.

5.3 Physical Conditions in the Narrow-Line Region

In addition to the broad emission lines discussed above, one also observes a variety of narrow-line features. Their typical line widths are ~ 500 km s $^{-1}$, considerably narrower than the lines of the BLR. By analogy to the BLR, the region in which these lines are produced is known as the *narrow-line region* or NLR. The strongest line from the NLR is, besides Ly α and C IV, the forbidden [O III] line at 5007. The existence (and indeed dominance) of forbidden lines implies that the gas densities in the NLR are significantly lower than in the BLR.

Like the BLR, the NLR gas is assumed to be photoionized by the UV and X-ray continuum from the central engine. Photoionization modeling is described in detail in [Sect. 5.4](#). From estimates analogous to those used for the BLR (see above), one can obtain the physical conditions of the NLR. An example of this work is shown in [Fig. 7-33](#).

It should be noted, however, that one cannot apply the technique of reverberation mapping, as no correlated variability has been observed, and the extent of the NLR is believed to be of order 100 pc. The line ratios of allowed and forbidden lines yield typical electron densities $n_e \sim 10^3\text{--}10^5$ cm $^{-3}$ for the gas where the lines originate. The typical temperature is $\sim 15,000$ K, similar to but perhaps slightly lower than the BLR, and the filling factor for the line-emitting material is significantly less than one – typically in the neighborhood of 10^{-2} . Hence one can use a similar geometrical picture as for the BLR, namely, that of line-emitting clouds, perhaps embedded in a generalized outflow.

Since the NLR is much more extended than the BLR, in nearby objects one can hope to resolve it with modern telescopes. An example of such data is seen in [Fig. 7-34](#). As can be seen, the morphology of the NLR is highly interesting – rather than spherically symmetric, it appears to show two cone-shaped regions on opposite sides of the nucleus. Thus it would appear as if the ionization of the NLR by the AGN's continuum radiation is not isotropic at these scales, but instead depends strongly on the direction. This is an observation which agrees strongly with unified schemes ([Sect. 6](#)).

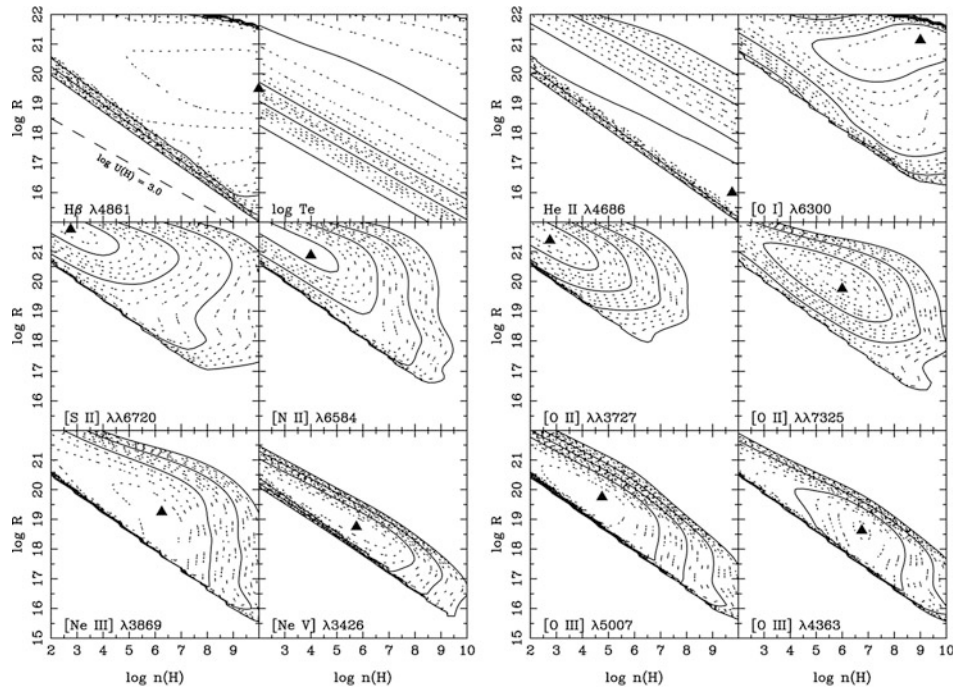


Fig. 7-33

Contours of constant logarithmic line EW as a function of $\log R$ (distance from the ionizing AGN, in cm) and $\log n(H)$ for the 23 emission lines indicated, referenced to the incident continuum at 4,860 Å. The cloud distance from the central ionizing source, R , was normalized assuming a $\log(L_{\text{ion}}) = 43.5$, and the grid computed using Cloudy (Ferland et al. 1998). The triangle is the location of the peak in the equivalent width distribution, and the contours decrease downward to the outer value of 1 Å. All points within the grid assume full source coverage. The upper right-hand plot in panel a is the $\log(T_e)$ at the illuminated face of the cloud. The temperature decreases from 10^7 K in the lower left-hand corner of the plot to 10^3 K in the upper right-hand corner. The bold lines represent 1 dex increments, and the dotted lines are 0.2 dex steps, for all panels (Figure taken from Ferguson et al. (1997))

5.4 Photoionization

As discussed above, the temperatures in the emission line regions of AGN are typically of order 10,000–20,000 K. How, then, do the regions around the central engine achieve a large enough abundance of ionized species to generate emission lines of highly ionized species, including [C IV], O III], etc.? Collisional ionization, which operates in supernova remnants and some other nebulae, cannot provide the answer: under pure shock-wave heating, the [O III] lines would require temperatures in excess of 5×10^4 K, and even higher for some of the higher-ionization lines. In addition, one expects a relationship between the temperature and degree of ionization, which is not observed. What is seen instead is a relatively constant temperature in both narrow

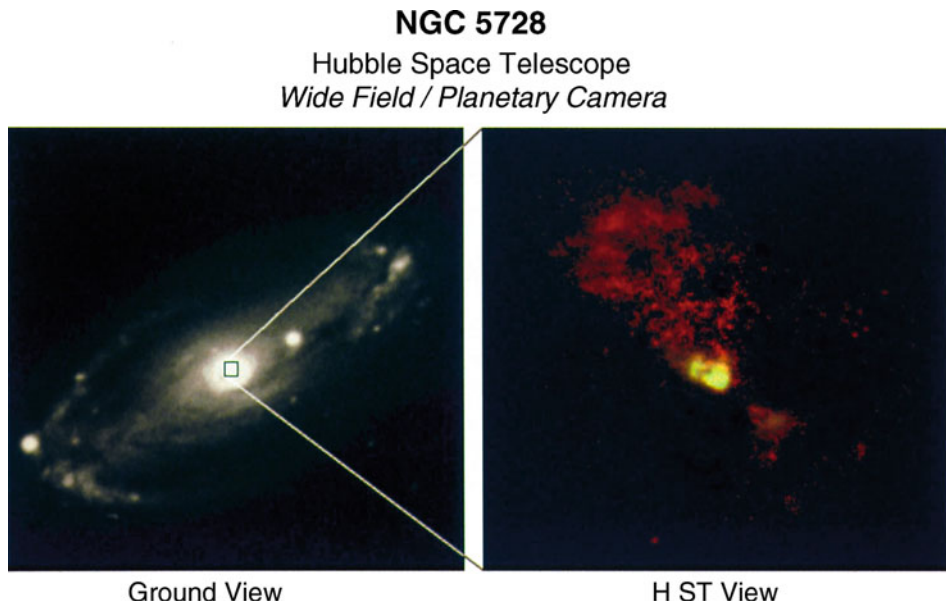


Fig. 7-34

Images of the Seyfert galaxy NGC 5728, showing its remarkable ionization cones. At left, a ground-based image of the galaxy. At right, a composite false-color image made from HST observations taken in the $\text{H}\alpha + [\text{NII}]$ and $[\text{OIII}]$ lines (Wilson et al. 1993). As can be seen, the ionized gas lies in two conical regions located on either side of the active nucleus; these regions represent the narrow-line region gas in this object

and broad emission line clouds, with a wide range of densities. Reverberation mapping campaigns also show that the highest ionization broad emission line clouds lie closest to the active nucleus (Fig. 7-31) – precisely where the flux of ionizing, high-energy radiation would be the highest. Moreover (Sects. 2 and 4), the active nucleus is a copious source of high-energy UV and X-ray emission, with a roughly power-law shape. Thus these considerations lead to the preeminence of photoionization as the primary excitation mechanism in both the broad and narrow emission line regions.

The physical balance in the broad- and narrow-line regions is dictated by the following concerns. Energy input to the emission line regions can come from both photoionization as well as hydrodynamic processes. The latter can include both generalized outflows (such as those in the model of Risaliti and Elvis 2010), as well as any interaction with the jet (in radio-loud objects) or obscuration lines. The primary method for energy output is via radiative cooling by collisionally excited lines, which increases rapidly with temperatures above 10,000 K, which is the temperature where hydrogen becomes dominantly ionized across a wide range of physical conditions. This fact tends to keep the temperature in the 10–20,000 K range over a wide range of input ionizing continua.

It is usually assumed that the photoionized gas is far enough from the central source that the gas can be modeled as an infinite slab. A given model will generally assume a constant density in the slab, with the gas in local thermodynamic equilibrium. The Boltzmann and Saha

equation are solved at each point, thus allowing the ionization and thermal structure to be determined within the gas along a radial direction from the central source. This will produce a depth-dependent opacity at every frequency as well as emission coefficients for different lines, allowing one to solve the equation of radiative transfer given the input emission spectrum. Several photoionization codes are in use; the most commonly used are CLOUDY (Ferland et al. 1998), Ion (Netzer 1990), and Xstar (Kallman and Bautista 2001).

The calculations these models do are quite complex, but the results can be encapsulated in two physical quantities: the number density and state of ionization. The number density is usually expressed in terms of the hydrogen column, whereas the ionization state is a more complex quantity, usually parameterized in terms of the *ionization parameter*, defined as the dimensionless ratio of the ionizing photon density to the electron density. In its simplest form – where ionization is done only by incident radiation – the ionization parameter can be expressed as

$$U = \frac{1}{4\pi r^2 c n} \int_{v_0}^{\infty} \frac{L_v}{h\nu} dv, \quad (7.33)$$

Here L_v is the ionizing luminosity per unit frequency interval above the Lyman limit (i.e., $h\nu_0 = 13.6$ eV), and n is the number density of the gas in the slab. This formalism can be extended fairly trivially to the case of collisional ionization by specifying a “pressure ionization parameter,” usually written as $\Xi = L/(4\pi r^2 c p)$, where p is the gas pressure.

The methodology one adopts is that one varies the density and ionization parameters until the predicted line luminosities match those observed. One must incorporate into the code all relevant atomic data, including recombination rates, ionization cross sections, charge exchange rates and the like. For each line, the luminosity is calculated, assuming that the total number of ionizing photons emitted by the central source must balance the number of recombinations in the ionized gas. These are of course related directly to the total number of line photons emitted in the gas. Thus, for any line, the equation of radiative transfer can be written (e.g., for H β)

$$L_{H\beta} = h\nu_{H\beta} \frac{\alpha_{H\beta}^{\text{eff}}(H^0, T)}{\alpha_B(H^0, T)} \frac{\Omega_{\text{ELG}}}{4\pi} \int_{v_0}^{\infty} \frac{L_v}{h\nu} dv, \quad (7.34)$$

where Ω_{ELG} is the solid angle covered by the emission line gas (so that $\Omega_{\text{ELG}}/4\pi$ is the covering factor), $\alpha_{H\beta}^{\text{eff}}(H^0, T)$ is the effective recombination coefficient for the H β line, and $\alpha_B(H^0, T)$ is the recombination coefficient for H^0 , such that the ratio of these two coefficients is the number of H β photons produced per hydrogen recombination. See, for example, Osterbrock and Ferland (2006) as well as Crenshaw et al. (2003) for detailed descriptions of the process and assumptions of photoionization models.

Thus once one has measured the input photon spectrum as well as the luminosity in each of the emission lines, one can calculate parameters for the regions where each line is generated using (7.33) and (7.34), with the former modified as appropriate for the line in question. It is the output of these calculations that has been shown in Figs. 7-32 and 7-33. Note also that this same procedure is used to model the ionization structure of any intrinsic absorption region (Sect. 6), where the models are iterated in density and ionization parameter to attempt to match the observed ionic column density.

Once these calculations have been done for each emission line, it is also useful to comment on the total mass of the BLR, which allows us to close the circuit begun at the beginning of this

section by discussing the mean radius of these regions. The luminosity in a given emission line can be rewritten as

$$L(H\beta) = n_e n_p \alpha_{H\beta}^{\text{eff}} h v_{H\beta} V \frac{\Omega_{\text{ELG}}}{4\pi}, \quad (7.35)$$

where V is the volume of the line emission region. Then, if one assumes roughly solar abundances, it can be shown that $n_e \approx 1.5 n_p$, and the mass of the region can then be calculated easily, as can its volume. The NLRs of the most luminous Seyfert galaxies have $L(H\beta) = 2 \times 10^8 L_\odot$, which gives a total mass $M_{\text{ion}} \approx 7 \times 10^5 (10^4/n_e) M_\odot$ if a roughly spherical NLR is assumed. Of course, this very elementary assumption does not pay attention to the underlying geometrical complexity of the emission line regions (e.g., [Fig. 7-34](#) for the NLR and [Fig. 7-31](#) for the BLR); however, it is adequate to an order of magnitude.

6 Nuclear Obscuration: Tori, Broad, and Narrow Absorption Lines

As shown by [Fig. 7-18](#), the basic picture underlying the unified scheme places a geometrically and optically thick cloud of gas, often described as the torus surrounding the broad-line regions along the equatorial plane. This obscuring region is central to our view of AGN – when viewing the AGN along an equatorial line of sight, the torus obscures the broad-line emission, but the narrow emission line region is still visible, resulting in a type 2 object. In comparison, a pole-on view would provide a direct view of both the narrow and broad emission line regions, resulting in a type 1 classification. The presence of the torus can account for the ionization cones commonly observed in AGN in both emission lines and polarized flux through shadowing of the ionizing radiation by the torus, resulting in the biconical shape shown in [Fig. 7-34](#) (e.g., Packham et al. 1997). The torus also accounts for the X-ray differences, where soft X-rays are at least partially absorbed during their passage through the torus (Maiolino and Risaliti 2007). In addition to the torus, there are other absorption regions in AGN, from which one observes a variety of line features. Both will be discussed in this section.

6.1 The Torus

By far the most ubiquitous and well known of these obscuration regions is the torus, which as already discussed is central to unified schemes. Before torus models are discussed in detail, it is important to note that torus models currently rank as the least well constrained of all the different parts of the unified scheme simply because of how recently good data became available. Classical models of the torus assumed for simplicity a uniform dust distribution within a large, extended obscuration region (e.g., Pier and Krolik 1992; Granato and Danese 1994; Efstathiou and Rowan-Robinson 1995). However, these models require large (100 pc scale) tori to produce long-wavelength emission, and fine-tuning to account for differences between types 1 and 2 sources. However, the mid-IR observations described in [Sect. 2.5](#) have thrown these notions largely into disrepute, as such a large, extended torus would easily have been resolved in nearby sources with ground-based observations. Moreover, such models fail to replicate the silicate feature characteristics and the extremely large ($N_H > 10^{24} \text{ cm}^{-2}$) column densities that X-ray data indicate for many sources.

More modern models of the torus must cope with size limits of only a few parsecs from the mid-infrared, as well as reverberation mapping observations (Suganuma et al. 2007) which

place the 1–2 μm emission region just outside the broad-line region, that is, typically at distances of a few tenths of parsecs in Seyfert galaxies and more distant in more luminous objects, in agreements with simple calculations for the dust sublimation radius. These results are difficult to explain under homogeneous, extended torus models, but are consistent with the new breed of compact, but patchy torus models whereby the distribution of dust is clumpy (Elitzur et al. 2004; Elitzur 2007; Elitzur and Shlosman 2006; Nenkova et al. 2008a, b; see Fig. 7-35). The fundamental distinction of the inhomogeneous density distribution is that radiation can freely propagate between different optically thick clumps.

The model formalism accounts for both direct heating by the AGN and indirect heating by the ambient clouds' emission, so some dense clouds remain cool to provide long-wavelength emission within a compact volume. It is relatively elementary to derive that under these assumptions, the intensity at a point s generated by clouds along a given ray is

$$I_\lambda^C(s) = \int_{s'}^s e^{-t_\lambda(s',s)} S_{C,\lambda}(s') n_C A_C(s') ds', \quad (7.36)$$

where $t_\lambda(s',s) = N(s',s)(1 - e^{-\tau_\lambda})' N(s',s) = \int_{s'}^s n_C A_C(s) ds$ is the mean number of clouds between s' and s ; n_C and A_C , respectively, are the number per unit volume and area of clouds along s ; and τ_λ is the optical depth at wavelength λ , and all clouds are assumed to be identical. This is an exact analog to the general solution of standard radiative transfer in continuous media. If radiation is propagating from s' to s , then it will have a probability of escaping that is equal to

$$P_{\text{esc}}(s',s) = e^{-t_\lambda(s',s)}. \quad (7.37)$$

Thus the only difference between clumpy and continuous media is that by integrating, one replaces the standard optical depth with its equivalent t_λ^s and the absorption coefficient is replaced by the product $n_C A_C$. Because of the particulate composition of matter, this equation is always valid in a statistical sense only, corresponding in principle to the intensity averaged along the same path over an ensemble of many sources with identical average properties.

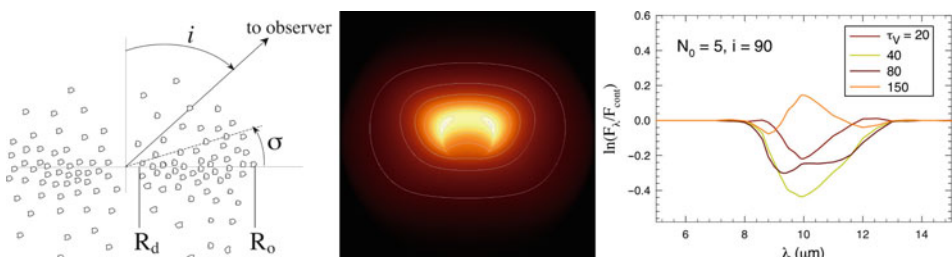


Fig. 7-35

Left: In the clumpy torus model, the clouds follow a power-law distribution with radius from the inner radius, R_d , to outer radius R_o . The clouds are concentrated in the equatorial plane, distributed with scale height s , which has a Gaussian edge (Elitzur et al. 2004). **Center:** Simulated image of NGC 1068 at 8.8 μm , with logarithmically spaced contours. The torus extends horizontally, but on the smallest scales; the images extend vertically because of optical depth effects. **Right:** Continuum-divided simulated spectra show a range of behavior of the 10- μm silicate feature, even at fixed viewing angle, i

To integrate a path containing a background source, such as the line of sight to the AGN, requires different handling since one cannot then average. For each line of sight, there are k intervening clouds, with Poisson probability P_k , and one then generates tabulations of intensities and their associated probabilities (I_k, P_k) with an actual source corresponding to one particular member of this probability distribution. Thus if the normalized spectral shape of the AGN radiation is $f_{e\lambda}$, the fraction of the AGN luminosity that emerges through a spherical shell of radius r centered on the nucleus is, on average,

$$p_{\text{AGN}}(r) = \int_0^1 d\sin\beta \int d\lambda f_{e\lambda} P_{\lambda,\text{esc}}(r, \beta). \quad (7.38)$$

where $P_{\lambda,\text{esc}}(r, \beta)$ is the probability for a photon of wavelength λ emitted by the AGN in direction β to reach radius r . Therefore, the fraction of type 2 sources in a given sample will be $f_2 = 1 - p_{\text{AGN}}(R_{\text{out}})$ where R_{out} is the outer torus radius.

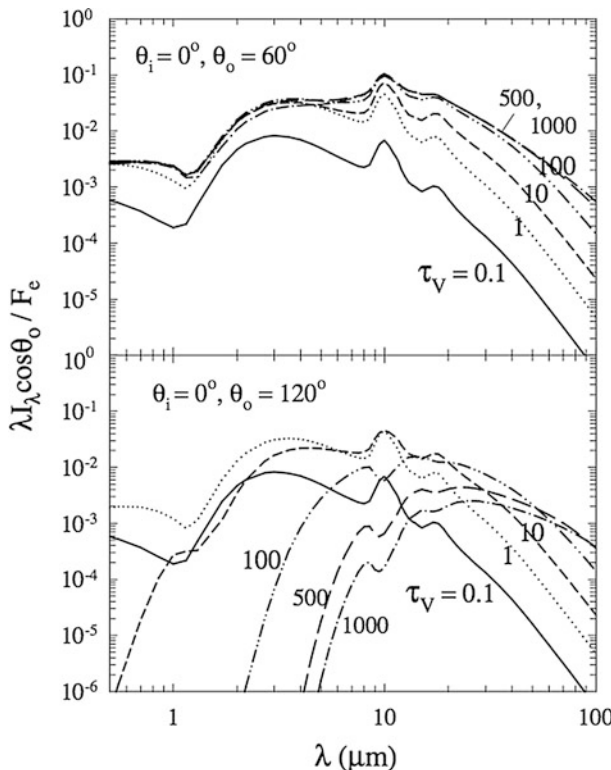
Within the clumpy models, one generally assumes a power-law distribution of clouds with radius from the inner radius, R_d (presumably where dust sublimates), to outer radius R_{out} . One general result is that there is no such thing as a single-temperature torus – the distribution of temperatures in a given cloud will be dependent on the optical depth within it, with the coldest dust temperatures found at the highest optical depth. Thus in this context it is important to understand that the radius for the 2-μm emission found by Suganuma et al. (2007) does not represent the inner radius of the torus but rather the mean distance of the torus clouds themselves because what Suganuma et al. would have measured would be just the dust in the outermost layers of clouds located in the torus, not necessarily those located in a certain part of the torus.

Figure 7-36 shows the spectral energy distribution of slabs illuminated by AGN radiation in the case of two different observer directions and a number of temperatures. As can be seen, the general features of AGN mid-IR continua (Sect. 2.5) are duplicated. Thus the clumpy models capture the broad spectral distinction of type 1 and type 2 AGN, with only the former affording direct views of the central engine and remaining bright across the entire UV-FIR bandpass, while producing nearly isotropic MIR emission. Most significantly, the models can reproduce the variety of observed MIR spectral characteristics, notably weak silicate absorption and emission, and a range of continuum slopes. The observations therefore provide powerful diagnostics of these physical conditions in the galaxies' central regions. Also, the emergent IR flux scales directly with the intrinsic luminosity of the AGN. Fitting a model to an observed spectrum therefore immediately reveals the power of the central engine, which is not otherwise evident in the obscured (type 2) cases.

6.2 Line Absorption

In addition to the above, AGN spectra contain a variety of line absorption features. This section will discuss only absorption that is *intrinsic* to either the AGN or its host galaxy rather than caused by intervening gas that lies by chance along the line of sight. While the latter features, seen in all AGN spectra, are interesting in their own right and place fundamental constraints on the physical state of the intergalactic medium and high-redshift galaxies, they are not germane to the subject of AGN physics.

Almost all varieties of AGN exhibit absorption, but its character seems to vary widely from one class to the next – both broad and narrow features are seen, with a large range in properties



■ Fig. 7-36

Optical depth dependence of the SED of clumpy slabs illuminated by normal radiation to a maximum temperature of 850 K. In the top and bottom panels, the observer direction is 60° from slab normal on the illuminated and dark sides, respectively (Nenkova et al. 2008a, their Fig. 8)

that is at some level luminosity dependent. However, one feature appears to be common among all of these absorbers, namely, that any velocity shift seen is toward the blue (as compared to the AGN's systemic velocity) – that is, the absorbing material is approaching us and must therefore be moving *away* from the AGN. This last fact will be discussed in detail at a later time; however, this discussion makes clear that these absorption lines offer a view into material that is flowing out from the active nucleus, driven by some process that is connected with the overall energy generation mechanism and hence fundamental to our understanding of the AGN itself.

The features observed in AGN spectrum range from features that are narrow (tens to hundreds of km s^{-1} in width) to extremely broad (from 1 to 50,000 km s^{-1}). The former are found in a majority of Seyfert galaxies, both in the optical/UV (e.g., Fig. 7-37) and X-ray (Fig. 7-14), as well as in many quasars. When observed in Seyferts, these features have typical widths of $20\text{--}400 \text{ km s}^{-1}$, while their more luminous cousins tend to have broader features, up to $\sim 1,000 \text{ km s}^{-1}$. The blueshifts of these features range from ~ 0 to $\sim 2,000 \text{ km s}^{-1}$ in Seyferts and up to $5,000 \text{ km s}^{-1}$ in more luminous quasars. These lines can be detected with only moderate spectral resolution and signal to noise, given their high column depth. Typically, these features are seen in C, N, and O in electric dipole transitions from the ground to high states – such as in the

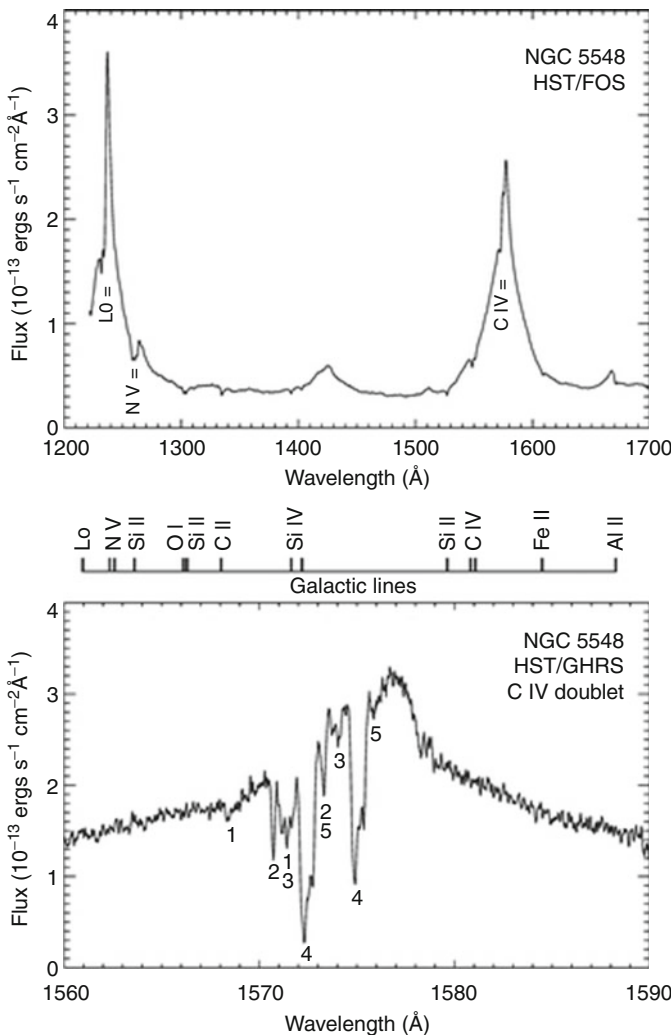


Fig. 7-37

HST spectra of the Seyfert 1 galaxy NGC 5548. The *top* panel shows a spectrum from the FOS and indicates positions of intrinsic UV absorption by H I Ly α and the C IV and N V doublets. The *middle* panel shows the locations of interstellar absorption lines in the *top* panel due to our galaxy. The *bottom* panel shows a high-resolution spectrum in the C IV region from the GHRS and identifies five kinematic components of absorption in the C IV doublet (From Crenshaw et al. (2003, their Fig. 1))

[C IV] λ 1549 doublet shown in Fig. 7-37. In some cases, absorption seen in other lines is also seen including O VI λ 1034, Si IV λ 1400, Ly α , and Mg II λ 2800. High-resolution observations reveal that these features are often quite complicated, as with the complex shown in Fig. 7-37, which has several components. These widths are much wider than the expected thermal widths (a FWHM of 9 km s⁻¹ would be expected for carbon at a temperature of 20,000 K). This indicates macroscopic motions within the absorbing gas.

A more spectacular form of absorption is seen in a minority of quasars, which exhibit broad features that extend from 1,000 to as much as 60,000 km s⁻¹ blueward of the quasar's systemic velocity (Weymann et al. 1991; see examples in [Fig. 7-38](#)). These features, like their less spectacular Seyfert cousins, are most often found in UV lines, although they are sometimes seen in the Balmer lines. These features are typically highly saturated – in fact, so much flux can be removed from the rest-frame ultraviolet spectrum that some quasars with these features (called BAL, or broad absorption line, QSOs) will drop out of flux-limited optical samples. Therefore, there is significant debate about the exact fraction of quasars with these features: although flux-limited samples suggest the number is less than 10%, the extreme nature of some BAL features suggests that the number may be significantly higher, perhaps as high as one-sixth (Reichard et al. 2003a) of all quasars.

A wide range of BAL quasar types are seen – in some objects, known as miniBALs, the lines are relatively modest in width (only a few thousand km s⁻¹ at most), while in others, the lines can be much broader. There is also a significant range in the types of lines where the BAL features are seen, with some objects showing them only in low-ionization lines (the LoBALs) and others showing them both in low- and high-ionization lines (HiBALs). The reader is referred to Reichard et al. (2003b) for the relative fraction of these subclasses, as drawn from the SDSS quasars. Delving into the taxonomy of each of these subclasses is beyond the scope of this work. However, their common feature is the overall spectral morphology, which shows a classic P Cygni-type line in the iconic objects, although in others where the absorption is heaviest and covers the largest velocity range, the amount of continuum and line emission that is absorbed makes the classical QSO spectral morphology of [Fig. 7-6](#) almost impossible to recognize.

Until very recently, BAL features were seen almost exclusively in radio-quiet objects. However, this is now known to be at some level a selection effect – BAL QSOs had first been identified in optically selected samples, and the complete radio-selected samples known at the time simply were not deep enough to contain these objects in significant numbers. This began to change with the identification of fainter radio quasars found in the FIRST sample (Brotherton et al. 1997, 1998) that were both clear BALs and clearly radio-loud. Later work with the SDSS verified that optically selected samples also contained these objects (insert comment about the fraction of these and whether there is any remaining dependence of BALnicity on radio-loudness).

The method that one would like to use to calculate the physical characteristics of these absorbing systems is similar to that used for the emission line regions: photoionization ([Sect. 5.4](#)). This is the method of choice for the narrow absorption systems; however, in the more spectacular BAL QSOs, it is by no means clear that hydrodynamic ionization does not play a significant role.

Let us first consider the narrow absorption systems. One clue to their origin lies in the fact that in nearly all AGN with such features, the depth of at least one component is sufficiently large to indicate that the gas absorbs both the incident continuum as well as the broad emission line flux (as in the case of component 4 seen in the spectrum of NGC 5548, [Fig. 7-37](#)). This material must therefore lie outside of the broad emission line region. Calculations based on photoionization models typically yield density ranges $n \sim 10\text{--}10^{10}$ cm⁻³ and ionization parameters of $\sim 0.01\text{--}1$ in the UV-absorbing gas; higher ionization parameters and densities are seen in the X-ray-absorbing gas. While these figures are somewhat lower than seen in the BLR, by itself this puts only loose bounds on the relative location of the absorbing gas, which from other considerations (see above) was already known to exist outside of the BLR.

A more recent constraint on this last question can be imposed from the existence of variability in these features, which is commonly observed on timescales of months to years

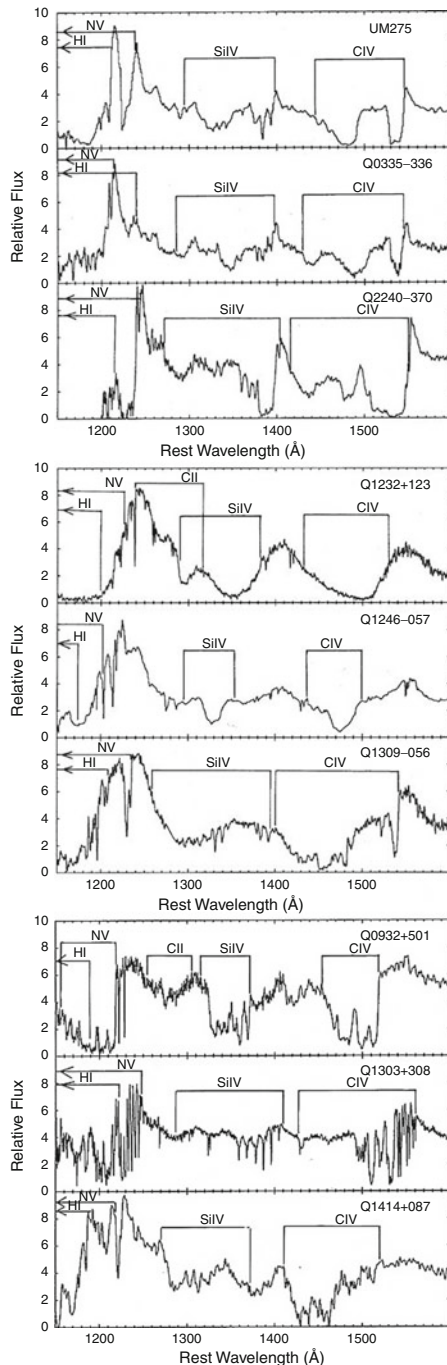


Fig. 7-38

Rest-frame ultraviolet spectra of several BAL quasars (Turnshek 1987, their Figs. 4–6). The features seen cover a considerable range in width and often consist of a complex of narrower subfeatures. In some objects, the features can completely destroy the classical QSO spectral morphology of Fig. 7-6

(e.g., Crenshaw et al. 1999, 2004; George et al. 1998; Kraemer et al. 2001a, b). Deep analysis of high-resolution, time-resolved spectra reveal that two mechanisms are at work: both changes in the ionization of the gas, due to variations in the ionizing continuum, as well as changes in the total column density due to, for example, bulk motion of the gas across the line of sight are required to explain the variability observed. Kraemer et al. (2001b) was able to map the absorbers in another Seyfert galaxy, NGC 4151, revealing a huge range in distances (from 0.03 to 2,150 pc from the nucleus, that is, extending from just outside the BLR to the larger galactic environment), number densities ($n \sim 10^{-3} \times 10^9 \text{ cm}^{-3}$), and column densities ($N_H \sim 10^{18} - 3 \times 10^{21} \text{ cm}^{-2}$). Both number and column densities typically decrease with distance, but there are no other obvious correlations with distance.

BAL features are much more difficult to model. One reason for this lies in the morphology of the lines – whereas the narrow absorption features found in Seyfert spectra are almost entirely contained within the broad emission line’s blue wing, this is not at all the case in BAL QSOs, which sometimes extend to blueshifted velocities much larger than the extent of the BLR. In addition, there is a much broader range of optical depths observed as a function of wavelength. Very often there are a significant range of wavelengths where the intensity goes to zero – that is, the broad absorption feature has removed essentially all flux from the spectrum. At other wavelengths, the absorption is only partial. The saturation of the absorption lines in many BAL quasars indicates that these flows are very high column densities – at least 10^{22} cm^{-2} and even higher, ranging up to 10^{24} cm^{-2} . Early X-ray observations also indicated that BAL quasars appear less luminous (Green and Mathur 1996), which more modern observations with *Chandra* and *XMM-Newton* suggest is due to the presence of large absorbing columns, which in several sources appear to be Compton-thick or nearly so (Brotherton et al. 2005; Shemmer et al. 2005; Gallagher et al. 2006; Giustini et al. 2008).

However, matters are not as simple as this. Naively, one would like to interpret the depth of absorption simply as an indicator of the optical depth and hence the absorbing column: where the flux goes to zero, the optical depth is several or higher, while where significant flux remains the optical depth is lower. However, the saturated nature of these systems means that particularly in the most optically thick systems it is very difficult to estimate the true column: the naïve calculation usually underestimates the true amount of material. This is partly due to the fact that the absorber does not have the same depth along all lines of sight to the continuum emission region (often referred to as *partial covering*). One might, for example, have very large optical depths along some rays and much less optical depth along others. The correct mean column density, averaged over the continuum source’s projected area, is then seriously underestimated. Another complication is that higher-resolution observations of many BALs find that they have a considerable complexity in structure (● Fig. 7-38), similar to their narrower cousins. In this case, also, what appears to be partial absorption and modest optical depth could in fact be much larger optical depth at some velocities, but no absorption at others. The inference of partial covering is strongly supported by the observation that BAL quasars are much more highly polarized than non-BAL objects, with polarizations as high as 10%, concentrated in the absorption troughs (e.g., Ogle et al. 1999 and references therein). The simplest explanation of this is that the polarized light is scattered by dust in the BAL clouds by a mechanism similar to that invoked for Seyfert galaxies (e.g., electron scattering, as discussed by Wang et al. 2005). This also means that the polarized light was originally emitted along another line of sight than ours, and thus the column along that line of sight is different than our own.

Modeling of BAL systems indicates a higher ionization parameter than in narrow absorption systems, typically at least 1–10 given the presence of N V and O VI BAL features, but not too much higher, as Mg II, CIII] C IV are also seen. It is possible, if not likely, that a range of

parameters is seen, but more work needs to be done here. It should also be noted that in BAL systems the ionization balance is also more complex, likely having contributions from both photoionization as well as hydrodynamic mechanisms. The distances of BAL regions from the central engine is not well constrained by ionization models. The best constraints come from observations of variability on timescales of months to years, which suggests distances of light-years or less from the nucleus. This is on the same scale as the BLR in quasars, as opposed to the narrow absorbers which are typically more distant. Another rough constraint can be derived from the fact that BAL features often absorb both line and continuum flux: this fact indicates that at least some of the BAL region lies beyond the BLR, although some overlap is possible.

The best estimates of the densities in BAL regions come from the combined use of ionization models with variability data, as pointed out by Krolik (1999). If, for example, the column density is observed to decrease along with the object's luminosity, then one may infer that recombination dominates ionization so that

$$n_e \approx 10^4 \left(\frac{\Delta t_{\text{rec}}}{1 \text{ year}} \right)^{-1} \left(\frac{Z_{\text{eff}}}{4} \right)^{-2} \text{ cm}^{-3} \quad (7.39)$$

where Z_{eff} is the charge of the ion and Δt_{rec} is the timescale for an order unity change in the ionic abundance due to recombination. Alternatively, if the column density increases as the flux does, one would suggest that ionization by the increasing flux caused the change. Because the absorbing matter is exactly along the line of sight, it sees the same ionizing luminosity, so one can infer both an estimated location for the absorber (relative to the nucleus) as well as a density:

$$r \approx 500 \left(\frac{L_{\text{ion}}}{10^{45} \text{ erg s}^{-1}} \right)^{1/2} \left(\frac{\Delta t_{\text{ion}}}{1 \text{ year}} \right)^{1/2} \left(\frac{Z_{\text{eff}}}{4} \right)^{-2} \text{ pc} \quad (7.40)$$

$$n_H \approx 10^3 U^{-1} \left(\frac{T}{10^4 \text{ K}} \right)^{-1} \left(\frac{\Delta t_{\text{ion}}}{1 \text{ year}} \right)^{-1} \left(\frac{Z_{\text{eff}}}{4} \right)^2 \text{ cm}^{-3} \quad (7.41)$$

where Δt_{ion} is the timescale for an order unity change in the ionic abundance (note that in this case photoionization dominates over any pressure terms). A third alternative is that the column might vary independently of the object's luminosity. In this last case, no such estimate is possible as the changes would be the result of the cloud moving across our line of sight. It should be noted that similar methods can also be used to infer the distance and density of narrow absorbing clouds.

The exact geometry associated with these absorbing clouds is uncertain. The fact that the narrow and broad variety of absorption features at least partially eat into the broad emission lines suggests that the material must be at a different orientation than the torus, discussed in the last section, as originally suggested by Weymann et al. (1991) for BAL QSOs. However, this is not at all clear, and more complicated geometries are certainly possible, particularly with a patchy torus composed of discrete, higher-density clouds as envisioned in the most recent models. What is, however, known is that these absorption features are evidence of large-scale mass outflows in AGN.

The kinematics observed in these lines show that the clouds that produce them are moving out from the nucleus with velocities of hundreds to tens of thousands of km s^{-1} , at distances of parsecs or more away from the nucleus. Such a flow will carry considerable momentum and will deposit large amounts of energy into the regions that surround the AGN, in the process

also taking away from the active nucleus's immediate environs material that might be used to fuel future activity. The rate at which mass flows out is

$$\begin{aligned}\dot{M} &= 4\pi C_{\text{abs}} r \mu_H \langle v \rangle N_H (r/\Delta r) \\ &= 0.04 \left(\frac{r}{\Delta r} \right) \left(\frac{C_{\text{abs}}}{0.1} \right) \tau_{\text{CIV}} \left(\frac{X_{\text{CIV}}}{10^{-4}} \right)^{-1} \left(\frac{\langle v/c \rangle}{0.05} \right) \left(\frac{\Delta v/c}{0.1} \right) M_{\odot} \text{ year}^{-1}\end{aligned}\quad (7.42)$$

where μ_H is the mean mass per H atom, r is the distance of the absorbing gas from the active nucleus, Δr is the radial thickness of the absorbing shell, $\langle v \rangle$ is the mean outflow velocity, ϵ is the efficiency of accretion, τ_{CIV} is the optical depth in the C IV line, and X_{CIV} is the abundance of C IV. Particularly in luminous objects (e.g., quasars), this can be an interesting fraction of the accretion rate:

$$\frac{\dot{M} c^2 \epsilon}{L} = 0.025 \left(\frac{r}{1 \text{ pc}} \right) \left(\frac{C_{\text{abs}}}{0.1} \right) \tau_{\text{CIV}} \left(\frac{X_{\text{CIV}}}{10^{-4}} \right)^{-1} \left(\frac{\langle v/c \rangle}{0.05} \right) \left(\frac{\Delta v/c}{0.1} \right) \left(\frac{L}{10^{46} \text{ erg s}^{-1}} \right)^{-1}. \quad (7.43)$$

Thus the existence of these clouds actually constitutes a major problem for BAL quasars as it can remove from the nuclear regions almost as much matter as is accreting into the black hole! Thus in these objects one is almost forced to conclude that the BAL stage must be transitory, a point discussed also later.

A second question one must ask ourselves before leaving the subject of these outflows is, exactly how are they driven? A number of mechanisms have been devised, including both thermal and radiation-pressure driven mechanisms. If one assumes that the gas is heated to a temperature such that its thermal energy matches its gravitational binding energy, then matter may be injected at some point; exposed to the AGN's radiation, its temperature rises, and once its temperature increases beyond the critical value, it is expelled. For this mechanism to work, a heating mechanism is needed. Many are possible, including photoionization, Comptonization, and collisions with energetic particles (see Begelman et al. 1991). If the heating rate is parameterized by that due to Comptonization, which may not be too bad an approximation as the rate of photoionization will be roughly dominated by radiative cooling, then the heating criterion is

$$\frac{L \sigma_T}{4\pi r^2} \frac{4k_B T_C}{m_e c^2} \frac{\phi}{\mu_e} > \frac{(GM)^{3/2}}{2r^{5/2}} \quad (7.44)$$

The above assumes that gas is injected with the kinetic energy that corresponds to a circular orbit at radius r , μ_e is the mean mass per electron, and ϕ describes how different the true heating rate is from that derived from Comptonization. Once the wind takes off, its temperature may not need to maintain the Compton temperature T_C referred to above, because adiabatic expansion can compete with radiative heating. If one assumes that the wind achieves a Mach number of order 1, then the Compton heating rate is balanced by an effective cooling per (mean) unit mass $\sim (k_B T / \bar{m})^{3/2} r^{-1}$. That dictates a temperature of

$$\begin{aligned}T &\sim \frac{\bar{m}}{k_B \phi^{2/3}} \left(\frac{4k_B T_C}{m_e c^2} \right)^{2/3} \left(\frac{L \sigma_T}{4\pi r \mu_e} \right)^{2/3} \\ &\sim 5 \times 10^6 \left(\frac{T_C}{10^7 \text{ K}} \right)^{2/3} \left(\frac{L}{10^{45} \text{ erg s}^{-1}} \right)^{2/3} \left(\frac{r}{1 \text{ pc}} \right)^{-2/3} \text{ K}.\end{aligned}\quad (7.45)$$

This assumption also allows us to estimate the maximum electron scattering depth as $\tau_{T,\text{max}} \sim U^{-1} (\nu_{\text{orb}}/c_s)^2 (L/L_E)$. In a thermally driven wind, the ratio of orbital speed to sound

speed will be ~ 1 , and because the critical ionization parameter for evaporation is ~ 10 (see the discussion in Chap. 10 of Krolik 1999), one can thus expect optical depths $\sim 0.1L/L_E$ whenever the luminosity is large enough to create the wind. These inferred conditions match fairly well to those found in the warm X-ray absorbers associated with Seyfert galaxies. If the terminal Mach numbers are few, then these winds can be expected to flow outward at several hundred km s $^{-1}$ and develop clouds within the flow that are at temperatures of tens of thousands of degrees, which would match the properties of the narrow absorbers found in Seyfert 1 spectra.

Thus thermal mechanisms can drive the narrow absorption features but fail to achieve the velocities necessary to drive the winds in BAL quasars. In those objects, radiative driving must dominate. This mechanism is much more difficult to calculate, but if one assumes that the primary driving mechanism is due to Thomson scattering, photoionization codes may be used to compute the distribution of opacities $dN_l/d\kappa(U)$, that is, the number of lines N_l with center opacities κ . The equation of motion is then

$$v \frac{dv}{dr} = \frac{GM}{r^2} \left[-1 + \frac{L}{L_E} M(N_H, U) \right]. \quad (7.46)$$

where $M(N_H, U)$ is a force multiplier that expresses the efficacy of line-driving over Thomson scattering. This parameter can be as large as 10–100 if the C IV line is marginally optically thick. It should be noted that radiative driving, augmented by winds, is a mechanism used to power the outflows in OB stars, so its presence in quasars should not be surprising. Calculations by Proga et al. (2000) and Chelouche and Netzer (2001) indicate that this mechanism can reach the velocities necessary to drive BAL outflows.

7 Jets and Lobes in Radio Loud AGN

The distinguishing feature of radio-loud AGN are their jets, as well as the hotspots and lobes seen at larger scale. These are features that, as already discussed, are also present in a significant number of radio-quiet AGN as well, albeit at much lower power levels.

7.1 Acceleration of Jets

A suite of both modeling and observational evidence indicates that these jets must originate deep within the central regions of an active nucleus. On the observational side, the evidence comes from high-frequency VLBI mapping of the M87 jet (► Fig. 7-39, Walker et al. 2009; Krichbaum et al. 2006), which shows that the jet extends very close to the central black hole and even reveals the location where collimation is taking place. The expansion of the jet's "cone" appears in these images on scales smaller than 0.5 milliarcsec, which corresponds to about 150 R_S for M87, and it continues in to distances of 0.1 milliarcsec from the VLBI core, which likely constitutes the base of the jet. Therefore, whatever process first collimates these relativistic outflows must occur on very small scales – within no more than 30 R_S from the black hole. Interestingly, however, the monitoring program that generated the images shown in ► Fig. 7-39 did not show motions as fast as those seen on larger, arcsecond scales (► Fig. 7-22), where speeds as high as $\sim 6c$ have been seen. On milliarcsecond scales, it is necessary to image the jet every few weeks to reveal relativistic motions, but indeed, speeds as high as $2c$ are seen in the monitoring data. On the smallest scales (within 0.5 milliarcsec), the *counterjet* – that is, the flow that

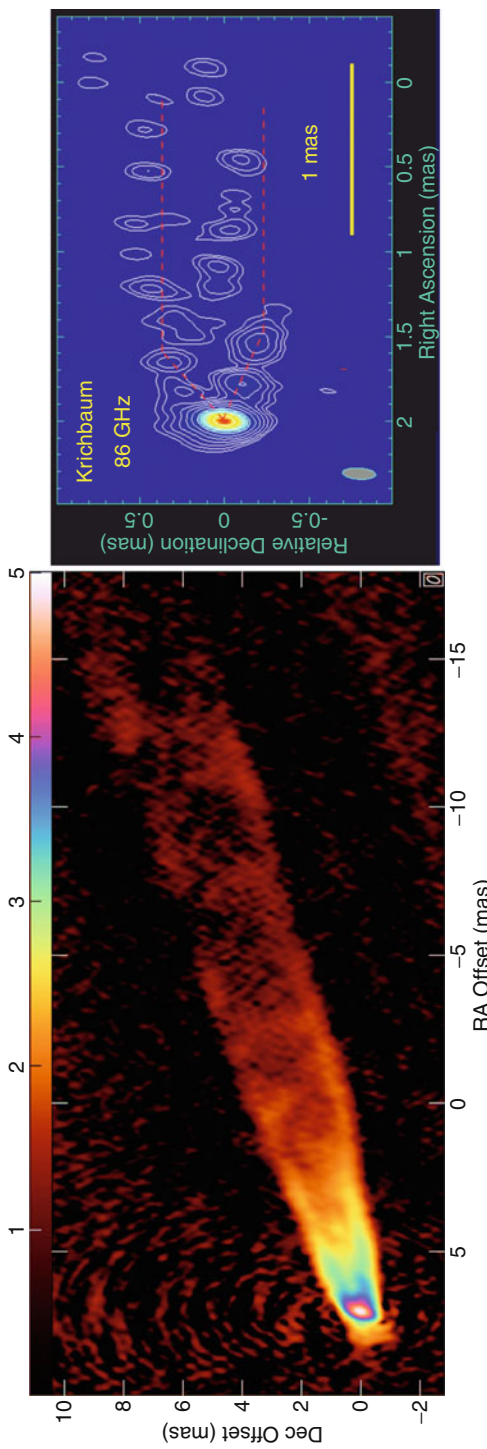


Fig. 7.39

High-frequency VLBA mapping of the M87 jet, at (at left) 43 GHz and (at right) 86 GHz. These images show the very innermost workings of a radio jet. Importantly, note that the jet takes up a constant angle up until the very smallest scales, when the 86-GHz image reveals that the initial expansion and collimation region can be seen (traced out by red dotted lines) within the innermost 0.5 millisecond of the jet. For reference, at the distance of M87 (16 Mpc), 1 millisecond is 0.078 pc = 16,000 AU, or 300 times the Schwarzschild radius for a $3 \times 10^9 M_\odot$ black hole (Figures from Walker et al. (2009) and Krichbaum et al. (2006))

emerges in the direction opposite to the jet seen at arcsecond scales – is measured. One can also see in [Fig. 7-32](#) that the images of the jet have a very edge-brightened appearance. This suggests that they are located along the jet’s outer edge, often called the “sheath.” Only much fainter components can be seen in the inner part of the jet’s cross section, the “spine.” Many jet models (e.g., Ghisellini et al. 2005) postulate that the spine should move at faster speeds, similar to the center of the flow of a fire hose. There are no detected motions in this central region, but the data are not deep enough to say this with confidence. However, it is clear that the *acceleration* process must take place over a significantly larger scale than does the *collimation* of jets.

This recent observation set constitutes a challenging goal for models of jet generation to meet – they need to be able to simulate the region very close to the central black hole, certainly within a few tens of gravitational radii if not all the way to the ergosphere. Thus any model for jet generation must include both special and general relativity, as well as a variety of other physics, most particularly magnetohydrodynamics (MHD). Moreover, if it is to model the generation, acceleration, and collimation of the jet, it needs to cover a large dynamic range in angular scale. This makes it very challenging for computational modeling. Because of this complexity, models of jet generation typically make a number of simplifying assumptions, in particular that of axisymmetry, as well as essentially infinite conductivity, which together allow the equations of ideal, relativistic MHD to be cast in a semianalytic form (e.g., Li et al. 1992; Contopoulos 1994; Meier et al. 2001; Vlahakis and Königl 2003, 2004) via self-similarity arguments.

It is beyond the scope of this chapter to give a full treatment of the equations of MHD. However, the differences between regular fluid flow and ideal MHD flow can be understood by referring to [Fig. 7-38](#) (left-hand panel), which shows a three-dimensional GR-MHD simulation of a magnetized jet’s propagation. As shown by [Fig. 7-40](#), the magnetic field lines thread the plasma and are frozen in. These field lines restrict the flow of plasma to the parallel direction. Moreover, if the field is strong (i.e., if the plasma’s hydrodynamic pressure ρv^2 is less than the magnetic pressure $B^2/8\pi$) and anchored in a rotating star or disk, then any plasma trapped in the field will be flung centrifugally outward along the field lines. Another important point is that parallel magnetic field lines tend to repel each other. This produces a pressure on the plasma perpendicular to the field lines due solely to the magnetic field. A weak field can thus be strengthened by bringing together many weak parallel lines of force to produce the equivalent of a few strong ones. As a result, compression perpendicular to the field lines or toroidal coiling can enhance the field. Finally, magnetic field lines do not maintain a curved shape unless they are acted on by forces from the plasma or other field lines – if left alone, they will straighten like springy wires, and if coiled in a hoop or spiral, the field will try to shrink around its axis to eliminate all but the straight axial component.

Simulations ([Fig. 7-40](#), center and right panels) begin with a disk that is initially in rotational equilibrium about the central black hole. Such a disk naturally rotates differentially. The disk is also threaded with an axial (vertical) magnetic field that is sufficiently strong to exert a braking force on the rotating plasma. As the simulation progresses, the magnetic field’s braking force removes angular momentum from the torus, transferring it up along magnetic field lines into the coronal plasma, which is also frozen to the field lines. As these rotating magnetic twists propagate out, they push out and pinch the coronal plasma into a spinning jet. As the disk material loses angular momentum, it falls toward the central object, releasing half of its gravitational energy into kinetic energy of rotation that continues to power the outflow. Thus the production of a high-velocity outflow or jet is a natural and mandatory byproduct of the accretion process where a strong magnetic field is present. The same process that generates the jet is also behind the magnetorotational instability, and therefore it may be that the presence of

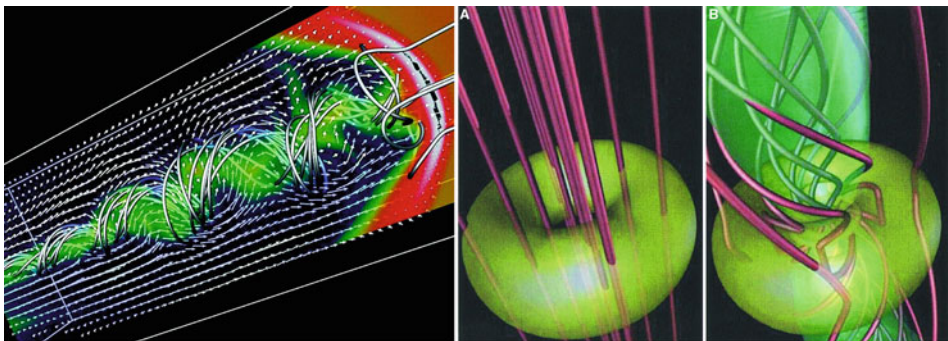


Fig. 7-40

Propagation (left) and generation (center and right) of a magnetized jet by a supermassive black hole and its accretion flow. The diagram at left shows flow velocity (arrows), plasma density (colors, with white and blue lines indicating high and low pressure, respectively), and magnetic lines of force (metallic tubes). In this simulation, the initially axisymmetric, rotating jet has developed a helical-kink instability that distorts its shape; such an instability may explain some of the wiggles observed in parsec-scale jets. The feature at far right in this diagram is a strong shock wave generated as the super-Alfvénic flow propagates into a region with decreasing Alfvén velocity. The diagrams at center and right were generated from a simulation that included a thick, magnetized toroidal disk surrounding a central $10^8 M_\odot$ black hole. The center panel shows the initial state, with the disk in rotational equilibrium with the axial magnetic field. As time goes on, the differentially rotating disk drags the field lines in the azimuthal direction, creating a braking force that allows material to accrete inward and gain additional rotational energy. This produces a torque on the magnetic field and generates a spinning plasma jet that carries away matter, angular momentum, and energy, producing the configuration seen at right (Figures from Meier et al. (2001, their Figs. 2 and 5))

such an axial magnetic field and hence the jet is a critical factor in removing angular momentum from disk material as it spirals inward toward the black hole.

Most simulations show that the speed of the ejected outflow is close to the escape speed at that radius – in other words, the magnetic field lines that are anchored to the disk closer in to the black hole will produce a faster flow than those that are anchored at greater distances. Thus these simulations reproduce the fire-hose-like velocity structure (“spine-sheath,” see above) hinted at by the high-frequency VLBA images of M87. Simulations have been done both for nonrotating (Schwarzschild) black holes as well as strongly rotating (Kerr) black holes. An outflow is generated in both cases, with a speed that is directly related to the escape velocity at the location of the innermost stable orbit, which represents the accretion disk’s inner edge. In the Schwarzschild case, the innermost stable orbit is at $3 R_S$, which makes the jet production region slightly larger, and hence the speed of the outflow is $\sim 0.5c$. However, in the maximal Kerr case, stable orbits can exist right down to the event horizon, making the center of the jet production region much smaller (similar in size to the ergosphere) and generating a faster outflow ($\sim 0.9c$, i.e., Lorentz factor $\Gamma = 2$). Thus the production of a relativistic jet is most likely tied to the spin of the black hole. Furthermore, even if the disk surrounding a Kerr black hole is initially given no rotation, a jet is still formed. This is because as matter plunges in to the ergosphere, it becomes caught up

in the rotating space around the black hole and then routed out into the jet. Thus the production of the jet is intimately rooted in the coupling of the magnetic field with the black hole's spin – the so-called Blandford–Znajek (1977) mechanism.

It should be mentioned that the generation of jets through a thin accretion disk produces a rather small luminosity. Therefore most jet generation models require a thick, more toroidally shaped disk. This can be produced by advection-dominated accretion flows (ADAFs), where most of the disk's thermal energy is carried into the black hole, as well as convection-dominated solutions. These increase the power that one can generate through the Blandford–Znajek mechanism by orders of magnitude. However, to produce the most luminous quasars, it appears necessary to combine the Blandford–Znajek mechanism operating on a thin disk with a rapidly rotating Kerr black hole. This will have the effect of naturally thickening the disk on small scales, through the frame dragging near the black hole's ergosphere.

One additional factor must be considered, namely, the fact that the Blandford–Znajek mechanism does not by itself appear to accelerate jets to speeds fast enough to account for those seen in VLBI monitoring (up to $40c$), nor can it account for their collimation. To get Lorentz factors up to 40 requires an additional, distributed acceleration process. This is provided by ideal MHD acceleration, which is by itself quite efficient, and powered by the pressure gradient in the toroidal magnetic field within the rotating jet. It can be thought of as akin to the gradual unwinding of a twisted rubber band and is by its very nature spatially extended. It naturally produces a rough balance between the Poynting and kinetic fluxes. The process develops naturally with the jet core due to compression by the hoop stress in the toroidal magnetic field. It is this same process that helps to confine the inner core of the magnetic field; however, the outer sheath of the jet must be confined by external pressure. These two can be driven together by a disk wind, which might develop hydrodynamically and are also seen in radio-quiet AGN.

Another issue that is not well constrained is the makeup of jets – whether they are positron/electron pair plasma, hadron dominated, or carry most of their energy as Poynting flux. Part of the problem is that there are no easy diagnostics given the nearly complete ionization of the jet material. Various methods have been derived to answer this issue, most of which have so far come up with a negative answer, both at large and small scales, most of which have to do with using the jet material as a Comptonization target (see [Sect. 7.3](#)) and then predicting the response. For examples, see Georganopoulos et al. (2005), Begelman and Sikora (1987), and Sikora et al. (1997).

7.2 Propagation and Dynamics of Jets at Larger Scales

Once launched, the jet can carry away a major fraction of the kinetic power and angular momentum that was within the disk. A jet of high power thus will remain collimated for very long distance, flowing through the galaxy and out beyond it into the surrounding cluster – as is indeed seen in virtually all sources. As the jet propagates, the magnetic field is carried along with it, and once the jet has reached its terminal velocity, the magnetic field lines will be essentially along the jet direction.

Jets are prone to a number of instabilities. Included among these are Kelvin-Helmholtz instabilities, as well as waves, pinches, and bends. Simulations of these have been performed by many workers, including Aloy et al. (2003), Hughes et al. (2002, 1996), Hardee et al. (2001, 2005, 2007), Hardee (2003), and Hardee and Rosen (2002). These simulations show that instabilities, perhaps combined with natural variations in the flow of material down the jet, can

produce many of the moving and stationary features in VLBI and VLA maps and also provide a natural mechanism for producing flares such as those seen in blazars as well as the M87 jet. As instabilities propagate, shock waves are generated, changing the direction of the local magnetic field.

Polarization observations, both in the radio and in the optical, reveal the complexity of many of these features. An example is shown in Fig. 7-41, which shows VLA and HST polarimetry of the jet of M87 (Perlman et al. 1999) on arcsecond (kiloparsec) scales. These maps reveal a wealth of detail, with complex structure in several of the knots, including evidence for compressed magnetic fields (as predicted in shock models) as well as rotations in the magnetic field. Several jet regions show a higher polarization at the jet edges, indicating shear by the surrounding interstellar medium. At least four inner jet knots show strong decreases of polarization at the position of the flux maximum. Closer examination of these figures shows that several of the knots have changes in optical polarization that are not seen in the radio. These include large

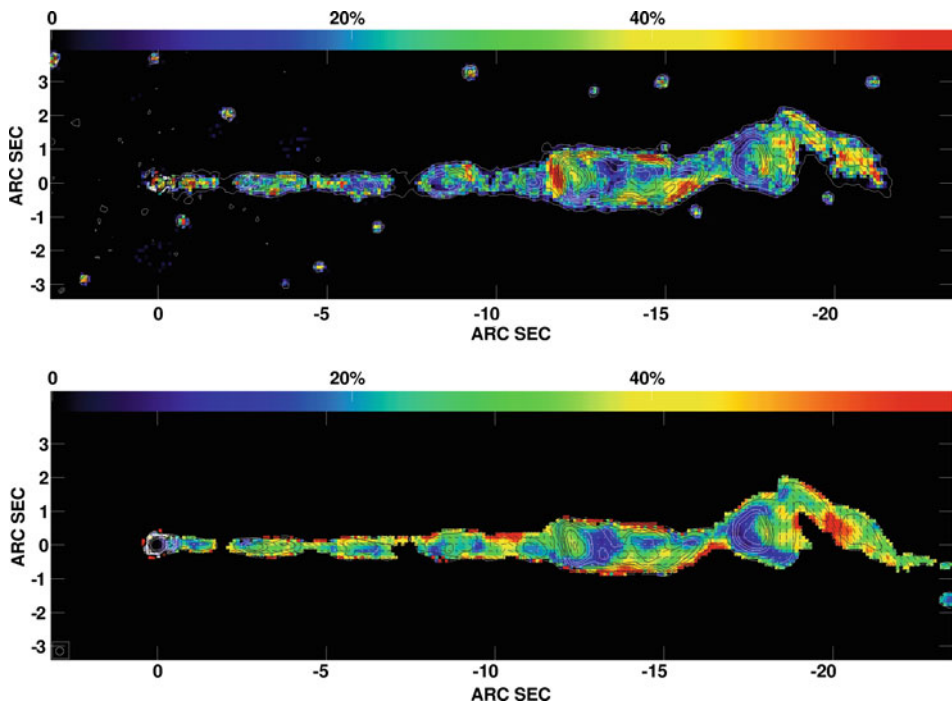


Fig. 7-41

Imaging polarimetry of the M87 jet, as obtained with the HST (top) and VLA (bottom). The colors indicate fractional polarization in each band, while the contours represent total flux in the optical and radio, respectively. A polarization of 20% is typical of what we see in the optical, with somewhat higher polarizations seen in the radio. The flux maximum regions of several knots exhibit large changes in the optical, including perpendicular magnetic fields and reduced polarization, that are not seen in the radio. These suggest that the optical emission from the M87 jet comes mainly from a region distinct from the radio emission (suggested to be the jet spine), while radio emission comes from the entire cross section (Figures adapted from Perlman et al. (1999))

rotations (near 90°) in magnetic field direction as well as decreases in the polarization fraction, in some cases to near zero. The explanation suggested for this phenomenon was that the optical emission and the jet shocks come largely from the jet's interior or spine region, while the radio emission comes from the entire jet cross section. Shocks would accelerate particles and thus be seen as enhanced emission first within the optical. Later multiband imaging (Perlman et al. 2001a) supported this scenario, as dramatic spectral index changes are seen in knot regions in the optical, but not in the radio. Later work on several other FR I radio galaxy jets reveals a similar pattern – not only do the jet dynamics reflect themselves in the polarimetry in the optical but also a spine-sheath pattern to the jet flow appears common, with more subtle changes also seen that indicate a variety of different disturbances in those jets, including twists as well as other features.

Emission at higher energies (optical, X-rays) is seen in over three dozen jets now, thanks to observations by the HST and Chandra (e.g., Fig. 7-42). The next section discusses the emission mechanisms for these large-scale jets in the next section; however, it is worth noting here that optical and X-ray emission from jets is often concentrated within the brighter knots in the inner jet and often does not appear to occupy the entire jet cross section.

Finally, it is worth discussing in this respect the effect that the jet will have on its surroundings. As the jet propagates, it carries with it an enormous amount of kinetic flux (up to 10^{61} ergs), and even though the flow is usually lower density than the surrounding medium, because of its high speed, it will deposit large amounts of energy into the surrounding regions. A number of effects can be stimulated, including star formation as well as hydrodynamic shockwaves that result in heating of the galactic and cluster medium. Simulations by O'Neill et al. (2005) indicate

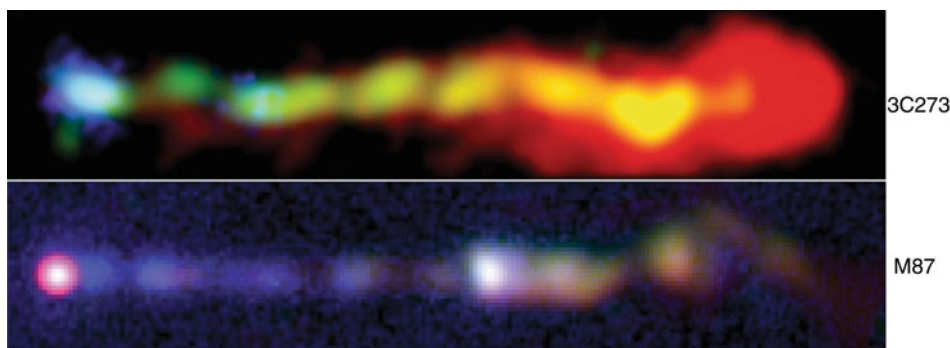


Fig. 7-42
Multispectral appearances of the jets of M87 and 3C273. The optically visible portion of the jet of M87 (shown) extends about 7,000 light-years from the nucleus (at left in the image at bottom) and feeds plasma to lobes that span 200,000 light-years. The bright portion of the jet of 3C273 extends for a projected distance of 90,000 light-years, beginning with a bright knot approximately 100,000 light-years from the host galaxy's nucleus (which is $12''$ off to the left side in the image shown). These figures were made using data from the radio VLA (red), infrared Spitzer space telescope (yellow), Hubble (green), and the Chandra X-ray observatory (blue). In both panels, red colors represent regions that are brightest in the infrared and/or radio, whereas blue colors represent regions that are brightest in the X-rays. Note that in both jets, the X-ray and optically bright regions of the jet do not occupy the entire cross section

that even light jets will deposit approximately half of their kinetic flux as thermal energy in the surrounding medium. Half of this would go directly into dissipative heating of the ICM, which is believed to be needed to support the reheating of the cluster gas against cooling flows. The remainder of the energy would reside primarily in the surrounding cocoon, which has been observed in jets on large scales (see Fig. 7-8 for examples). Interestingly, these same simulations show that jets at low Mach numbers are more easily bent and disrupted. As a result, it seems likely that the Fanaroff-Riley divide is not only a reflection of the power of the outflow and AGN process but also the Mach number of the jet flow.

7.3 Emission Mechanisms in Jets

The emission from the jets and lobes of active galaxies at lower (radio through optical) energies is normally interpreted in the framework of *synchrotron radiation* from relativistic electrons whirling around in the magnetic field of the jet. Basic electromagnetic theory shows that electrons in a magnetic field propagate along helical, that is, corkscrew-shaped paths, so that they are constantly accelerated by the Lorentz force. Accelerated electrons also emit electromagnetic radiation in the form of synchrotron emission. If an electron has Lorentz factor γ , this emission has a characteristic frequency

$$\nu_c = \frac{3\gamma^2 eB}{4\pi m_e c} \approx 4.2 \times 10^6 \gamma^2 \left(\frac{B}{1G} \right) \text{Hz}, \quad (7.47)$$

where B is the magnetic field strength, e is the electron charge, and m_e is the mass of the electron. For frequencies considerably lower than ν_c , the spectrum of a single electron is proportional to $\nu^{1/3}$, whereas at larger frequencies it decreases exponentially. As the synchrotron emission is seen over several decades of frequency, to a first approximation, the spectrum of a single electron can be considered as quasi-monochromatic, as it radiates over a very small energy range. To produce radiation at centimeter wavelengths in a $\sim 100 \mu\text{G}$ magnetic field, Lorentz factors $\gamma \sim 10^4$ are required, that is, the electrons need to be highly relativistic. To attain such high energies, particles must be accelerated very efficiently in the inner regions of AGN, particularly in some objects where synchrotron radiation is observed up through X-ray energies. The mechanism for this particle acceleration is believed to be diffusive shock acceleration. Diffusive shock acceleration naturally produces a power-law distribution of particle energies (see e.g., Longair 1994), with a number density $N(E) dE \propto E^{-s} dE$. It is easy to show that the synchrotron radiation from a population of particles that has a power-law energy distribution will also be a power law, with spectral index $\alpha = (s - 1)/2$. An observed spectral index of $\alpha = 0.7$ results from a particle energy spectral index of $s = 2.4$, which is very similar to the energy distribution of cosmic rays observed from Earth. Thus the synchrotron emission observed in AGN results from a population of energetic electrons that covers a wide range of energies.

At low frequencies, the optical depth for absorption due to the synchrotron process can become significant. When this optical depth is close to or larger than 1, a source is called synchrotron self-absorbed. Such a source can have a significantly flatter spectrum, and for a small frequency interval, it may even rise. In the limiting case of infinite optical depth, the spectral shape approaches $S_\nu \propto \nu^{2.5}$ at low frequencies. It is synchrotron self-absorption that accounts for the rather different spectral morphology of the compact radio-emitting components.

The electrons in the emitting region lose energy through emission. The power emitted by an electron of Lorentz factor γ , integrated over all frequencies, is

$$P = \frac{dE}{dt} = \frac{4}{9} \frac{e^4 B^2 \gamma^2}{m_e^2 c^3} = \frac{4}{3} \sigma_T c \beta^2 \gamma^2 U_B \quad (7.48)$$

where, in the last form, U_B is the energy in the magnetic field. The characteristic time in which an electron loses energy is then obtained from its energy $E = \gamma m_e c^2$ and its energy loss rate $\dot{E} = -P$ as

$$t_{\text{cool}} = \frac{E}{P} = 2.4 \times 10^5 \left(\frac{\gamma}{10^4} \right)^{-1} \left(\frac{B}{10^{-4} \text{G}} \right)^{-2} \text{ years.} \quad (7.49)$$

As the cooling time t_{cool} depends on γ^{-1} , it is thus dependent also on ν^{-1} . For low-frequency (meter-wave and longer) radio emission, this lifetime is longer than or comparable to the age of radio sources. But at higher frequencies, the cooling time becomes important, with optical synchrotron-emitting particles having radiative lifetimes typically in the hundreds of years, and X-ray synchrotron-emitting particles having radiative lifetimes of only a few years. The fact that optical and X-ray synchrotron emission are observed in a significant number of objects (see later in this chapter) means that the processes of particle acceleration are not confined to the innermost regions of an AGN but must also occur at large distances (many kiloparsecs) from the central black hole.

Since the characteristic frequency ([Fig. 7.47](#)) of synchrotron emission depends on both the radiating particle's Lorentz factor γ and the magnetic field B , it is impossible to measure both quantities independently. In order to estimate the magnetic field strength, it is often assumed that energy is divided equally between the particles and the magnetic field (this is often called *equipartition*). A second, more sophisticated approach is to first estimate the magnetic field such that the total energy of the relativistic electrons and magnetic field is minimized for a given luminosity. It can thus be shown that equipartition represents the minimum energy state for the macroscopic system and is thus a plausible, if not a physically accurate, representation of the physical state of the radiating region.

A second process, that of inverse-Compton scattering (already discussed in [Sect. 4.3](#)), also occurs in AGN jets. It is trivial to show that if the input spectrum is a power law, then the inverse-Compton process produces a power law with the same slope. The photons being scattered (the so-called *seed photons*) can come from a variety of sources – either from the jet itself (often referred to as synchrotron self-Compton), the broad or narrow-line regions, the torus, starlight, or even the cosmic microwave background. Models of AGN jet emission must take all of these regions into account as possible seed photon sources. In [Fig. 7.43](#), an example jet spectrum is shown that takes into account not only the synchrotron process but also Comptonization from broad-line photons.

Two issues must be mentioned when discussing [Fig. 7.43](#). The first is that multiple Comptonization processes are possible. One uses synchrotron photons generated within the jet (called synchrotron self-Compton or SSC). For SSC, so long as one can use the Thomson cross section (see below), one can derive that the power radiated via the inverse-Compton process is

$$P = \frac{4}{3} \sigma_T c \beta^2 \gamma^2 U_{\text{rad.}} \quad (7.50)$$

This is almost identical to the form discussed earlier ([Fig. 7.49](#)) for synchrotron energy, with the exception that in place of U_B , the energy density in the magnetic field, one has $U_{\text{rad.}}$, the

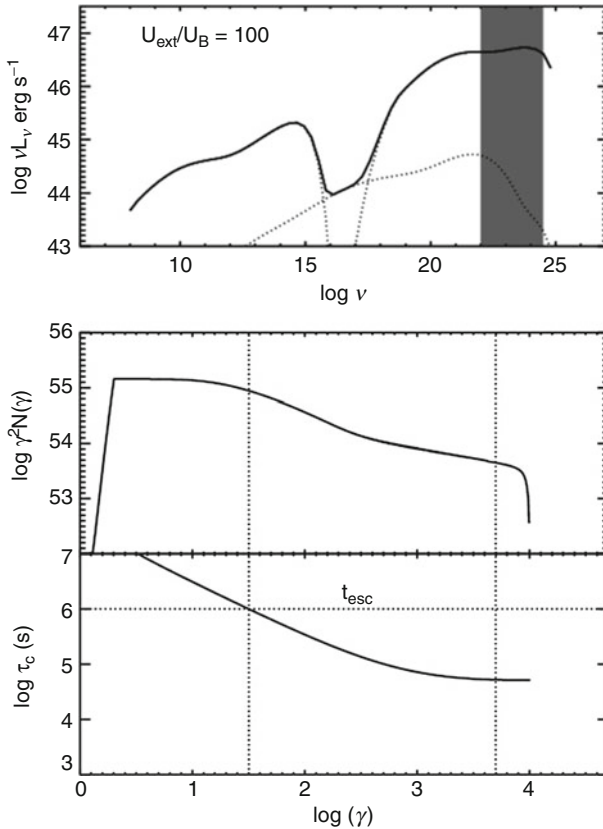


Fig. 7-43

A model for an external Compton-dominated blazar. Here the assumed ratio $U_{\text{ext}}/U_B = 100$ and we have assumed a source size $\sim 5 \times 10^{16}$ cm to ensure the dominance of EC over SSC. Bottom panel: the electron cooling time as a function of γ . Middle panel: the electron energy distribution. Top panel: the emitted power. Solid line represents total power, and dotted lines represent synchrotron (leftmost), SSC (central), and EC (rightmost and most powerful) components. The gray band is roughly the EGRET-GLAST regime (Figure taken from Perlman et al. (2008, their Fig. 6))

energy density in radiation. Thus the competition between these two processes in terms of the dominance of energy loss mechanisms breaks down to the ratio

$$\frac{P_{\text{sync}}}{P_{\text{IC}}} = \frac{U_B}{U_{\text{rad}}} \quad (7.51)$$

At most energies, the cross section for Compton scattering is simply the Thomson cross-section. However, at high energies, when $x = h\nu/m_e c^2 \geq 1$, it is necessary to use a result from quantum electrodynamics, namely, the Klein-Nishina cross section,

$$\sigma_{\text{KN}} = \frac{3}{4} \left\{ \frac{1+x}{x^3} \left[\frac{2x(x+1)}{1+2x} - \ln(2x+1) \right] + \frac{1}{2x} \ln(2x+1) - \frac{1+3x}{(2x+1)^3} \right\}. \quad (7.52)$$

The Klein-Nishina cross section is an energy-dependent modification to the Thomson cross section. At low energies ($x \ll 1$), it reduces to the Thomson cross section, but at high energies it decreases roughly as $1/x$. A rough rule of thumb is that the Klein-Nishina cross section is dominant when $\epsilon_o \gamma \sim 1$ where ϵ_o is the photon energy and γ is the Lorentz factor of the particles.

A second type of Comptonization process is also possible, where the seed photons come from outside the jet. This process, called external Compton or EC, can use seed photons either from the BLR (at small scales), the torus, starlight, or (at the largest scales) the cosmic microwave background. Which process will be dominant in a given jet depends only on the energy density of the various photon populations in the jet's comoving frame.

Thus, it is noted that [Fig. 7-43](#) was created with parameters that match 3C 279, a typical Compton-dominated source. One can see in [Fig. 7-43](#) a number of features due to the Klein-Nishina cross section. For example, there is a “hump” at optical-UV energies, where both jet and BLR seed photons are present with $\epsilon_w \gamma \sim 1$. As a result, the scatters that produce GeV photons will occur between the Thomson and Klein-Nishina regime, producing a flat or rising GeV spectrum, as well as achromatic GeV variability, with the latter occurring because electron cooling is not energy dependent in the valley between the Thomson and Klein-Nishina regime. These predictions are just beginning to be tested with data. CGRO observations of 3C 279 find a fairly flat spectrum at high energies (Joshi et al. 2011; For a counterexample, however, see Ackerman et al. 2010).

The second remark that needs to be made concerns the nature of the variability one will observe in a given source, for it is through observing variability in coordinated, multiwaveband campaigns that models of this sort can be tested. In most of the environments within AGN jets and lobes, the source is optically thin – that is, a given photon will scatter at most once before it escapes the source. Therefore the response that one would expect at gamma-ray energies would be what is known as quadratic variability – that is to say, if the source increases in flux by a factor of 2 at lower energies (i.e., in its synchrotron component), an increase of a factor 4 in its gamma-ray flux would be seen. This is the expectation if a source’s inverse-Compton emission is roughly equal or less than its synchrotron emission, as in BL Lacs. This is shown in [Fig. 7-43](#) by the lowest-luminosity set of curves.

This argument led early workers, notably Wehrle et al. (1998), to argue that due to the observation of superquadratic variability in 3C 279, an additional seed photon source, believed to be the BLR, might be needed. In 3C 279, a bright blazar with prominent broad lines, it might be natural to expect EC to contribute significantly to the observed high-energy emissions of the source; it is important to note that the data do not yet require BLR seed photons to be invoked. However, while attractive, this argument is not strictly correct.

In more luminous sources, such as 3C 279, the efficiency of Comptonization increases, as the increased number of seed photons increases the number of photon-electron collisions. After a certain point, the source will not be optically thin to Comptonization, and in fact in the most luminous sources it is Comptonization, rather than synchrotron emission, that represents the primary cooling channel for jet electrons. In these sources, the jet becomes optically thick to Compton scattering. As a result, one can get a superquadratic variability response, as pointed out by Georganopoulos et al. (2006), even without invoking an external seed photon source. [Figure 7-44](#) shows how the response of the spectrum changes as the luminosity of the synchrotron component, and corresponding dominance of the Compton channel goes up.

Observational data are now becoming good enough where direct tests of some of these models are possible. The most direct way to test these models directly is with multiwaveband campaigns, which use the fact that different physical models of emission and/or jet

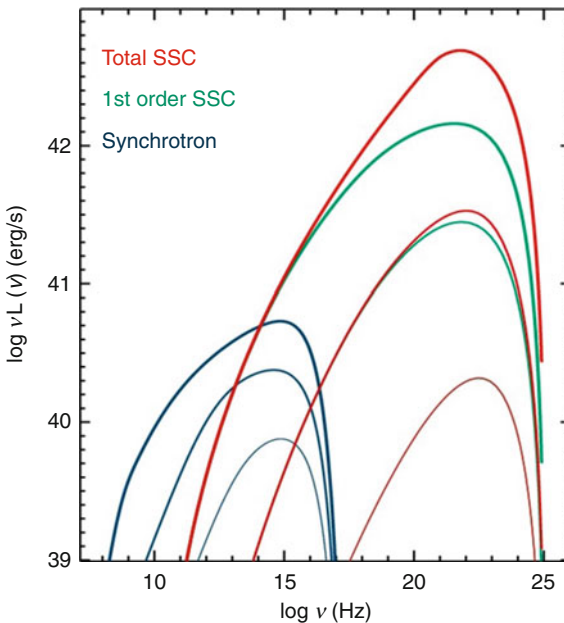


Fig. 7-44

Example spectral response for variable sources. Synchrotron emission is seen in the *left-hand* curves, whereas SSC emission is seen in the *right-hand* curves. As can be seen, as the dominance of Compton cooling increases, the source becomes optically thick to Comptonization. These second-order reactions cause superquadratic variability without the need for an external seed photon source

compression/expansion predict different responses from different jet bands. If for example, one is observing purely synchrotron emission where the main jet cooling process at X-rays is due to synchrotron emission, one would expect to observe not only correlated variability between bands but also an energy-dependent response during the cooling phase, with less energetic photons taking longer to cool, and the jet spectrum softening during the cooling process. This has been observed in the X-ray band during many BL Lac observations (e.g., Fossati et al. 2008). An alternate possibility, however, is that adiabatic expansion may dominate the cooling process, at least between bands, and this would predict no change in the SED as the source cools.

Multiwaveband campaigns can be used to test the latter set of comments regarding superquadratic variability. This was done recently by Aharonian et al. (2009) for the exceptional gamma-ray variability episodes of PKS 2155–304 during 2006. As can be seen ([Fig. 7-45](#)), at that epoch, PKS 2155 exhibited variations that were very similar in X-ray and TeV gamma-rays, but those bands were not correlated with the optical emission. Moreover, the response of the SED to the variations was not the classical quadratic one would expect – instead, nearly cubic behavior was commonly seen, as shown in [Fig. 7-38](#). This demonstrates the viability of the SSC mechanism for producing superquadratic variations. However, the lack of correlation between the X-ray/TeV and optical lightcurves led Aharonian et al. (2009) to invoke a multizone model.

As noted earlier, high-energy emissions are also seen from jets on kiloparsec scales. Here it is not so easy to find diagnostics to test the viability of emission mechanisms. While at optical

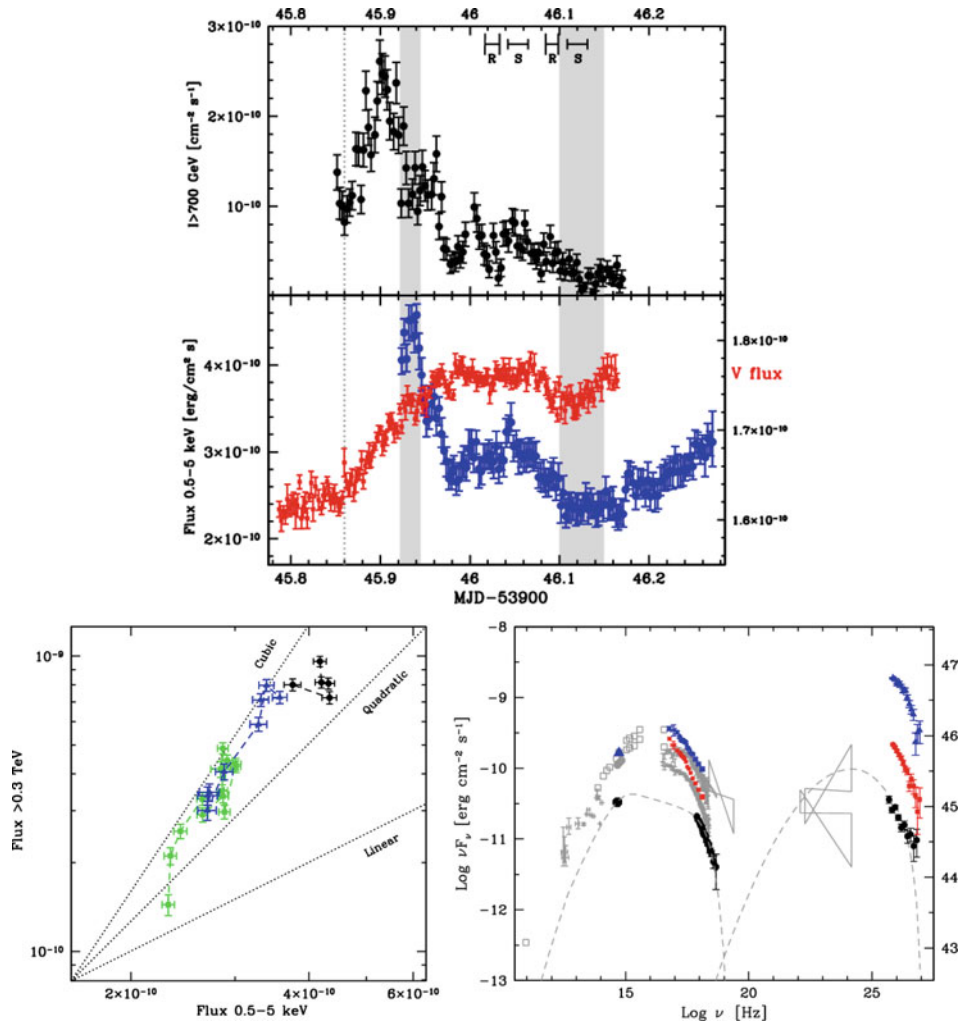


Fig. 7-45

Multiwavelength observations of PKS 2155–304 during 2006. At left, the optical (red), X-ray (blue), and TeV (black) lightcurves observed during July 29–30, 2006. Note the correlated X-ray/TeV variability, but the lack of correlation seen between those bands and the optical emission. At center, the spectral energy distributions are plotted, showing respectively the highest and lowest simultaneous states during this night, together with historical data (the latter in gray). The highest state is represented by the blue symbols, while the lowest state is represented by the red. The black points and accompanying curves represent data from the 2003 multiwaveband campaign with a 1-zone fit (Figures from Aharonian et al. (2009, respectively Figs. 2, 15, and 13))

and radio energies, synchrotron emission is the natural interpretation, supported by the spectral shape and high polarization; at X-ray energies synchrotron, and Comptonization mechanisms are both possible. For FR I sources, it is likely that synchrotron emission is the dominant X-ray emission mechanism. This is for several reasons. First of all, the observed optical-radio emission

component is seen to extrapolate to X-ray energies, albeit with breaks that may be steeper than the classical 0.5 and evidence that only a fraction of the jet cross section radiates at these high energies (see, e.g., Hardcastle et al. 2001; Marshall et al. 2002; Perlman and Wilson 2005). In addition, the variability observed in M87’s knot HST-1 weighs heavily in favor of synchrotron X-ray emission.

For more luminous, FR II sources, however, the jury is still out on the X-ray emission process (Harris and Krawczynski 2002, 2006; Hardcastle et al. 2004). The SSC mechanism is highly unlikely because it requires the jet to be massively out of equipartition; moreover, the observed morphology, whereby the jet emission is seen primarily within knots, also argues against it. However, two other mechanisms are possible, namely, synchrotron emission and Comptonization of the cosmic microwave background photons. Both processes appear to be viable at present. In some sources, for example, 3C 273 (shown in Fig. 7-40) and PKS 1136–135, the optical-UV spectrum appears to extend to high energies and connect with the Chandra emissions, and high optical polarizations are detected (Cara et al. 2010), the latter ruling out Comptonization of an unpolarized photon population (Uchiyama and Coppi 2010; McNamara et al. 2009). However, in other sources, notably PKS 0637–752 (Mehta et al. 2009), the valley in between the radio-optical and X-ray components is extreme, and a separate mechanism is needed, which is more likely to be EC/CMB.

8 Final Remarks

This chapter has discussed active galactic nuclei in considerable depth, including their properties, the current state of unified schemes, and the emission mechanisms required. As detailed in the discussion above, the evidence for the unified scheme is quite strong, so that active galaxies comprise a particular subset of the supermassive black holes that lie at the center of all bright, massive galaxies. As detailed in further chapters (Chaps. 10 and 11), these galaxies – and thus the black holes located at their centers – presumably grew hierarchically from initial density perturbations through merging of smaller galaxies into the objects seen today.

Yet despite all this discussion, the one question left unexplored is fairly basic – namely, what actually makes a given galaxy’s nucleus become active. It is fairly easy to prove that 100 million solar mass black hole, accreting at the Eddington rate, will exhaust the nuclear medium that feeds its activity in a small fraction of the Hubble time, ~a few tens of millions of years. Thus it is important to realize that the AGN phase represents a small fraction of the life cycle of a given galaxy. Moreover, in order to maintain the number of AGN seen today, it is necessary to assume that most or all bright galaxies go through an AGN phase at some time within their history but remain quiescent for the vast majority of their history.

Turning this argument around, then, a fully self-consistent understanding of the AGN phenomenon requires a working mechanism to transform a hitherto-inactive galaxy into an active one. Such a mechanism would need to be able to force large amounts of material into the galaxy’s central regions, as observations of bulges (particularly in massive galaxies) have consistently shown that the central bulges of galaxies represent an environment where many generations of star formation have exhausted the nuclear ISM, leaving it with much less material than would be required to support nuclear activity. An example of such an object would be our own galaxy, which possesses a supermassive black hole (Sag A*) that is, compared to the galaxies discussed in this chapter, remarkably inactive – estimates of its accretion luminosity are in the range of $\sim 10^{-8}$ times the Eddington rate.

The most consistent mechanism for such a transformation lies in the interaction and merging process that each galaxy undergoes throughout its history. Simulations of galactic interactions show that the merger process profoundly disturbs the matter distribution of each (e.g., Mihos and Hernquist 1996), eventually producing out of the merger a single aggregate elliptical galaxy (Barnes and Hernquist 1992) that takes several dynamical times (hundreds of millions of years) to fully relax. As the product galaxy is forming, material from the interstellar media of both galaxies falls toward the center of the aggregate. Moreover, at the same time, the central black holes of the two galaxies are also falling towards one another and will eventually merge. This latter point is actually important because it is difficult if not impossible to spin up a black hole in any way other than by merging it with another black hole that comes in with a different angular momentum and a considerable fraction of its mass.

It was for these reasons that Wilson and Colbert (1995) first proposed that a major merger of two disk galaxies could provide the mechanism for producing an active nucleus, particularly one that is radio-loud. The Wilson-Colbert hypothesis explains the strong correlation between radio-loud AGN and giant elliptical host galaxies (Chap. 11) as well as the relative numbers of radio-quiet and radio-loud AGN, the latter being a by-product of the fact that most mergers are not of nearly equal mass objects, where the central black hole could be spun up. An unequal merger could then ignite activity, but not necessarily the ejection of jets, which appears to require a strong black hole spin. Under the merging scenario, an initial merger of disk galaxies at high redshift and their individual supermassive black holes would create a rapidly spinning product black hole and a luminous AGN. However, as the surrounding cluster or group of galaxies in which the AGN is embedded develops a hot ICM, a large fraction of the cluster galaxies will be stripped of most of their gas, thus ensuring that subsequent mergers are “dry,” and provide less and less accretion power.

The merger scenario is supported by the discovery of twin, active black holes in the centers of two ultraluminous infrared galaxies (ULIRGs), NGC 6240 and Mrk 463 (Komossa et al. 2003; Bianchi et al. 2008). If the merger scenario is correct, these objects would represent an intermediate stage in the AGN development process, wherein the black holes are merging. Indeed, the host galaxies are clearly merger products, with their nuclei separated by a few kiloparsecs. A second line of evidence supporting the merger hypothesis is that HST imaging of the nearest compact symmetric objects (CSOs), which represent the very youngest of radio sources, appear to require that they underwent a major merger a few hundred million years ago (Perlman et al. 2001b) – long enough in the past that the merger of the black holes may either be in process or have taken place (e.g., Begelman et al. 1984) but also recently enough so that the nuclear medium would be expected to be dense enough to fuel an AGN. This delay of a few hundred million years is actually supported by the simulations, which show that the length of time required to force gas to the aggregate center is of the same order (di Matteo et al. 2005, 2008; Hopkins et al. 2005, 2006, 2008a, b; Springel et al. 2005a, b). It should be mentioned that in quasars, this phase might also correspond to the BAL stage, when the active nucleus is most dense. In such a case, one would expect that the luminosity of the AGN would peak when the object is very young and then decrease as the AGN ages and the amount of material available for accretion decreases. The latter mechanism has been used by Bicknell et al. (1997) to attempt to fit the luminosity function of CSOs as compared to FR II and FR I galaxies. Finally, some very recent work (Batcheldor et al. 2010) on M87 indicates that its supermassive black hole does not in fact lie in the galaxy’s dynamical center but rather is offset from the center of the isophotes by 7 pc (projected), along the direction opposite to the jet. The most consistent explanation for this

result is either that the black hole is displaced as a result of gravitational recoil resulting from the coalescence of binary supermassive black holes, or that it was accelerated by an intrinsically asymmetric jet. Since the latter hypothesis is not suggested by any other evidence, whereas the possibility of gravitational recoil is predicted by models of black hole mergers (e.g., Tichy and Marronetti 2007), which show that when two spinning black holes merge, gravitational waves can produce a kick of hundreds of km s^{-1} that damp out on Gyr timescales (Gualandris and Merritt 2008). Note, however, that due to the long damping timescale, any merger of spinning supermassive black holes can produce such an offset – not merely the one that might have been the activity's proximate cause.

As of the current writing, this merger scenario represents the leading hypothesis for the development of an active nucleus. Besides fleshing out various aspects of AGN properties and physics, it is therefore important to also test this mechanism for the development of nuclear activity.

References

- Abdo, A. A., et al. 2009a, ApJS, 183, 46
 Abdo, A. A., et al. 2009b, ApJ, 700, 597
 Abdo, A. A., et al. 2009c, ApJ, 707, 55
 Abraham, Z., Barres de Almeida, U., Dominici, T. P., & Caproni, A. 2007, MNRAS, 375, 171
 Ackerman, et al. 2010, ApJ, 721, 1383
 Aharonian, F., et al. 2006, Science, 314, 1424
 Aharonian, F., et al. 2009, A&A, 502, 749
 Alef, W., Gotz, M. M. A., Preuss, E., & Kellermann, K. I. 1988, A&A, 192, 53
 Alef, W., Wu, S. Y., Preuss, E., Kellermann, K. I., & Qiu, Y. H. 1996, A&A, 308, 376
 Allen, S. W., Dunn, R. J. H., Fabian, A. C., Taylor, G. B., & Reynolds, C. S. 2006, MNRAS, 372, 21
 Aloy, M.-A., Martí, J.-M., Gómez, J.-L., Agudo, I., Müller, E., & Ibáñez, J.-M. 2003, ApJ, 589, L109
 Antonucci, R. R. J. 1983, Nature, 303, 158
 Antonucci, R. R. J. 1984, ApJ, 278, 499
 Antonucci, R. R. J. 1993, ARAA, 31, 473
 Antonucci, R. R. J., & Miller, J. S. 1985, ApJ, 297, 621
 Antonucci, R. R. J., Hurt, T., & Kinney, A. 1994, ApJ, 430, 210
 Antonucci, R. R. J., Geller, R., Goodrich, R. W., & Miller, J. S. 1996, ApJ, 472, 502
 Arav, N., Barlow, T. A., Laor, A., & Blandford, R. D. 1997, MNRAS, 288, 1015
 Arav, N., et al. 2007, ApJ, 658, 829
 Arav, N., Barlow, T. A., Laor, A., Sargent, W. L. W., & Blandford, R. D. 1998, MNRAS, 297, 990
 Arav, N., Kaastra, J., Kriss, G., Korista, K. T., Gabel, J., & Proga, D. 2005, ApJ, 620, 665
 Artxaga, I., & Terlevich, R. 1994, MNRAS, 269, 462
 Armus, L., et al. 2006, ApJ, 640, 204
 Arshakian, T. G., Léon-Tavares, J., Lobanov, A. P., Chavushyan, V. H., Shapovalova, A. I., Burenkov, A. N., & Zensus, J. A. 2010, MNRAS, 401, 1231
 Babadzhanyants, M. K., & Hagen-Thorn, V. A. 1969, Astron. Tsirk., 526, 1
 Balbus, S. A. 2003, ARAA, 41, 555
 Barnes, T. G. 1968, ApL, 171, 1
 Barnes, J. E., & Hernquist, L. 1992, ARAA, 30, 705
 Batcheldor, D., Robinson, A., Axon, D. J., Perlman, E. S., & Merritt, D. 2010, ApJ (in press). arXiv: 1005.2173
 Beckmann, V., Barthelmy, S. D., Courvoisier, T. J.-L., Gehrels, N., Soldi, S., Tueller, J., & Wendt, G. 2007, A&A, 475, 827
 Begelman, M. C., & Sikora, M. 1987, ApJ, 322, 650
 Begelman, M. C., Blandford, R. D., & Rees, M. J. 1984, Rev. Mod. Phys., 56, 255
 Begelman, M. C., de Kool, M., & Sikora, M. 1991, ApJ, 382, 416
 Beilicke, M., Benbow, W., Cornils, R., Heinzelmann, G., Horns, D., Raue, M., Ripken, J., & Tluzczykont, M. 2005, astro-ph/0504395
 Benbow, W., Boisson, C., & Costamante, L. 2008, Proc. ICRC, 3, 1081, arXiv: 0709.4608
 Bentz, M. C., Peterson, B. M., Pogge, R. W., Vestergaard, M., & Onken, C. A. 2006, ApJ, 644, 133
 Bentz, M. C., et al. 2007, ApJ, 662, 205
 Bentz, M. C., et al. 2009a, ApJ, 705, 199
 Bentz, M. C., Peterson, B. M., Netzer, H., Pogge, R. W., & Vestergaard, M. 2009b, ApJ, 697, 160
 Bentz, M. C., Peterson, B. M., Pogge, R., & Vestergaard, M. 2009c, ApJ, 694, L166
 Bianchi, S., Chiaberge, M., Piconcelli, E., Guainazzi, M., & Matt, G. 2008, MNRAS, 386, 105

- Bicknell, G. V., Dopita, M. A., & O'Dea, C. P. 1997, *ApJ*, 485, 112
- Biretta, J. A., Zhou, F., & Owen, F. N. 1995, *ApJ*, 447, 582
- Biretta, J. A., Sparks, W. B., & Macchetto, F. D. 1999, *ApJ*, 520, 621
- Blandford, R. D., & Znajek, R. L. 1977, *MNRAS*, 179, 433
- Bolton, J. G., Stanley, J. G., & Slee, O. B. 1949, *Nature*, 164, 101
- Brenneman, L. W., & Reynolds, C. S. 2009, *ApJ*, 702, 1367
- Brotherton, M. S., Tran, H. D., van Breugel, W., Dey, A., & Antonucci, R. 1997, *ApJ*, 487, L113
- Brotherton, M. S., van Breugel, W., Smith, R. J., Boyle, B. J., Shanks, T., Croom, S. M., Miller, L., & Becker, R. H. 1998, *ApJ*, 505, L8
- Brotherton, M. S., Laurent-Muehleisen, S. A., Becker, R. H., Gregg, M. D., Telis, G., White, R. L., & Shang, Z.-H. 2005, *AJ*, 130, 2006
- Buchanan, C. L., Gallimore, J. F., O'Dea, C. P., Baum, S. A., Axon, D. J., Robinson, A., Elitzur, M., & Elvis, M. 2006, *AJ*, 132, 401
- Cannon, R. D., Penston, M. V., & Penston, M. J. 1968, *Nature*, 217, 340
- Cara, M., et al. 2010 (in prepare)
- Chelouche, D., & Netzer, H. 2001, *MNRAS*, 326, 916
- Cheung, C. C., Harris, D. E., & Stawarz, L. 2007, *ApJ*, 663, L65
- Chini, R., Kruegel, E., Kreysa, E., & Gemuend, H.-P. 1989, *A&A*, 216, L5
- Chitnis, V. R., Pendharkar, J. K., Bose, D., Agrawal, V. K., Rao, A. R., & Misra, R. 2009, *ApJ*, 698, 1207
- Cirasuolo, M., Magliocchetti, M., Celotti, A., & Danese, L. 2003, *MNRAS*, 341, 993
- Collin, S., Kawaguchi, T., Peterson, B. M., & Vestergaard, M. 2006, *A&A*, 456, 75
- Collin, S., & Kawaguchi, T. 2004, *A&A*, 426, 797
- Contopoulos, J. 1994, *ApJ*, 432, 508
- Costantini, E., et al. 2007, *A&A*, 461, 121
- Crenshaw, D. M., Kraemer, S. B., Boggess, A., Maran, S. P., Mushotzky, R. F., & Wu, C. 1999, *ApJ*, 516, 750
- Crenshaw, D. M., Kraemer, S. B., & George, I. M. 2003, *ARA&A*, 41, 117
- Crenshaw, D. M., Kraemer, S. B., Gabel, J. R., Kaastra, J. S., & Steenbrugge, K. C. 2004, *ApJ*, 607, 794
- Cristiani, S., Trentini, S., La Franca, F., Aretxaga, I., Andreani, P., Vio, R., & Gemmo, A. 1996, *A&A*, 306, 395
- de Koff, S., Baum, S. A., Sparks, W. B., Biretta, J. A., Golombek, D., Macchetto, F. D., McCarthy, P., & Miley, G. K. 1996, *ApJS*, 110, 191
- di Matteo, T., Springel, V., & Hernquist, L. 2005, *Nature*, 433, 604
- di Matteo, T., Colberg, J., Springel, V., Hernquist, L., & Sijacki, D. 2008, *ApJ*, 676, 33
- di Serego Alighieri, S., Cimatti, A., & Fosbury, R. A. E. 1994, *ApJ*, 431, 123
- Dondi, L., & Ghisellini, G. 1995, *MNRAS*, 273, 583
- Efstathiou, A., & Rowan-Robinson, M. 1995, *MNRAS*, 273, 649
- Ekers, R. D., Fanti, R., & Miley, G. K. 1983, *A&A*, 120, 297
- Elitzur, M. 2007, in *The Central Engine of Active Galactic Nuclei*, eds. L. C. Ho & J.-M. Wang (San Francisco: ASP), 415. astro-ph/0612458
- Elitzur, M., & Shlosman, I. 2006, *ApJ*, 648, L101
- Elitzur, M., Nenkova, M., & Ivezić, Z. 2004, in *The Neutral ISM in Starburst Galaxies*, eds. S. Alto, S. Huttemeister, & A. Pedlar (San Francisco: ASP), 242. astro-ph/0309040
- Fabian, A. C., Vaughan, S., Nandra, K. P., Iwasawa, K., Ballantyne, D. R., Lee, J. C., De Rosa, A., Turner, A., & Young, A. J. 2002, *MNRAS*, 335, L1
- Fanaroff, B. L., & Riley, J. M. 1974, *MNRAS*, 167, 31
- Fath, E. A. 1909, *Lick Obs. Bull.* 5, 71
- Ferguson, J. W., Korista, K. T., Baldwin, J. A., & Ferland, G. J. 1997, *ApJ*, 487, 122
- Ferland, G. J., Korista, K. T., Verner, D. A., Ferguson, J. W., Kingdon, J. B., & Verner, E. M. 1998, *PASP*, 110, 761
- Ferrarese, L., & Merritt, D. 2000, *ApJ*, 539, L9
- Filippenko, A. V. 1989, *AJ*, 97, 726
- Fossati, G., et al. 2008, *ApJ*, 677, 906
- Francis, P. J. 1996, *PASA*, 13, 212
- Gabel, J. R., et al. 2005, *ApJ*, 631, 741
- Gallagher, S. C., Brandt, W. N., Chartas, G., Priddey, R., Garmire, G. P., & Sambruna, R. M. 2006, *ApJ*, 644, 709
- Georganopoulos, M., Kazanas, D., Perlman, E. S., & Stecker, F. W. 2005, *ApJ*, 625, 656
- Georganopoulos, M., Perlman, E. S., Kazanas, D., & Wingert, B. 2006, in *Blazar Variability Workshop II: Entering the GLAST Era*, ed. H. R. Miller, K. Marshall, J. R. Webb, & M. F. Aller (San Francisco: ASP), 178
- George, I. M., Turner, T. J., Mushotzky, R. F., Nandra, K., & Netzer, H. 1998, *ApJ*, 503, 174
- Ghisellini, G., Tavecchio, F., & Chiaberge, M. 2005, *A&A*, 432, 401
- Giovannini, G., Taylor, G. B., Arbizzani, E., Bondi, M., Cotton, W. D., Feretti, L., Lara, L., & Venturi, T. 1999, *ApJ*, 522, 101
- Giovannini, G., Giroletti, M., & Taylor, G. B. 2007, *A&A*, 474, 409
- Giustini, M., Cappi, M., & Vignali, C. 2008, *A&A*, 491, 425

- Gliozzi, M., Papadakis, I. E., Eracleous, M., Sambruna, R. M., Ballantyne, D. R., Braito, V., & Reeves, J. N. 2009, *ApJ*, 703, 1021
- Gomez, J.-L., Marscher, A. P., Alberdi, A., Martí, J. M. A., & Ibanez, J. M. A. 1998, *ApJ*, 499, 221
- Goodrich, R. W., & Cohen, M. H. 1992, *ApJ*, 391, 623
- Granato, G. L., & Danese, L. 1994, *MNRAS*, 268, 235
- Green, P. J., et al. 2009, *ApJ*, 690, 644
- Green, P. J., & Mathur, S. 1996, *ApJ*, 462, 637
- Greene, J. E., & Ho, L. C. 2007, *ApJ*, 667, 131
- Greenhill, L. J., Gwinn, C. R., Antonucci, R. R. J., & Barvainis, R. 1996, *ApJ*, 472, L21
- Greenstein, J. L., & Matthews, T. 1963, *Nature*, 197, 1041
- Greenstein, J. L., & Schmidt, M. 1963, *Nature*, 197, 1041
- Greenstein, J. L., & Schmidt, M. 1963, *ApJ*, 1
- Guainazzi, M., Matt, G., Brandt, W. N., Antonelli, L. A., Barr, P., & Bassani, L. 2000, *A&A*, 356, 463
- Gualandris, A., & Merritt, D. 2008, *ApJ*, 678, 780
- Hardcastle, M. J., Birkinshaw, M., & Worrall, D. M. 2001, *MNRAS*, 326, 1499
- Hardcastle, M. J., Harris, D. E., Worrall, D. M., & Birkinshaw, M. 2004, *ApJ*, 612, 729
- Hardee, P. E. 2003, *ApJ*, 597, 798
- Hardee, P. E., & Rosen, A. 2002, *ApJ*, 576, 204
- Hardee, P. E., Hughes, P. A., Rosen, A., & Gomez, E. A. 2001, *ApJ*, 555, 744
- Hardee, P. E., Walker, R. C., & Gómez, J. L. 2005, *ApJ*, 620, 646
- Hardee, P. E., Mizuno, Y., & Nishikawa, K. 2007, *Ap&SS*, 311, 281
- Harris, D. E., & Krawczynski, H. 2002, *ApJ*, 566, 244
- Harris, D. E., & Krawczynski, H. 2006, *ARAA*, 44, 463
- Harris, D. E., Biretta, J. A., Junor, W., Perlman, E. S., Sparks, W. B., & Wilson, A. S. 2003, *ApJ*, 586, L41
- Harris, D. E., Cheung, C. C., Stawarz, L., Biretta, J. A., & Perlman, E. S. 2009, *ApJ*, 699, 305
- Hazard, C., Mackey, M. B., & Shimmins, A. J. 1963, *Nature*, 197, 1037
- Hicks, E. K. S., & Malkan, M. A. 2008, *ApJS*, 174, 31
- Hopkins, P. F., Hernquist, L., Cox, T. J., Di Matteo, T., Martini, P., Robertson, B., & Springel, V. 2005, *ApJ*, 630, 705
- Hopkins, P. F., Hernquist, L., Cox, T. J., Di Matteo, T., Robertson, B., & Springel, V. 2006, *ApJS*, 163, 1
- Hopkins, P. F., Cox, T. J., Keres, D., & Hernquist, L. 2008a, *ApJS*, 175, 356
- Hopkins, P. F., Hernquist, L., Cox, T. J., & Keres, D. 2008b, *ApJS*, 175, 390
- Hubble, E. 1926, *ApJ*, 64, 321
- Hughes, P. A., Duncan, C., & Mioduszewski, A. 1996, in *Energy Transport in Radio Galaxies and Quasars*, eds. P. E. Hardee, A. H. Bridle, & J. A. Zensus (San Francisco: ASP), 137
- Hughes, P. A., Miller, M. A., & Duncan, G. C. 2002, *ApJ*, 572, 713
- Impey, C. D., & Neugebauer, G. 1988, *AJ*, 95, 307
- Ivezic, Z., et al. 2002, *AJ*, 124, 2364
- Ivezic, Z., et al. 2004, in *AGN Physics with the Sloan Digital Sky Survey*, eds. G. T. Richards & P. B. Hall, *ASP Conference Series*, Vol. 311, 347, *astro-ph/0310569*
- Iwasawa, K., & Taniguchi, Y. 1993, *ApJ*, 413, L15
- Jackson, N., & Tadhunter, C. N. 1993, *A&A*, 272, 105
- Jaffe, W., et al. 2004, *Nature*, 429, 407
- Jansky, K. G. 1932, *Proc. IRE*, 20, 1920
- Jansky, K. G. 1933, *Proc. IRE*, 21, 1387
- Jansky, K. G. 1935, *Proc. IRE*, 23, 1158
- Jiang, L., Fan, X., Ivezic, Z., Richards, G., Schneider, D. P., Strauss, M. A., & Kelley, B. C. 2007, *ApJ*, 656, 680
- Jorstad, S. G., Marscher, A. P., Mattox, J. R., Wehrle, A. E., Bloom, S. D., & Yurchenko, A. V. 2001, *ApJS*, 134, 181
- Jorstad, S. G., et al. 2005, *AJ*, 130, 1418
- Joshi, et al. 2011, arXiv: 1111.0984
- Jourdain, E., et al. 1993, *ApJ*, 412, 586
- Kallman, T., & Bautista, M. 2001, *ApJ Suppl.*, 133, 221
- Kaspi, S., et al. 2002, *ApJ*, 574, 643
- Kaspi, S., Brandt, W. N., Maoz, D., Netzer, H., Schneider, D. P., & Shemmer, O. 2007, *ApJ*, 659, 997
- Kataoka, J., et al. 2007, *PASJ*, 59, 279
- Kellermann, K. I., Sramek, R., Schmidt, M., Shaffer, D. B., & Green, R. 1989, *AJ*, 98, 1195
- Kelly, B. C., & Bechtold, J. 2007, *ApJS*, 168, 1
- Kinman, T. D. 1968, *Science*, 162, 1081
- Kniffen, D. A., et al. 1993, *ApJ*, 411, 133
- Komossa, S., Burwitz, V., Hasinger, G., Predehl, P., Kaastra, J. S., & Ikebe, Y. 2003, *ApJ*, 582, L15
- Koratkar, A., & Blaes, O. 1999, *PASP*, 111, 1
- Körding, E. G., Jester, S., & Fender, R. 2006, *MNRAS*, 372, 1366
- Körding, E. G., Jester, S., & Fender, R. 2008, *MNRAS*, 383, 277
- Korista, K. T., & Goad, M. R. 2000, *ApJ*, 536, 284
- Korista, K. T., & Goad, M. R. 2004, *ApJ*, 606, 749
- Korista, K. T., et al. 1995, *ApJS*, 97, 285
- Kraemer, S. B., Crenshaw, D. M., & Gabel, J. R. 2001a, *ApJ*, 557, 30
- Kraemer, S. B., et al. 2001b, *ApJ*, 551, 67
- Krichbaum, T. P., Graham, D. A., Bremer, M., Alef, W., Witzel, A., Zensus, J. A., & Eckart, A. 2006, in *The Universe Under the Microscope – Astrophysics at High Angular Resolution*, *Journal of Physics: Conference Series*, Vol. 54, 328

- Krolik, J. H., 1998, Active Galactic Nuclei: From the Central Black Hole to the Galactic Environment, (Princeton: Princeton University Press)
- Larsson, J., Levan, A. J., Davies, M. B., & Fruchter, A. S. 2007, MNRAS, 376, 1285
- Leahy, J. P., & Perley, R. A. 1991, AJ, 102, 537
- Li, Z.-Y., Chiueh, T., & Begelman, M. C. 1992, ApJ, 394, 459
- Longair, M. S. 1994, High Energy Astrophysics, vol. 2: Stars and the Interstellar Medium (Cambridge: Cambridge University Press)
- Lynden-Bell, D. 1969, Nature, 223, 690
- Magorrian, J., Tremaine, S., Richstone, D., Bender, R., Bower, G., Dressler, A., Faber, S. M., Gebhardt, K., Green, R., Grillmair, C., Kormendy, J., & Lauer, T. 1998, AJ, 115, 2285
- Maiolino, R., & Risaliti, G. 2007, in The Central Engine of Active Galactic Nuclei, ed. L. C. Ho, & J.-M. Wang (San Francisco: ASP), 447
- Maraschi, L., Ghisellini, G., & Celotti, A. 1992, ApJ, 397, L5
- Maraschi, L., et al. 1994a, ApJ, 435, L91
- Marshall, H. L., Miller, B. P., Davis, D. S., Perlman, E. S., Wise, M., Canizares, C. R., & Harris, D. E. 2002, ApJ, 564, 683
- Marshall, K., Ryle, W. T., Miller, H. R., Marscher, A. P., Jorstad, S. G., Chicka, B., & McHardy, I. M. 2009, ApJ, 696, 601
- Mason, R. E., Geballe, T. R., Packham, C., Levenson, N. A., Elitzur, M., Fisher, R. S., & Perlman, E. 2006, ApJ, 640, 612
- Matt, G., et al. 1997, A&A, 327, L13
- McGill, K. L., Woo, J.-H., Treu, T., & Malkan, M. 2008, ApJ, 673, 703
- McNamara, A. L., Kuncic, Z., & Wu, K. 2009, MNRAS, 395, 1507
- Mehta, K. T., Georganopoulos, M., Perlman, E. S., Padgett, C. A., & Chartas, G. 2009, ApJ, 690, 1706
- Meier, D. L., Koide, S., & Uchida, Y. 2001, Science, 291, 84
- Meisenheimer, K., et al. 2007, A&A, 471, 453
- Melia, F. 2009, High-Energy astrophysics, (Princeton)
- Mihos, J. C., & Hernquist, L. 1996, ApJ, 464, 641
- Miller, J. S., Goodrich, R. W., & Mathews, W. G. 1991, ApJ, 378, 47
- Moore, J. H. 1915, PASP, 21, 192
- Mutel, R., Phillips, R., Su, B., & Buciferro, R. 1990, ApJ, 352, 81
- Nandra, K., George, I. M., Mushotzky, R. F., Turner, T. J., & Yaqoob, T. 1997, ApJ, 488, L91
- Nenkova, M., Sirocky, M. M., Ivezić, Z., & Elitzur, M. 2008a, ApJ, 685, 147
- Nenkova, M., Sirocky, M. M., Nikutta, R., Ivezić, Z., & Elitzur, M. 2008b, ApJ, 685, 160
- Netzer, H. 1990, in Active Galactic Nuclei, ed. T. Courvoisier, & M. Mayor (Berlin: Springer)
- O'Neill, S. M., Tregillis, I. L., Jones, T. W., & Ryu, D. 2005, ApJ, 633, 717
- Ogle, P. M., Cohen, M. H., Miller, J. S., Tran, H. D., Goodrich, R. W., & Martel, A. R. 1999, ApJ Suppl., 125, 1
- Onken, C. A., & Kollmeier, J. A. 2008, ApJ, 689, 13
- Onken, C. A., et al. 2007, ApJ, 670, 105
- Oke, J. B. 1963, Nature, 197, 1040
- Osterbrock, D. E. 1999, ApJ, 525, 337
- Osterbrock, D. E., & Ferland, G. J. 2006, in Astrophysics of Gaseous Nebulae and Active Galactic Nuclei (2nd ed.; Sausalito: University Science Books)
- Pacholczyk, A. G., & Wyemann, R. T. 1968, AJ, 73, 850
- Packham, C., Young, S., Hough, J. H., Axon, D. J., & Bailey, J. A. 1997, MNRAS, 288, 375
- Packham, C., Radomski, J. T., Roche, P. F., Aitken, D. K., Perlman, E. S., Alonso-Herrero, A., Colina, L., & Telesco, C. M. 2005, ApJ, 618, L17
- Padovani, P., Giommi, P., Landt, H., & Perlman, E. S. 2007, ApJ, 662, 182
- Pease, F. G. 1915, PASP, 27, 133
- Perlman, E. S., et al. 2011, ApJ, 743, 119
- Perlman, E. S., & Wilson, A. S. 2005, ApJ, 627, 140
- Perlman, E. S., Biretta, J. A., Zhou, F., Sparks, W. B., & Macchetto, F. D. 1999, AJ, 117, 2185
- Perlman, E. S., Biretta, J. A., Sparks, W. B., Macchetto, F. D., & Leahy, J. P. 2001a, ApJ, 551, 206
- Perlman, E. S., Stocke, J. T., Conway, J. E., & Reynolds, C. 2001b, AJ, 122, 536
- Perlman, E. S., Addison, B., Georganopoulos, M., Wingert, B., & Graff, P. 2008, in Blazar Variability Across the Electromagnetic Spectrum, <http://pos.sissa.it/p.9,arXiv:0807.2119>
- Peterson, B. M. 1993, PASP, 105, 247
- Peterson, B. M., et al. 2005, ApJ, 632, 799; Erratum: 2006, ApJ, 741, 638
- Pier, E. A., & Krolik, J. H. 1992, ApJ, 399, L23
- Poncelet, A., & Perrin, G., Sol, H. 2006, A&A, 450, 483
- Poncelet, A., Doucet, C., Perrin, G., Sol, H., & Lagage, P. O. 2007, A&A, 472, 823
- Poncelet, A., Sol, H., & Perrin, G. 2008, A&A, 481, 305
- Proga, D., Stone, J. M., & Kallman, T. R. 2000, ApJ, 543, 686
- Radomski, J. T., Piña, R. K., Packham, C., Telesco, C. M., De Buizer, J. M., Fisher, R. S., & Robinson, A. 2003, ApJ, 587, 117
- Radomski, J. T., et al. 2008, ApJ, 681, 141
- Reber, G. 1940a, Proc. IRE, 28, 68
- Reber, G. 1940b, ApJ, 100, 279
- Rees, M. J. 1966, Nature, 211, 468

- Reeves, J. N., et al. 2007, PASJ, 59, 301
- Reichard, T. A., Richards, G. T., Hall, P. B., Schneider, D. P., Vanden Berk, D. E., Fan, X.-H., York, D. G., Knapp, G. R., & Brinkmann, J. 2003a, AJ, 126, 2594
- Reichard, T. A., Richards, G. T., Schneider, D. P., Hall, P. B., Tolea, A., Krolik, J. H., Tsvetanov, Z., Vanden Berk, D. E., York, D. G., Knapp, G. R., Gunn, J. E., & Brinkmann, J. 2003b, AJ, 125, 1711
- Reynolds, C. S. 1996, PhD Thesis, Cambridge University
- Reynolds, C. S., & Fabian, A. C. 2008, ApJ, 675, 1048
- Reynolds, C. S., Fabian, A. C., Brenneman, L. W., Miniutti, G., Uttley, P., & Gallo, L. C. 2009, MNRAS, 397, 21
- Reynolds, C. S., & Miller, M. C. 2009, ApJ, 692, 869
- Reynolds, C. S., & Nowak, M. A. 2003, Phys. Rep., 389, 466
- Risaliti, G. 2002, in Inflows, Outflows & Reprocessing Around Black Holes, Proceedings of the 5th Italian AGN Meeting, <http://www.unico.it/ilaria/AGNS/proceedings.html>, p.111
- Risaliti, G., & Elvis, M. 2004, in Supermassive Black Holes in the Distant Universe, ed. A. J. Barger (Dordrecht: Kluwer), 187, astro-ph/0403618
- Risaliti, G., & Elvis, M. 2010, A&A, 516, 89
- Roche, P. F., Packham, C., Telesco, C. M., Radomski, J. T., Alonso-Herrero, A., Aitken, D. K., Colina, L., & Perlman, E. S. 2006, MNRAS, 267, 1689
- Roche, P. F., Packham, C., Aitken, D. K., & Mason, R. E. 2007, MNRAS, 375, 99
- Ross, H. N. 1970, Nature, 226, 431
- Rybicki, G. H., & Lightman, A. P. 1986, Radiative Processes in Astrophysics (New York: Wiley)
- Ryle, M. & Smith, F. G. 1948, Nature, 162, 462
- Schmidt, M. 1963, Nature, 197, 1040
- Scott, J. E., et al. 2009, ApJ, 694, 438
- Scott, J. E., Kriss, G. A., Brotherton, M., Green, R. F., Hutchings, J., Shull, J. M., & Zheng, W. 2004, ApJ, 615, 135
- Selove, D. M. 1969, ApJ, 158, 19
- Shakura, N. I., & Sunyaev, R. A. 1973, A&A, 24, 337
- Shang, Z., et al. 2005, ApJ, 619, 41
- Shemmer, O., Brandt, W. N., Gallagher, S. C., Vignali, C., Boller, T., Chartas, G., & Comastri, A. 2005, AJ, 130, 2522
- Shields, G. 1999, PASP, 111, 661
- Seyfert, C. K. 1943, ApJ, 98, 20
- Sikora, M., Madejski, G., Moderski, R., & Poutanen, J. 1997, ApJ, 484, 108
- Sikora, M., Stawarz, L., & Lasota, J.-P. 2007, ApJ, 658, 815
- Slipher, V. M. 1917, Lowell Obs. Bull., 3, 59
- Springel, V., di Matteo, T., & Hernquist, L. 2005a, MNRAS, 361, 776
- Springel, V., et al. 2005b, Nature, 435, 629
- Stocke, J. T., Morris, S. L., Weymann, R. J., & Foltz, C. B. 1992, ApJ, 396, 487
- Stone, J. M., & Balbus, S. A. 1996, ApJ, 464, 364
- Stull, M. A. 1970, Nature, 225, 832
- Suganuma, M., Kobayashi, Y., Yoshii, Y., Minezaki, T., Tomita, H., Aoki, T., Enya, K., Koshida, S., & Peterson, B. A. 2007, in The Central Engine of Active Galactic Nuclei, ed. L. C. Ho, & J.-M. Wang (San Francisco: ASP), 462
- Tang, S. M., Zhang, S. N., & Hopkins, P. F. 2007, MNRAS, 377, 1133
- Tchekhovskoy, A., Narayan, R., & McKinney, J. C. 2010, ApJ, 711, 50
- Tchekhovskoy, A., Narayan, R., & McKinney, J. C. 2011, ApJ, 711, 50
- Terlevich, R., Tenorio-Tagle, G., Franco, J., & Melnick, J. 1992, MNRAS, 255, 713
- Tichy, W., & Marronetti, P. 2007, Phys. Rev. D., 76, 061502
- Tristram, K. R. W., et al. 2007, A&A, 474, 837
- Tristram, K. R. W., et al. 2009, A&A, 502, 67
- Tsvetanov, Z. I., Hartig, G. F., Ford, H. C., Dopita, M. A., Kriss, G. A., Pei, Y. C., Dressel, L. L., & Harms, R. J. 1998, ApJ, 493, L83
- Turnshek, D. A. 1987, in QSO Absorption Lines, STScI Symposium Series 2, ed. J. C. Blades, D. A. Turnshek, & C. A. Norman (Cambridge: Cambridge University Press), 17
- Uchiyama, Y., & Coppi, P. 2010 (in prepare)
- Ulrich, M.-H., Maraschi, L., & Urry, C. M. 1997, ARAA, 35, 445
- Urry, C. M., & Padovani, P. 1995, PASP, 107, 803
- Valtaoja, E., Terasranta, H., Urpo, S., Nesterov, N. S., Lainela, M., & Valtonen, M. 1992, A&A, 254, 80
- Van den Berk, D. E., et al. 2001, AJ, 122, 549
- Veilleux, S., & Osterbrock, D. 1987, ApJS, 63, 295
- Veron-Cetty, M. P., Veron, P. 2000, A&AR, 10, 81
- Vestergaard, M., & Osmer, P. S. 2009, ApJ, 699, 800
- Vestergaard, M., & Peterson, B. M. 2006, ApJ, 641, 689
- Vestergaard, M., Fan, X., Tremonti, C. A., Osmer, P. S., & Richards, G. T. 2008, ApJ, 674, L1
- Vlahakis, N., & Königl, A. 2003, ApJ, 596, 1104
- Vlahakis, N., & Königl, A. 2004, ApJ, 605, 656
- Walker, R. C., Ly, C., Junor, W., & Hardee, P. 2009, in Approaching Micro-Arcsecond Resolution with VSOP-2: Astrophysics and Techniques, ed. Y. Hagiwara, E. Fomalont, M. Tsuboi, & Y. Murata (Astronomical Society of the Pacific: San Francisco), 227

- Wang, H.-Y., Wang, T.-G., & Wang, J.-X. 2005, ApJ, 634, 149
- Wang, J.-G., Dong, X.-B., Wang, T.-G., Ho, L. C., Yuan, W., Wang, H., Zhang, K., Zhang, S., & Zhou, H. 2009, ApJ, 707, 1334
- Wehrle, A. E., et al. 1998, ApJ, 497, 178
- Weymann, R. J., Morris, S. L., Foltz, C. B., & Hewett, P. C. 1991, ApJ, 373, 23
- Wilson, A. S., & Colbert, E. J. M. 1995, ApJ, 438, 62
- Wilson, A. S., Braatz, J. A., Heckman, T. M., Krolik, J. H., & Miley, G. K. 1993, ApJ, 419, L61
- Wu, Y., Charmandaris, V., Huang, J., Spinoglio, L., & Tommasin, S. 2009, ApJ, 701, 658
- Yip, C. W., et al. 2004, AJ, 128, 2603
- Young, S., Packham, C., Mason, R. E., Radomski, J. T., & Telesco, C. M. 2007, MNRAS, 378, 888
- Zaitseva, G. V., & Lyutyi, V. M. 1969, Astron. Zh., 526, 1
- Zhang, S.-Y., Bian, W.-H., & Huang, K.-L. 2008, A&A, 488, 113
- Zheng, W., Kriss, G. A., Telfer, R. C., Grimes, J. P., & Davidsen, A. F. 1998, ApJ, 492, 855